Charles University in Prague
Faculty of Mathematics and Physics

DIPLOMA THESIS

Hynek Němec

Application of methods in time-domain terahertz spectroscopy for investigation of ultrafast dynamics in condensed matters

Department of electronic structures
Supervisor of diploma thesis: Dr. Petr Kužel
Study programme: Physics of condensed and macromolecular matters

Acknowledgement

I would like to thank to everyone, without whom this thesis would not be written. Especially my supervisor, Petr Kužel, for providing me the possibility to work in his group, for introducing me into the topic and last but not least for the advice; and the members of the terahertz group for the pleasant and helpful atmosphere. Support through LT GaAs MBE-growth by W. Hansen and S. Schnüll is also acknowledged.

This work was supported by the National Center for Complex Molecular Systems and Biomolecules (Project No. LN00A032).

I confess I have written my diploma thesis on my own, using only quoted sources. I agree with lending of the thesis.

Prague, April 10, 2002

Hynek Němec

Contents

Název práce: Aplikace metod časově rozlišené terahertzové spektroskopie na studium ultrarychlé dynamiky v kondenzovaných látkách
Autor: Hynek Němec
Katedra (ústav): Katedra fyziky elektronových struktur
Vedoucí diplomové práce: Dr. Petr Kužel
e-mail vedoucího: kuzelp@fzu.cz

Abstrakt: Tato práce se zabývá terahertzovou (THz) spektroskopií s časovým rozlišením. Je provedena rešerše metod generace a detekce THz pulsů a jsou popsána základní experimentální schémata. Navrhli jsme experimentální uspořádání pro emisní spektroskopii, umožňující správnou interpretaci změřených dat. V tomto uspořádání jsme studovali ultrarychlou dynamiku v GaAs pěstovaném molekulární epitaxí při nízkých teplotách. Z tvaru emitovaných THz pulsu jsme určili jak doby záchytu elektronů pastmi, tak pohyblivosti elektronů v závislosti na teplotě růstu. Poslední část práce je zaměřena na metodologii experimentů optické excitace a THz sondování při slabé nerovnovážné odezvě. Aplikace dvojrozměrné Fourierovy transformace umožňuje přímý výpočet nerovnovážné zobecněné susceptibility popisující mj. solvatační dynamiku či dynamiku fotoexcitovaných nositelů v polovodičích.

Klíčová slova: THz spektroskopie, časové rozlišení, GaAs, nerovnovážná odezva, excitace–sondování.

Title: Application of methods in time-domain terahertz spectroscopy for investigation of ultrafast dynamics in condensed matters
Author: Hynek Němec
Department: Department of electronic structures
Supervisor: Dr. Petr Kužel
Supervisor's e-mail address: kuzelp@fzu.cz

Abstract: This work is focused to the terahertz (THz) time-domain spectroscopy. A bibliographic research of methods of generation and detection of THz pulses is presented and basic experimental schemes are described. We proposed an experimental setup for emission spectroscopy, which allows correct interpretation of measured data. In this setup, we studied an ultrafast dynamics of low-temperature grown GaAs. From the shape of the emitted THz pulse we determined electron trapping times as well as mobilities of electrons for several growth temperatures. The last part of this work deals with methodology of optical pump – THz probe experiments for weak nonequilibrium response. Application of two-dimensional Fourier transformation allows a direct extraction of nonequilibrium generalized susceptibility describing e.g. solvation dynamics or dynamics of photoexcited carriers in semiconductors.

Keywords: THz spectroscopy, temporal resolution, GaAs, nonequilibrium response, pump–probe.

Part 1

Introduction

This diploma work deals with a relatively novel spectroscopic method — terahertz (THz) time-domain spectroscopy. There is a lot of surprising phenomena in the THz region. The water is practically opaque here; on the other hand, most of the plastics (like polyethylene) are transparent and lenses are often fabricated from it in this region. Nothing interesting happens during propagation in the vacuum of a 1 ps pulse of visible light collimated to 1 mm, as the central period is much shorter than 1 ps (see Fig. 1.1*a*). However, the THz pulses are practically single-cycle transients with central period near 1 ps and wavelength 0.3 mm. Due to diffraction effects, the beam spreads and the shape of the pulse completely changes during propagation on few centimetres (Fig. 1.1*b*).

FIGURE 1.1: Shape of the electric intensity of a (a) visible and (b) THz pulse.

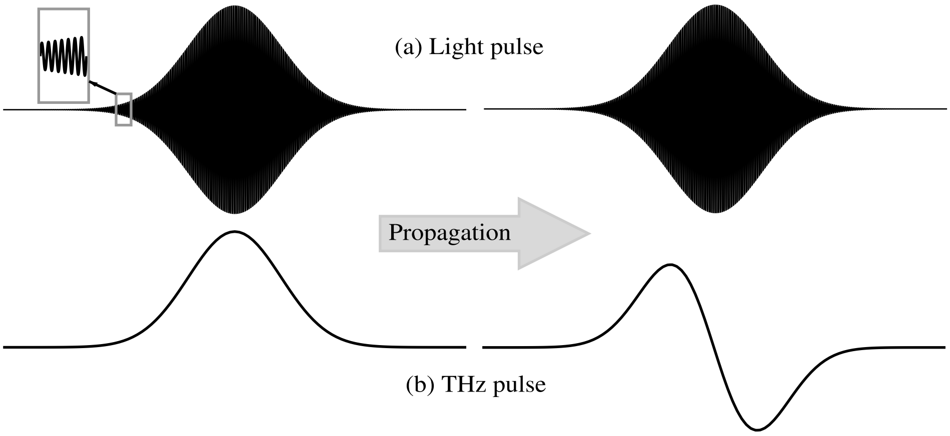

The THz region is relatively narrow (see Fig. 1.2), however, it is of great importance in condensed matter physics, as many interesting phenomena fall right to this region. These are especially soft lattice vibrations in dielectrics. The THz region bridges the millimetre wave region and infrared region (see Fig. 1.2). The millimetre wave region is accessible via conventional radiofrequency methods, which cannot be extended as the frequency of synthesizers is limited. In the infrared region, the optical devices are used. However, while the frequency is lowered, the brightness of common infrared radiation sources practically vanishes.

FIGURE 1.2: Overview of frequency regions.

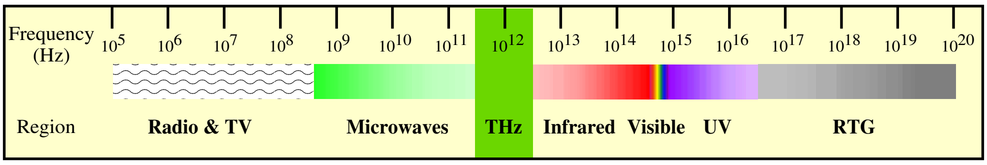

How can be expressed 1 THz:

$$\mathbf{1\,THz = 1\,ps = 0.3\,mm = 33\,cm^{-1} = 4.1\,meV = 48\,K}.$$

The rise of THz time-domain spectroscopy is dated by the development and spread of femtosecond laser sources, i.e. this method is barely 20 years old now. A block scheme of a THz time-domain spectrometer is given in Fig. 1.3. The whole spectrometer is driven by a femtosecond laser. An ultrashort pulse from it is divided into two parts by a beam splitter (BS_1 in

FIGURE 1.3: Block scheme of a THz time-domain spectrometer. The whole apparatus (i.e. the emitter, detector and pump beam eventually) is synchronized by the femtosecond laser pulse.

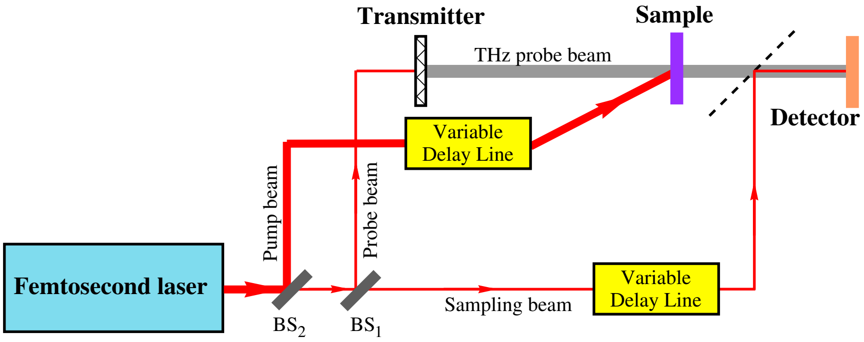

Fig. 1.3). The first part (probe pulse) irradiates the transmitter, generating a THz electric transient. The second part (called gating or sampling pulse) gates the detector, i.e. the detector tells us, what was the instantaneous THz field in the moment of the gating pulse arrival. By delaying the gating pulse, we can measure the shape of the whole THz pulse. That's why we are talking about the *time-domain* spectroscopy.

As the THz spectroscopy is a time-domain method, the pump – probe experiments can be performed very easily. The sample can be excited by the optical *pump* beam (thick lines in Fig. 1.3), which is split from the femtosecond laser beam — the pump beam is perfectly synchronized with the THz probe pulse and gating pulse. During last few years, the femtosecond optical amplifiers and parametric generators became commercially available. The first enabled us to generate a very intense excitation pulse and the latter to tune the excitation wavelength.

This makes the THz time-domain spectroscopy very suitable for investigations of ultrafast dynamics on the subpicosecond time scale. This very new technique has been already employed for studies of dynamics in semiconductors and superconductors. Currently, very challenging problems are studies concerning the solvation dynamics in liquids. However, up to now, the interpretation of the measured data still remains an opened problem.

This work is structured in the following way. A bibliographical research concerning THz time-domain spectroscopy is provided in part 2: sections 2.1 and 2.2 deal with the sources and detectors of the THz radiation, section 2.3 describes the most important techniques based on the THz time-domain spectroscopy and section 2.4 presents a brief overview of problems solved in condensed matter physics via THz spectroscopy. The major part of this diploma work is devoted to the development of the THz emission spectroscopic technique and its application on ultrafast semiconductors and to the methodology of optical pump – THz probe experiments. Thus, in part 3 an investigation of an ultrafast dynamics in a semiconductor GaAs by the THz time-domain emission spectroscopy is reported. It describes a new setup, in which it is possible to establish a straightforward relation between the measured THz waveform and the dynamics of photoexcited free carriers in the sample. Part 4 deals with the development of methods relating the generalized nonequilibrium susceptibility and the measured THz waveforms in optical pump – THz probe experiments. Finally, the boon of this work is summarized in part 5.

Part 2

Principles and applications of THz spectroscopy

2.1 Sources of THz radiation

Most of the sources of coherent THz transients are based on mechanisms, which are triggered by ultrashort laser pulses. The first sources of coherent THz transients were based on photoconductive switches irradiated by 100 fs laser pulses [1]. The photogenerated carriers are accelerated in an electric field (external bias or a surface depletion field), thus radiating into material or free space. With the development of high-power ultrafast lasers it became possible to generate THz radiation via optical rectification [2]. The spectrum of THz pulses generated by optical rectification can be now extended to cover a spectral range from 100 GHz to 70 THz [3].

The emission process itself can be an object of the scientific investigation. For example, charge oscillations involved in quantum beats [4] or Bloch oscillations [5] produce THz radiation and can be studied through the THz waveform analysis.

Besides these optically gated devices, there are other sources of THz radiation based on oscillations of an electron beam. Most of them generate narrow band coherent tunable radiation. Namely backward wave oscillators and free electron lasers are involved in condensed matter research.

2.1.1 Biased and unbiased photoconductive emitters

All photoconductive emitters are based on the same principle. An incoming laser pulse with a photon energy above the band gap excites free carriers to the conduction band. These *free* carriers are immediately being accelerated due to the presence of an electric field inside the emitter (see Fig. 2.1*a*), i.e. the current density rapidly increases (Fig. 2.2*a*) and radiates into the material or free space (Fig. 2.2*b*). Finally, the photoexcited free carriers are trapped or recombine and the current density returns to its steady value — the emitter is prepared for the emission of the next pulse.

FIGURE 2.1: (a) Principle of generation of THz pulses in photoconductive emitters. (b) Dimensions of large and (c) small aperture emitter.

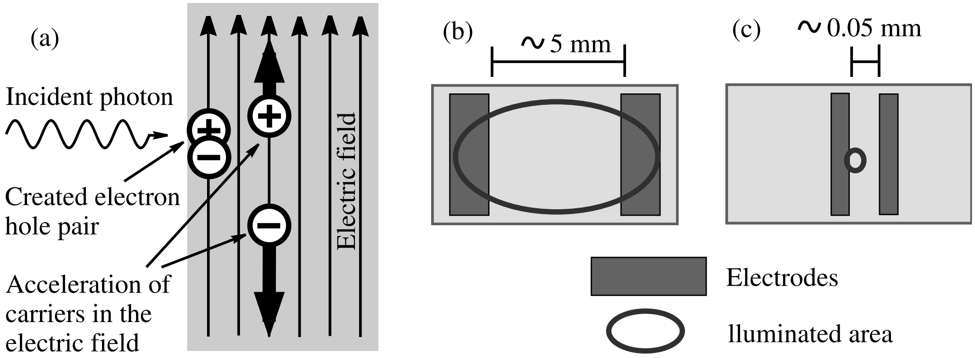

The very first emitters were **biased small aperture** ones [1] (Fig. 2.1*c*), i.e. the wavelength of THz radiation is larger than the aperture of the emitter. Such sources can by well approximated by an elementary Hertzian dipole $p(t)$. The electric field at a distance r, and angle θ relative to the dipole axis is then [1]

$$E(t) = \frac{1}{4\pi\varepsilon_0 N^2}\left(\frac{p(t)}{r^3} + \frac{N}{cr^2}\frac{\partial p(t)}{\partial t} + \frac{N^2}{c^2 r}\frac{\partial^2 p(t)}{\partial t^2}\right)\sin\theta, \tag{2.1}$$

where c is the velocity of light, ε_0 is permittivity of vacuum and N is the refractive index of the medium in which is placed the dipole. The first term can be identified with the quasistatic field, the second with the near field and the last one with the far field. The on-axis radiated field far from the dipole is thus simply described by

$$E(t) = \frac{\mu_0}{4\pi r}\frac{\partial^2 p(t)}{\partial t^2} \tag{2.2}$$

$$\text{or by}\quad E(t) = -\frac{e\mu_0}{4\pi r}\frac{\partial I(t)}{\partial t} \tag{2.3}$$

using the current I forming the dipole. A typical example is shown in Fig. 2.2. The radiated field deduced via Eq. (2.3) from the current waveform (Fig. 2.2*a*) is depicted in Fig. 2.2*b* and appropriate spectra of both are drawn in Fig. 2.2*c* and *d* respectively.

Figure 2.2: (a) Evolution of the current flowing through the emitter. (b) Shape of the electric transient far from the emitter. (c) Spectrum of the current and (d) spectrum of the radiated field.

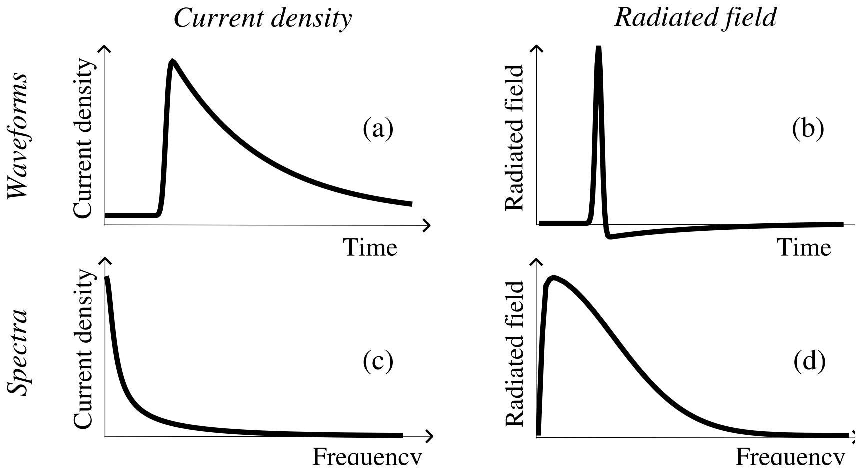

The directional characteristics of the radiation into the free space are more complicated then the dipole radiation due to the presence of the substrate. Common property of these kinds of sources is a high divergence. Thus a collimating lens attached directly to the emitter is used to enhance the radiated power in the forward direction [6]. The radiation patterns are calculated and measured in [7] and [8].

Later on, with the development of high-power ultrafast lasers, it became possible to use **large aperture** emitters (Fig. 2.1*b*), which allow generation of intense THz pulses at lower divergence. The radiated field can be calculated as a superposition of elementary dipoles [9]. Such calculations show, that these sources radiate more directionally, and thus higher intensity can be easily achieved. Expressions (2.2) and (2.3) (far from the emitter) remain valid, but the proportionality constant is different.

Initially, the radiated electric field scales linearly with the optical fluence. However it saturates at high fluence [10, 11], thus sufficiently large emitters are required to make use of the whole fluence. The scaling with the bias electric field is practically linear [11, 12], but a breakdown can occur at high voltages.

The electric field for accelerating carriers is very often produced by an external electric source — this is referred to as **biased** photoconductive emitters in the literature. Such emitters are based on radiation damaged silicon on sapphire (RD-SOS) [1], InP [12], Cr-doped GaAs [8], GaAs grown at low temperatures [13] and others.

It was demonstrated, that also the surface depletion field can act as the bias for the carrier acceleration [14]. Such an electric field is perpendicular to the emitter surface and the emitted THz field vanishes for normal incidence of the excitation optical beam. Consequently, arrangements with oblique incidence (e.g. near the Brewster angle) are required. This type of THz generation was investigated in a large number of materials, e.g. arsenic-ion-implanted GaAs [15], Fe-doped InP, semi-insulating GaAs and CdTe including the effects of doping [16].

2.1.2 Optical rectification

Optical rectification in potassium dihydrogen phosphate (KDP) and potassium dideuterium phosphate ($\mathrm{KD_dP}$) was first demonstrated to produce radiation in MHz region using $0.1\,\mu$s laser pulses [17]. Later, this method was extended to picosecond regime due to optical rectification on $\mathrm{Cu^{++}}$ ions in $\mathrm{LiTaO_3}$ [18]. Further development allowed generation of freely propagating radiation [2] and thus easy implementation to various THz experiments. Nowadays, optical rectification is a method allowing to generate ultrashort pulses with a spectrum extending up to 70 THz [3].

Optical rectification takes place in noncentrosymetric materials. We can look upon this effect as an inverse process to the Pockels effect: in fact, the optical field generates the THz field, i.e. nearly DC voltage comparing to the carrier frequency of the optical field. In order to describe this phenomenon, it is convenient to treat it as a special case of a difference frequency generation, where optical photons with close frequencies ν_1 and ν_2 produce far-infrared photon with frequency $f = |\nu_1 - \nu_2|$. The generated nonlinear polarization may be described by formula

$$P_i^{\mathrm{THz}} = \sum_{j,k} \chi_{ijk}^{(2)} E_j E_k \tag{2.4}$$

where $\boldsymbol{E}$ represents the incident optical field and $\chi^{(2)}$ is the second-order nonlinear susceptibility tensor. Obviously, the polarization, and thus the radiated field (Eq. (2.2)) is proportional to the intensity of the optical beam. The spectrum of the optical pulse broadens when shorter pulses are used. Thus more distant frequencies can mix and also the THz pulse spectrum may broaden.

It is convenient to distinguish mechanisms by which the THz waveform generation occurs in different materials. When the optical frequency is high enough to cause a band-to-band transition, free carriers are generated and moved, the nonlinear susceptibility has a high value because it is resonant.

Otherwise, when the transition is virtual, only bonded carriers are anharmonically displaced. In this case, the nonlinear susceptibility is nonresonant, and consequently smaller. The fact how closely a phase-matching condition is satisfied becomes very important. This property is usually characterized by the pulse walk-off defined as

$$\frac{|N_{\mathrm{g}}(\nu) - n_{\mathrm{THz}}(f)|}{c}, \tag{2.5}$$

where N_{g} is the group refractive index of the optical pulse and n_{THz} is the refractive index of the THz component with the frequency f. The phase-matching condition reads $N_{\mathrm{g}}(\nu) - n_{\mathrm{THz}}(f) = 0$. In several materials, the phase-matching condition is not satisfied, though intense THz radiation may be generated.

Let us enumerate the main cases:

- The optical transition is **nonresonant**, and the **phase-matching** condition is **satisfied**. The representative materials is ZnTe [19] (pulse walk-off $\sim$ 140 fs/mm as measured in our laboratory) which is now very widely used. The accessible frequency region with ZnTe usually spreads from millimetre waves (0.1 GHz) up to 3 THz [19]. Other materials, like poled copolymer [20] and GaSe [21] are under investigation.

- **Resonant** optical transition occurs. Then the optical beam is absorbed typically within few microns, and the phase-matching condition becomes meaningless. The appropriate nonlinear coefficient is usually very high, leading to the generation of an intense THz radiation. This type of optical rectification can be observed for example in GaAs [22, 23], InP and CdTe [24] when the photon energy of the excitation beam exceeds the band gap.

- Even for **nonresonant** transitions with **phase-matching** condition **not satisfied**, a significant THz radiation can be produced via polarization shock-wave. This is commonly referred in the literature as the Čerenkov-like radiation. It was predicted by Askayran et al. already in 1962 [25]. In most materials, the refractive index for the THz beam is higher than the group refractive index for the optical beam due to polar-phonon contribution to the dielectric constant. Then the waves with low frequencies propagate slower than the incident optical pulse. This leads to the formation of the polarization shock-wave on a Čerenkov-like cone generated via optical rectification effect. A setup producing far-infrared radiation up to 4 THz in $LiTaO_3$ was reported [26] and a free-space propagation of such THz waves was also demonstrated [27].

- There are some crystals composed of organic molecules with very high electronic polarizabilities, and consequently with high nonlinear coefficients. As these nonlinearities have purely electronic origin without vibronic contribution, the relevant nonlinear coefficient responsible for the optical rectification is huge compared to anorganic crystals. The optical rectification signal can thus be detected even if the phase-matching condition is not satisfied. This is the case of monoclinic organic crystal DAST (dimethyl amino 4-*N*-methylstilbazolium tosylate) [28] and derivatives of MNA (2-methyl-4-nitroaniline) [29].

- Optical rectification on the surfaces was observed in ⟨100⟩ and ⟨111⟩ oriented InP [30] — the presence of the surface depletion field can induce the linear electrooptic effect even in centrosymmetric crystals. Of course, this effect is related to the quadratic electrooptic effect, i.e. one can describe it in terms of four-waves mixing:

$$0_{\text{surface}} + \nu_1 + (-\nu_2) \rightarrow f. \tag{2.6}$$

2.1.3 Sources of continuous radiation

There is also a variety of devices based on electron beams. Unlike preceding sources, these do not generate few-cycle transients, but rather chunks of nearly monochromatic waves (free electron laser, gyrotron) or continuous monochromatic wave (klystron, magnetron and backward wave oscillator). Their wavelength can be usually less or more tuned. Most of them generate very intense radiation, but the cost is low operating frequency. Only backward-wave oscillators and free electron lasers and gyrotron can access THz region. frequencies above 100 GHz. Their typical parameters are summarized in Tab. 2.1.

Experimental arrangements having a **backward-wave oscillator** are frequently used in the condensed matter research. The source generates high-power (10 mW at 0.5 THz) and tunable highly monochromatic $\Delta f/f \sim 10^{-5}$ radiation covering the range from 35 GHz to 1 THz [31]. These methods also allow measurements of the complex transmission and reflection (and thus complex optical constants). However, the amplitude and phase are measured separately in slightly different setups, i.e. the measurements are separated in time. Though this method is very suitable when spectroscopic measurements with high frequency resolution are required.

Free electron laser generates tunable, coherent and high-power radiation over a large part of the electro-magnetic spectrum, ranging from millimetre waves, up to potentially X-rays. However, it is a large scale device requiring a high energy electron beam. More detailed info can be found [32], where are links to most of free electron laser sites.

TABLE 2.1: Parameters of devices based on electron beams: free-electron lasers operating in THz frequency region (FIR-FEL and MM-FEL on University of California, Santa Barbara, [33]) and backward-wave oscillators (BWO, [31]).

Quantity	FIR-FEL	MM-FEL	BWO
Range (μm)	338 – 63	2500 – 338	8500 – 300
Range (THz)	0.89 – 4.76	0.12 – 0.89	0.035 – 1.0
Peak power	6 – 1 kW	15 – 1 kW	$> 10\,$mW
Pulse length	1 – 20 μs	1 – 20 μs	continuous
Repetition rate	0 – 7.5 Hz		continuous

2.2 Detectors of THz radiation

Once the THz pulse is generated, it is possible to reconstruct through photoconductive or electrooptic gating the shape of its electric (or magnetic) field $E_{\mathrm{true}}(t)$ at a given position in space. It means, that in contrast to common optical methods, where only the light intensity $\propto |E_{\mathrm{true}}(f)|^2$ at particular frequency f is measured, one can access here both amplitude and phase of any frequency component constituting the temporal waveform.

The first phase-sensitive detector for the THz range was based on a photoconductive antenna [1] built on the same block of material as the emitter. The THz transients were detected also via conventional electrooptic sampling [34]. Nowadays, the freely propagating THz radiation is detected usually by photoconductive antennas [35] and free-space electrooptic sampling [36]. The latter technique is able to work up to mid-infrared region [3]. Recently, a magnetooptic sampling was employed to measure directly the shape of magnetic field of THz pulse [37]. Techniques that do not provide information about the phase are used only rarely. These are usually bolometric and autocorrelation methods [38].

Due to several effects (like dispersion in the sensor), the measured waveform E_{meas} in THz spectroscopy practically always differs from the true one. These effects can be described by the response function $\mathcal{D}$ of the detector. The measured waveform can be written as

$$E_{\mathrm{meas}}(t) = E_{\mathrm{true}}(t) * \mathcal{D}(t). \tag{2.7}$$

Fortunately, it is not necessary to know the response function for processing measured data, when equilibrium spectroscopy (sections 2.3.1 and 2.3.2) is being performed. However, knowledge of the detector response $\mathcal{D}$ becomes an important point for emission and pump – probe experiments (sections 2.3.3 and 2.3.4).

2.2.1 Photoconductive receiving antennas

Photoconductive detectors are based on the inverse mechanism to the photoconductive transmitter (section 2.1.1). The optical gating pulse generates free carriers in the photoconductive medium, the THz electric field acts as the bias voltage and the generated current is measured. For simplicity, let us assume very short carrier lifetimes. In this situation, the current flows through the detector only in the simultaneous presence of the laser pulse and THz electric field. Assuming the validity of Ohm's law, the total amount of the transported charge is proportional to the instantaneous THz electric field when the gating pulse arrived (see Fig. 2.3). Scanning of the time delay between the THz pulse and the optical gating pulse allows to determine the whole THz waveform $E_{\text{meas}}(t)$.

FIGURE 2.3: Operation of the photoconductive antenna. The total charge transferred during one pulse is proportional to the amplitude of THz beam at the moment of the sampling pulse arrival.

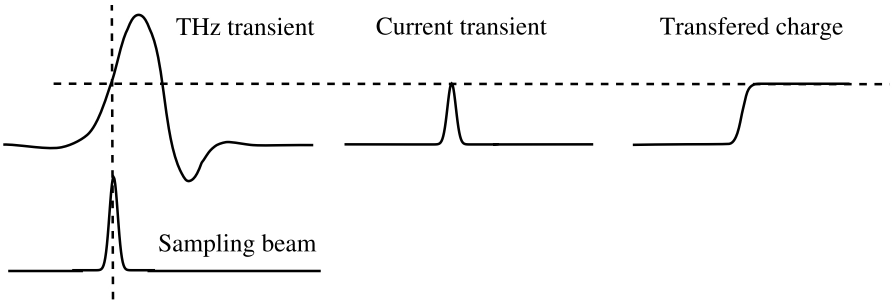

As we have mentioned in the introduction, this technique was first used by Auston [1] using radiation-damaged silicon on sapphire. The common materials are low-temperature grown GaAs [39], semi-insulating GaAs [40, 41] and semi-insulating InP [40]. However, the detectors based on long-lifetime photoconductors (like semi-insulating GaAs) measure directly only the primitive function of the THz field, thus a diferenciation needs to be performed. This results in f^{-1} sensitivity for higher frequencies. On the other hand, this suggests that carrier lifetime limits the speed of photoconductive detectors only partially. Photoconductive antenna based on low-temperature grown GaAs with carrier lifetime 1.4 ps was reported to be sensitive up to 20 THz using 15 fs gating pulses [39].

2.2.2 Electrooptic sampling

Electrooptic sampling is based on the linear electrooptic effect. In an electrooptic crystal, the THz transient E_{THz} induces an instantaneous birefringence

$$\Delta n \propto E_{\mathrm{THz}}. \tag{2.8}$$

which influences the propagation of an optical sampling beam. In a crystal with thickness L, the phase shift between the ordinary and extraordinary part of the sampling beam is

$$\Delta\varphi = \frac{2\pi\nu}{c}\Delta n L, \tag{2.9}$$

where ν is the frequency of the sampling beam. This can cause, for example, a conversion of a linearly polarized sampling pulse into a slightly elliptically polarized pulse (Fig. 2.4). This ellipticity is then detected. As the sampling pulse is usually very short, the measured ellipticity gives access to the instantaneous electric field E_{THz} at the moment of the sampling pulse arrival. Similarly as in the case of photoconductive detection, time-delay scans of the sampling pulse allow to determine the THz waveform $E_{\mathrm{meas}}(t)$.

FIGURE 2.4: Principle of the electrooptic sampling technique: setup with single photodetector.

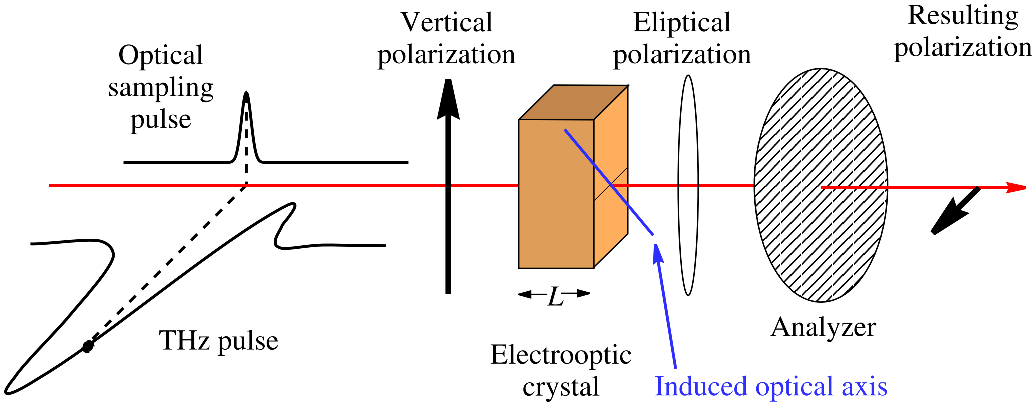

In the setup depicted in Fig. 2.4, the change in the detected sampling pulse intensity is related to the electric field E_{THz}, or rather to the induced phase delay φ via formula

$$I_{\mathrm{s}} \propto \frac{I_{\mathrm{s},0}}{2}(1 - \cos \Delta\varphi). \tag{2.10}$$

There are two problematic points in this setup. First, this formula holds only in the ideal case. If the polarization of the sampling beam is not exactly linear and exactly vertical, an additional phase shift will appear in Eq. (2.10). The imperfections of the crystal further complicate the extraction of the THz field [42]. Second, changes of the sampling beam intensity are very low. Such setup may be thus sensitive to other light sources and parasite reflections of the laser beam. Though this setup may be preferred when single photodetector is to be used, like in THz imaging applications. This technique was also used for single shot measurements in conjunction with chirped sampling beam [43].

FIGURE 2.5: Electrooptic sampling: detection of ellipticity by a pair of balanced photodiodes gives a signal proportional to the THz field E_{THz}.

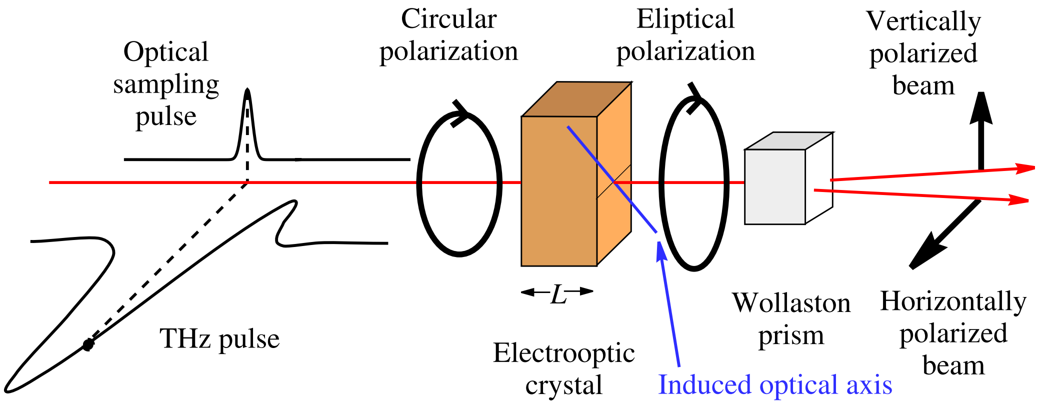

An essentially higher signal and a linear response is achieved in the setup shown in Fig. 2.5, where a circularly polarized sampling beam is used. The deviations from circular polarization are detected by a pair of balanced photodiodes. It can be simply derived, that the difference ΔI_{s} between the intensity of horizontally (I_{H}) and vertically (I_{V}) polarized part of the sampling beam is given by

$$\Delta I_{\mathrm{s}} = I_{\mathrm{H}} - I_{\mathrm{V}} \propto I_{\mathrm{s},0} \sin \Delta\varphi \tag{2.11}$$

and is thus proportional to the THz electric field E_{THz} for reasonable THz signals (e.g. for 1 mm thick ZnTe sensor a 1 % deviation from linearity occurs at 10 kV/cm).

The most popular materials for free space electrooptic sampling are ZnTe [44–46] which is commonly used in the range from 0.1 THz to 3 THz, GaP [47] and DAST [48]. Materials like $LiTaO_3$ [49] and $LiNbO_3$ [50] were used for both conventional and free space electrooptic sampling. Reflective electrooptic sampling in low-temperature grown GaAs was used to study the changes of surface electric field [51].

2.2.3 Magnetooptic sampling

Magnetooptic sampling is a technique based on Faraday rotation effect, caused by transient magnetic field. Its reported sensitivity is 10^{-7} T [37]. The experimental setup requires orthogonal geometry (Fig. 2.6), as the magnetic field needs to be parallel with the sampling beam propagation direction. The induced elipticity is proportional to the magnetic field. Sensors built from terbium-gallium-garnet and amorphous glass SF-59 were investigated [37].

FIGURE 2.6: Scheme of the free-space magnetooptic sampling technique.

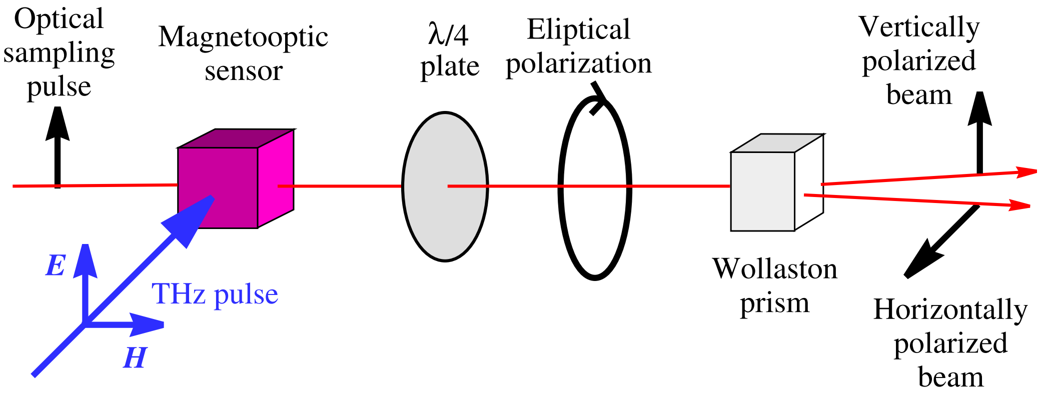

2.2.4 Other methods

The **bolometric methods** are of limited usage due to few information provided at high expense. Bolometers are usually used in the interferometric setups. The interferograms of THz pulses give the amplitude spectrum of the THz transient only, but still not the information about the phase. This does not allow the reconstruction of the pulse shape in the time domain. The first interferometric characterization of THz transients was reported by Greene et al. [38].

2.3 Various setups in THz spectroscopy

THz time-domain spectroscopy was successfully applied to the investigation of both equilibrium and nonequilibrium systems. For **equilibrium** systems, the main aim is to obtain the complex refractive index N or complex relative permittivity ε or complex conductivity σ of the studied material in the far-infrared and submillimetre frequency range. These quantities are connected via relations

$$\varepsilon(f) = \sqrt{N(f)} \quad \text{and} \quad \sigma(f) = 2\pi \mathrm{i} f \varepsilon_0 (1 - \varepsilon(f)). \tag{2.12}$$

These properties are usually extracted from the measurements of the THz transmission. Measurements of reflectivity are of limited usage as they are very sensitive to the positioning of the sample and to the stability of the apparatus.

For **nonequilibrium** systems, an effort is made to obtain the temporal evolution of the current density or of the polarization directly from the shape of the THz waveform. This approach is usually related to the emission spectroscopy [8,52] or to the optical pump – THz probe experiments [53,54].

2.3.1 Transmission spectroscopy

The transmission spectroscopy (Fig. 2.7*a*) is probably the most widespread method in the THz region. It was used for studying a great variety of materials, including dielectrics [55], semiconductors [56], superconductors [57], organic materials [58], liquids [59], gases [60] and flames [61]. As this method is a prototype of most of the methods in THz time-domain spectroscopy, following paragraphs discuss this method in detail.

Optical spectroscopy is usually carried out by measuring the relative *intensity* of monochromatic *light* passing through the sample. This allows a determination of the appropriate optical constant at this wavelength. Similarly, in THz time-domain spectroscopy, the optical constants are extracted from the transmission defined as

$$T(f) = \frac{E^{\mathrm{sam}}_{\mathrm{meas}}(f)}{E^{\mathrm{ref}}_{\mathrm{meas}}(f)}, \tag{2.13}$$

where $E^{\mathrm{sam}}_{\mathrm{meas}}(f)$ and $E^{\mathrm{ref}}_{\mathrm{meas}}(f)$ are the detected fields with and without the presence of the sample, respectively. Unlike in optical spectroscopy, we are able to measure the shape of the waveforms $E_{\mathrm{meas}}(t)$. This implies, that both the amplitude and the phase of Fourier components $E_{\mathrm{meas}}(f)$ are determined and thus the *complex* refractive index of the sample can be extracted.

FIGURE 2.7: Basic setups for each type of THz spectroscopy: (a) transmission, (b) reflection, (c) emission and (d) optical pump – THz probe. Instead of the pair of elliptical mirrors (represented by arcs in the picture), four parabolic mirrors are often used.

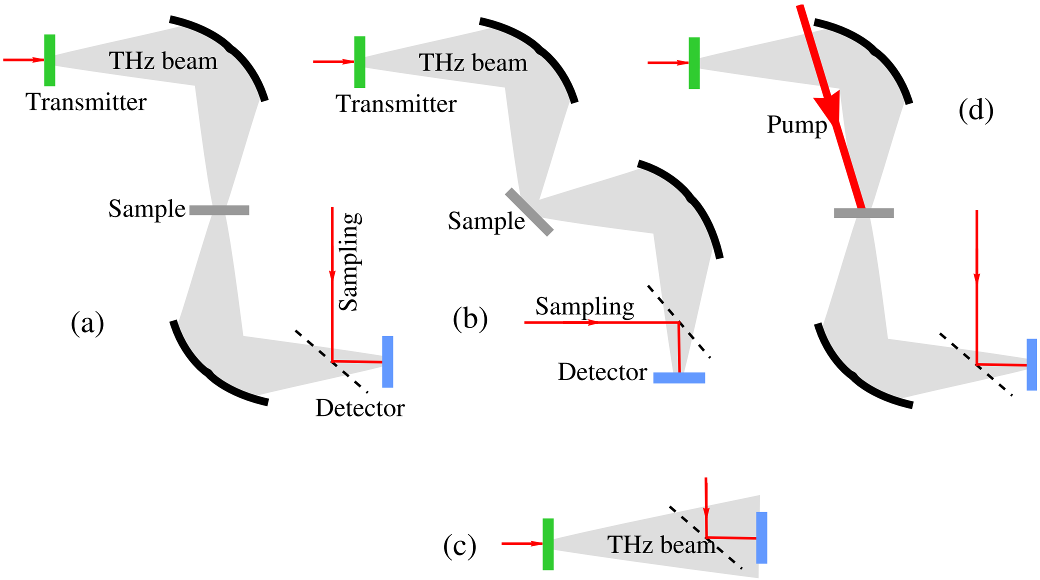

The measured waveform can be described (in the frequency domain) by the formula

$$E_{\text{meas}}(f) = E_{\text{emit}}(f) \cdot \mathcal{P}_{\text{bef}}(f) \cdot \mathcal{T}(f) \cdot \mathcal{P}_{\text{aft}}(f) \cdot \mathcal{D}(f). \tag{2.14}$$

Here, E_{emit} is the waveform emitted by the emitter, functions $\mathcal{P}_{\text{bef}}$ and $\mathcal{P}_{\text{aft}}$ describe the reshaping due to the propagation before and after the sample respectively, $\mathcal{T}$ stands for the propagation through the sample and $\mathcal{D}$ is the detector response. Except of $\mathcal{T}$, functions on the right-hand side of Eq. (2.14) cannot be usually simply constructed or measured. That's why two measurements are performed. After substitution of Eq. (2.14) to Eq. (2.13) these unknown apparatus quantities cancel out:

$$T(f) = \frac{E^{\text{sam}}_{\text{meas}}(f)}{E^{\text{ref}}_{\text{meas}}(f)} = \frac{E_{\text{emit}}(f)\mathcal{P}_{\text{bef}}(f)\mathcal{T}^{\text{sam}}(f)\mathcal{P}_{\text{aft}}(f)\mathcal{D}(f)}{E_{\text{emit}}(f)\mathcal{P}_{\text{bef}}(f)\mathcal{T}^{\text{ref}}(f)\mathcal{P}_{\text{aft}}(f)\mathcal{D}(f)} = \frac{\mathcal{T}^{\text{sam}}(f)}{\mathcal{T}^{\text{ref}}(f)}. \tag{2.15}$$

Though all of them still indirectly affect this quantity. In the range, where they become small, they significantly increase the relative error of the measured waveform E_{meas} and thus do not allow a precise measurement of the transmission function T.

The propagation $\mathcal{T}^{\mathrm{sam}}$ through the sample can be simply constructed assuming (a) the sample is placed in the air, (b) THz beam is collimated, (c) the sample is a plane-parallel plate and (d) the THz beam irradiates the sample at normal incidence. Then

$$\mathcal{T}^{\mathrm{sam}}(f) = \frac{4N}{(N+1)^2} \exp\left(2\pi \mathrm{i} f \tfrac{Nd}{c}\right) \sum_{k=0}^{\infty} \left(\frac{N-1}{N+1}\right)^{2k} \exp\left(4\pi \mathrm{i} f \tfrac{Nd}{c} k\right), \qquad (2.16)$$

where $N \equiv N(f)$ is the complex refractive index (frequency dependent) of the sample and d is its thickness. The first term stands for Fresnel losses due to transmission through the boundaries, the exponential for direct propagation through the sample and the last sum describes the contribution of internal reflections (see Fig. 2.8). The reference transmission (sample = air) then simply yields

$$\mathcal{T}^{\mathrm{ref}}(f) = \exp\left(2\pi \mathrm{i} f \tfrac{d}{c}\right). \qquad (2.17)$$

The transmission T (Eq. (2.13)) is thus related to the refractive index N by

$$T(f) = \frac{4N}{(N+1)^2} \exp\left(2\pi \mathrm{i} f \tfrac{d}{c}(N-1)\right) \sum_{k=0}^{P} \left(\frac{N-1}{N+1}\right)^{2k} \exp\left(4\pi \mathrm{i} f \tfrac{d}{c} k\right). \qquad (2.18)$$

As we are dealing with a time-domain method, we can sometimes (usually for thick samples) resolve the internal reflections of the transients in the sample (see Fig. 2.9*a*). This enables us to apply temporal windowing to the measured waveform and construct the transmission using only specific echoes: only corresponding terms are taken into account in the sum in Eq. (2.18). When the internal reflections cannot be resolved (usually for *thin* samples), it is necessary to sum up to infinity.

The final step is the solution of the inverse problem, i.e. extraction of the refractive index N from the transmission T. A fast numerical procedure for its calculation is described in [62]. For samples where the temporal echoes are well resolved, the thickness of the sample can be also refined from the THz results [63] — this allows further refining of the refractive index, too.

FIGURE 2.8: Meaning of the terms in Eq. (2.16).

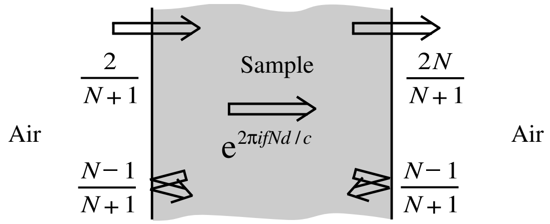

FIGURE 2.9: (a) Internal reflections in a dispersive sample. The spatial separation of echoes is used only for their graphical resolution; practically, it vanishes. The waveform reflected from the sample is not drawn for simplicity. (b) The reflections can be resolved in thick samples, thus we may apply temporal windowing. The numbering of echoes coincides with the k value indexing terms in the sum in Eq. (2.18).

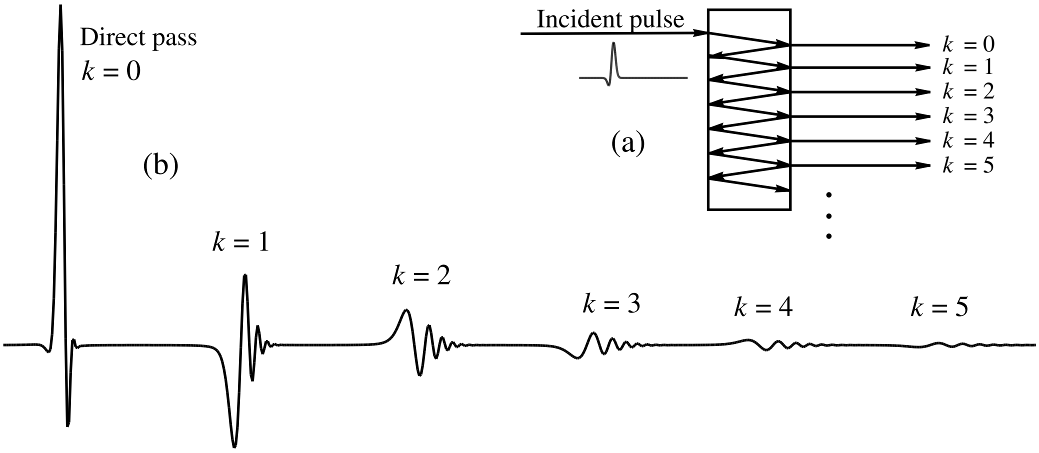

2.3.2 Reflection spectroscopy

There are only few differences in reflection geometry (Fig. 2.7*b*) comparing to the transmission setup. Also the measured quantities are very similar: from the reflectivity R defined as

$$R(f) = \frac{E^{\text{sam}}_{\text{meas}}(f)}{E^{\text{ref}}_{\text{meas}}(f)}, \tag{2.19}$$

it is in principle possible to extract the complex refractive index.

In frame of this diploma work, we made an evaluation of systematic errors in $N = n + \mathrm{i}\kappa$ due to misalignment of experimental setup in view of potential applications of the THz reflection spectroscopy. If an ideal mirror is used as a reference sample, the expressions for reflectivity R are

$$R = \frac{N^2 \cos\theta - \sqrt{N^2 - \sin^2\theta}}{N^2 \cos\theta + \sqrt{N^2 - \sin^2\theta}} \quad \text{TM polarization} \tag{2.20}$$

$$R = \frac{\cos\theta - \sqrt{N^2 - \sin^2\theta}}{\cos\theta + \sqrt{N^2 - \sin^2\theta}} \quad \text{TE polarization,} \tag{2.21}$$

where θ is the angle of incidence of the THz beam. However, the extracted refractive index is significantly affected even by extremely small changes of the optical path of THz beam. These changes will take place at least due to replacement of the sample by the reference mirror. Let us assume that the path increases by the length l. A displacement L of the sample with respect to the reference mirror may cause a change $L/\cos\theta$ in the optical path. The relation between the true reflectivity R and the measured one R^{meas} will be thus

$$R^{\text{meas}} = \exp\left(2\pi \mathrm{i} f \tfrac{l}{c}\right) R(N) = \exp\left(2\pi \mathrm{i} f \tfrac{L}{c\cos\theta}\right) R(N). \tag{2.22}$$

In order to evaluate the error due to the displacement to the first order in L, we have to calculate the derivative $\mathrm{d}N/\mathrm{d}L$. This can be simply done using theorems about the derivative of implicit and inverse functions:

$$\frac{\mathrm{d}N}{\mathrm{d}L} = -\frac{2\pi \mathrm{i} f}{c\cos\theta} \cdot \frac{R}{\frac{\mathrm{d}R}{\mathrm{d}N}}. \tag{2.23}$$

After substitution for R we obtain

$$\text{TM:} \quad \frac{\mathrm{d}N}{\mathrm{d}L} = \frac{2\pi \mathrm{i} f}{c\cos\theta} \cdot \frac{\sqrt{N^2 - \sin^2\theta}}{2N\cos\theta} \cdot \frac{N^4\cos^2\theta - N^2 + \sin^2\theta}{2\sin^2\theta - N^2} \tag{2.24}$$

$$\text{TE:} \quad \frac{\mathrm{d}N}{\mathrm{d}L} = \frac{2\pi \mathrm{i} f}{c\cos\theta} \cdot \frac{\sqrt{N^2 - \sin^2\theta}}{2N\cos\theta} \cdot (1 - N^2) \tag{2.25}$$

Primarily, these expressions predict unacceptable sensitivity to displacement of the sample for big angles of incidence via $1/\cos^2\theta$ behaviour. Second, the error scales linearly with frequency, and grows as N^2 for higher N. For samples with very low losses ($\kappa \to 0$), the expressions are purely imaginary. This implies, that the real part of the refractive index is not significantly affected by the displacement. However, the effect of the displacement on the absorption is high, and is depicted in Fig. 2.10.

Behaviour of errors for lossy samples is more complicated. However, it is possible to draw a set of refractive indices leading to the same modulus of the reflectivity. These points differ only by the phase of reflectivity, which is via Eq. (2.22) related to different displacements of the sample. Some examples of these sets are depicted in Fig. 2.11 (p. 28). It is evident, that as the samples become lossy, both parts of the complex refractive index become affected by the displacement. Expansion of the error in refractive index to the first order can be justified only for very small displacements.

Due to these problems, the performance of reflection measurements is still questionable. Only few successful measurements of the complex refractive index via reflection spectroscopy were done [64–67].

FIGURE 2.10: Influence of a displacement of the sample: a special case of sample with negligible absorption: The graph shows the expressions $\frac{1}{f}\frac{\mathrm{d}\kappa}{\mathrm{d}L}$ given by Eq. (2.24) and (2.25).

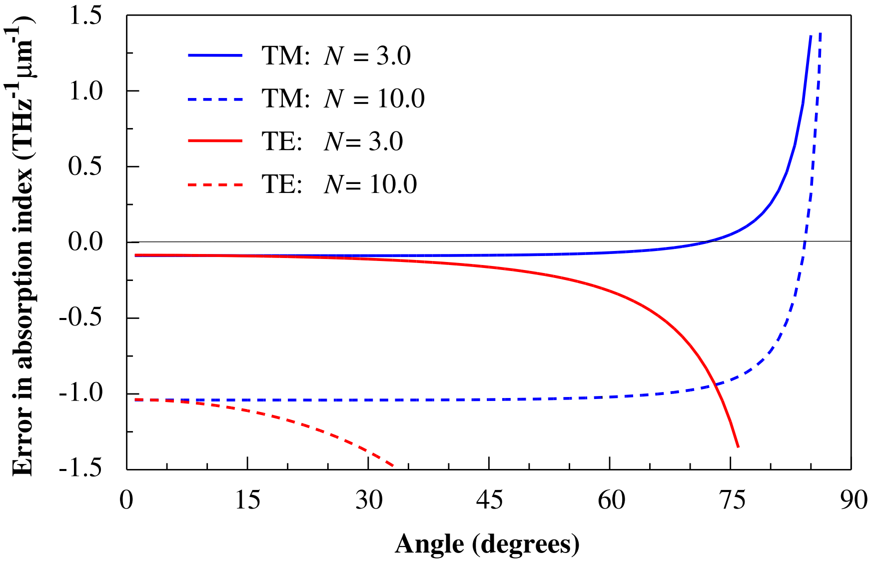

2.3.3 Emission spectroscopy

The THz emission spectroscopy investigates ultrafast processes which lead to the THz pulse radiation. The shape of the THz waveform emitted from the sample after the irradiation by ultrashort optical pulse holds an information about transient current density or polarization (Eq. (2.3) or (2.2)). This technique was used for example to investigate quantum structures [68], semiconductor surfaces [16], cold plasma [69] and influence of magnetic field on carrier dynamics [70].

The measured waveform E_{meas} generally differs from the emitted one E_{emit} due to the reshaping during propagation described by a function $\mathcal{P}$ and due to the detector response $\mathcal{D}$:

$$E_{\text{meas}}(f) = E_{\text{emit}}(f) \cdot \mathcal{P}(f) \cdot \mathcal{D}(f). \tag{2.26}$$

This makes the interpretation a little tricky. In several cases, when the emitted spectrum is narrow and only the central frequency is of the primary interest (e.g. Bloch oscillations [5]), both the influence of propagation and detector response may be estimated only very roughly. However, when the emitted spectrum is broadband, or when directly the *true* time evolution of the current density or polarization has to be studied, a careful determina-

Figure 2.11: Graph of complex refractive indices corresponding to the same modulus of the reflectivity. The angle of incidence is $\theta = 45°$. The frequency is supposed to be 1 THz, the distance between points corresponds to displacement of $1\,\mu$m. Different colours correspond to different modulus of reflectivity. The graphs are plotted for (a) TM and (b) TE polarization.

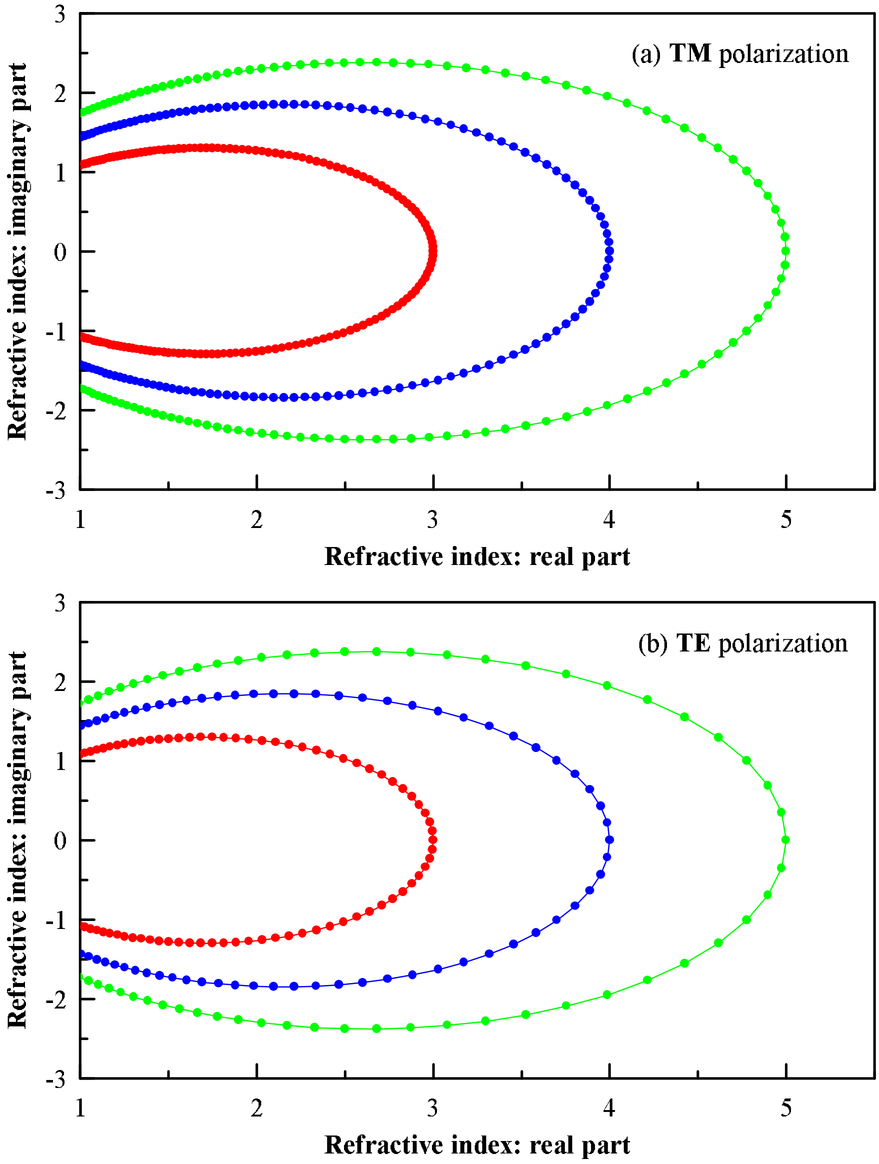

tion of the influence of the propagation $\mathcal{P}$ and the detector $\mathcal{D}$ becomes an important point for correct interpretation of measured waveforms.

The situation in the frequency domain is similar to that in transmission or reflection spectroscopy. We are able to determine the complex spectrum $E_{\text{emit}}(f)$ in a limited frequency range. This prevents from a complete reconstruction of the emitted waveform $E_{\text{emit}}(t)$ in the time domain as it is related to $E_{\text{emit}}(f)$ via integral transformation. The best scheme thus seems to be a construction of a theoretical model for $E_{\text{emit}}(t)$, which enables to predict the measured waveform via inverse Fourier transformation of Eq. (2.26). This allows a direct comparison with the experimental data.

The third part of this work concerns the development of this technique and its applications to the investigation of ultrafast dynamics in semiconductors, i.e. especially to the evolution of the current density.

2.3.4 Optical pump – THz probe experiments

In an optical pump – THz probe experiment the changes of the response of the sample induced by an intense ultrashort optical excitation are studied via probing the sample by a delayed THz pulse. The setup (see Fig. 2.7*d*) is based on the transmission geometry; an optical excitation beam is added. The excitation and THz beams are perfectly synchronized as they may be triggered by the same ultrashort laser pulse. This method was successfully applied to several problems including carrier dynamics in semiconductors [53], superconductors [71] and liquids [72].

In this type of experiments, generalized response function is usually studied. In addition to the equilibrium experiments, it also takes into account the causal influence of the excitation beam. Thus the polarization may be described [73] by the formula

$$P(t, t_{\text{e}}) = \varepsilon_0 \int_{-\infty}^{t} E(t')\chi(t - t', t - t_{\text{e}})\, \mathrm{d}t', \tag{2.27}$$

where t_{e} is the time of the excitation of the sample and t the time of measurement (sampling beam arrival). Unlike in equilibrium situation, the integral in Eq. (2.27) does not represent a convolution. That's why application of the Fourier transformation in the time t does not lead to a product of electric intensity and susceptibility. This in turn prevents from using the formalism developed for the transmission spectroscopy.

2.4 Applications in condensed matter physics

2.4.1 Quantum structures

The THz radiation can be produced by charge oscillations due to **quantum beats**. These can occur already in a three-level system, whose two levels are very close, thus the beating frequency may lie in the THz spectral range. The THz emission then proves directly these charge oscillations. This phenomenon was first directly observed in double quantum wells [4]. The emission from a single quantum well due to the excitation of the light hole and heavy hole excitons was also reported [68].

Long ago it was predicted, that an electron in a periodic potential in the presence of uniform electric field E would periodically oscillate with the Bloch frequency $f_{\mathrm{B}} = eEd/h$, where d is the period of potential. Due to the scattering, the coherence of the Bloch states is destroyed before a single oscillation cycle is completed. However, Esaki and Tsu expected, that these Bloch oscillation should also occur in superlattices. The first direct observation of this phenomena was reported in 1993 by Waschke et al. [5] using THz emission spectroscopy. The spectrum emitted from these types of emitters is usually narrower than that of conventional emitters.

2.4.2 Dielectrics

For studies performed on dielectrics in THz region, the THz time-domain transmission spectroscopy is commonly used. It establishes connection between radiofrequency and infrared regions. The number of investigated materials is high, let us name at least common substrates like e.g. sapphire, quartz and fused silica [74]. For many materials, this spectral range contains precious information about the behaviour of low-frequency (soft) polar phonons and relaxational mechanisms (central modes) which are often responsible for structural (namely ferroelectric) phase transitions. Recently, the THz time-domain spectroscopy was applied to the study of high-permitivity microwave ceramics [75], where it makes a feedback to the technological protocols: (i) The presence of a second unwanted phase in the ceramic samples may cause additional peaks in the submillimetre region [76]; (ii) intrinsic losses of the ceramics in the microwave region can be estimated directly through THz time-domain spectroscopy [75]. An important phenomenon contributing to dielectric properties in the THz region is a strong mixing of transversal optic phonons and photons near frequencies of transversal optic phonons: the technique offers a possibility to characterize precisely the polariton dispersion and dephasing [77]. THz spectroscopy is also sensitive to presence of residual free carriers and defects [74].

2.4.3 Semiconductors

Concerning the equilibrium, the THz frequency range is particularly interesting for doped semiconductors, as the majority of the oscillator strength of the Drude conductivity falls here. This is important, as it allows noncontact characterization of doping concentrations and scattering rate of the free carriers using THz transmission spectroscopy. The pioneering studies of GaAs, silicon and germanium were performed by Grischkowsky et al. [74].

THz based methods are also successfully used for the investigation of the dynamics in semiconductors. For this purpose, the optical pump – THz probe or THz emission spectroscopy is used. Nowadays, there is a rapidly increasing number of studies concerning the free carrier dynamics [53, 69, 78–80] and influence of magnetic field on it [70, 81].

2.4.4 Liquids

The phenomena in liquids with a time-scale falling into the THz region are especially molecular motion and bulk dielectric relaxation. These features can be very simply observed in polar liquids due to the strong interaction between the electromagnetic radiation and molecular dipoles. However, in nonpolar liquids the absorption related to dipoles induced by collisions becomes the dominant process. The important liquids like water [59,82], $CHCl_3$, CCl_4 and their mixtures [83] and methanol, ethanol, 1-propanol and liquid ammonia [59] were investigated by THz transmission spectroscopy.

Nowadays, the studies of a solvent dynamics due to the charge transfer of optically excited solute becomes a challenging experimental problem. This dynamics can be composed of various phenomena including vibrations, solvation or e.g. conformational changes in proteins. Up to now, only few preliminary measurements concerning *n*-hexane [84], betain [72, 85] and *p*-nitroanilin [72] were performed.

Part 3

Study of GaAs grown at low temperatures by THz emission spectroscopy

The GaAs grown by molecular beam epitaxy at low temperatures (LT GaAs) is an important ultrafast photoconductive material. First, it was studied for its semi-insulating property, which is important for the fabrication of buffer layers in GaAs MESFETs, as it provides excellent device isolation, thus eliminating backgating effects and reducing short-channel effects in GaAs MESFETs with submicron-long gates [86]. Further structural investigations were then done [87,88] and ultrafast dynamics in LT GaAs was observed [89] and used to construct a picosecond switch [90].

Nowadays, the properties of LT GaAs are further being improved (different deposition and annealing conditions, beryllium doping [91]). A detailed understanding of the mechanisms of the ultrafast response is thus a crucial point that allows to optimize the elaboration and to control the properties.

3.1 Structure of LT GaAs

GaAs films with good crystalline and electric quality are grown by molecular beam epitaxy at substrate temperatures $\sim$ 600°C at the growth rate $\sim 1\,\mu$m/h. However, decreasing the substrate temperature below 500°C and preserving the growth rate dramatically changes the property of GaAs layers [92] — such material is then referred as low-temperature grown GaAs. Further annealing above 450°C of these layers also significantly affects their properties [93].

A variety of characterization techniques was employed for investigating

LT GaAs. For structure analysis, let us name X-ray studies [88, 94], transmission electron microscopy [88, 95–97], scanning tunnelling microscopy [98], Auger electron microscopy [94], electron paramagnetic resonance and related techniques [93, 99] and slow positron spectroscopy [100]. The optical and electronic properties were studied namely by resistivity and breakdown measurements [101, 102], infrared absorption spectroscopy [94, 99, 102, 103], Hall effect [94, 102, 103], photoluminescence [104] and magnetic circular dichroism of absorption [99].

Though the first investigations started already about 1989 [88], there are still doubts about the structure of both as-grown and annealed LT GaAs [94]. The microstructure of LT GaAs is primarily determined by the growth temperature, arsenic pressure during the growth and by the annealing conditions (temperature and time) [87, 93, 105, 106]. Anyway, the common property of this material is an exceptionally high excess of arsenic (like 1 %). It can be incorporated in the crystal matrix in a form of arsenic antisite point defects, arsenic interstitials, gallium vacancies and arsenic clusters. Schematic band structure of LT GaAs is depicted in Fig. 3.1.

FIGURE 3.1: Scheme of the band structure of (a) GaAs and (b) as-grown LT GaAs. The annealed LT GaAs differs from this scheme by lower density of donors and presence of arsenic clusters. All values correspond to measurements at room temperature.

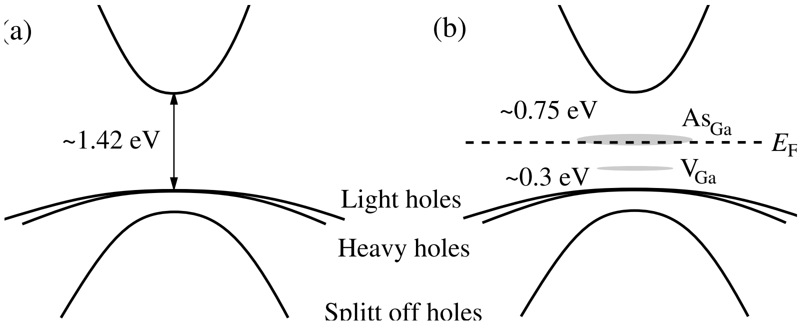

Concerning the ultrafast response of this material, the most important seems to be the concentration of ionized arsenic interstitial point defects (As^+_{Ga}). For low concentrations of photogenerated carriers, only the dynamics of electrons is important due to low mobility of holes. For high concentrations of carriers the traps (As^+_{Ga}) can be filled with electrons. The rate of the dynamics thus becomes determined by the rate of further ionization of traps, which is closely related to the rate and mechanism of capturing the holes. In this situation, the dynamics of holes may be dominant.

In **as-grown** LT GaAs, the most important defect is arsenic antisite, which acts as a deep donor. The increase of the lattice parameter is also attributed to this point defect. The gallium vacancies are assumed to act as acceptors, thus partially ionizing the donors, which then serve as traps responsible for the ultrafast behaviour. The dark resistivity in as-grown samples is quite low due to a strong hoping conduction [101]. On the other hand, due to high neutral-defect density, the mobility of photogenerated carriers is low.

Processes in **annealed** LT GaAs seem to be more complicated. The arsenic antisite and arsenic interstitials tend to form precipitates during annealing. Thus it seems, that there is a high-quality GaAs matrix with embedded arsenic precipitates, which behave as metallic clusters. Their wavefunctions do not overlap. This results in a high dark resistivity comparable to the semi-insulating GaAs, and simultaneously in an increase of the mobility of photogenerated electrons comparing to LT GaAs. However, the density of ionized point defects $\mathrm{As}_{\mathrm{Ga}}^{+}$ becomes lower, resulting in longer electron trapping times.

3.2 Investigation of ultrafast properties

There is a great effort to fabricate an ultrafast material with high free carrier mobility and high dark resistivity. In bulk semi-insulating GaAs, the fast dynamics is determined by recombination, which leads to nanosecond carrier lifetimes. In order to shorten the carrier lifetimes, it is necessary to create a high density of traps, i.e. high density of defects. Concerning GaAs, several technologies like impurity doping [107], growth of amorphous material [108] or damage by proton implantation [109] were used. However, growth by molecular beam epitaxy at low temperatures and successive annealing seems to produce a very suitable material [110].

As the carrier lifetime in LT GaAs is usually shorter then 1 ps, rather optical than electric techniques need to be employed for its characterization. Following optical methods offering sufficient time resolution of carrier dynamics are more or less commonly used:

- Time-resolved photoluminescence spectroscopy
- Optical pump – optical probe methods (both reflection and transmission geometry is commonly employed)
- Optical pump – THz probe technique (up-to-day only transmission geometry has been used)
- THz emission spectroscopy (introduced by us).

Signal from **time-resolved luminescence** is related to the product of free electron and hole densities. However, this technique is of very limited usage, as the electron trapping in LT GaAs is a nonradiative process. This results in a very low photoluminescence intensity [92], thus the time resolved luminescence becomes practically nonapplicable technique even at very high carrier densities. On the other hand, it has been shown, that the beryllium doping increases the luminescence intensity: the time resolved luminescence technique can thus be applied only to the investigation of heavily beryllium doped samples [111].

Optical pump – optical probe is probably the most widespread method giving the greatest amount of information. The interpretation of data measured by this method remains a very complex problem. High excitation intensities are required to obtain a measurable signal; it then leads to a large number of secondary effects, which should be accounted to in a model. A very complex study (measurements at different pump – probe wavelengths and intensities) should be carried on in order to draw a reliable picture of the involved processes. In the simplest experimental scheme, pump and probe are degenerate (usually around 800 nm): the pump pulse produces band-to-band transitions and the delayed probe pulse exhibits a delay-dependent decrease of the reflectivity due to the conduction-band filling. On the other hand, large number of effects like electron trapping, electron cooling, trap filling, carrier recombination, Auger recombination, bandgap renormalization and band filling can contribute simultaneously to the measured signal. One needs to take into account namely the trap filling. The most important effects related to high excitation intensities are discussed in [106, 112, 113].

This method is used both in reflection and transmission geometry. By the proper choice of wavelengths of the pump and probe beam, phenomena like carrier cooling, trapping, recombination [114–119] or dynamics of holes [120] were studied. The time resolution of this method is determined only by the length of incident laser pulses. That's why it offers a resolution of tens of femtoseconds.

In **optical pump – THz probe** experiments the free carriers are again generated by the optical pump pulse. However, the THz probe beam is absorbed namely due to the interaction with free carriers. Their concentration and mobility can be simultaneously deduced from the measured data. The measurements show that much lower excitation densities are necessary to obtain a measurable signal. However, the time resolution is determined by the length of the *THz probe pulse*, resulting in a typical value of approximately 400 fs. Recently, this method has been used for investigation of carrier dynamics in LT GaAs [53, 78], GaAs [54] and proton-bombarded InP [79].

The optical pump beam irradiates a *biased sample* in **THz emission**

spectroscopy. As the carriers are being generated, trapped, or accelerated, an emission in THz region occurs. Time resolution of this method is limited by the *response of the sensor* and by the length of the optical pump and sampling pulses, which can in principle lie in the order of tens femtoseconds [3]. Again, it is a method sensitive to free carrier density, and it also allows to determine the mobility if a simple Drude-like behaviour of carriers is assumed. Only low free carrier densities are necessary to produce a reasonable signal. Unlike preceding methods this one requires building electrical contacts.

In our case, the THz emission spectroscopy is especially useful, as we are interested in the determination of free carrier trapping times and their mobilities at low carrier concentrations. This method also offers sufficient time resolution.

3.3 Experimental setup

Our setup for THz-emission measurements is depicted in Fig. 3.2. The whole system is driven by a Ti:sapphire oscillator (wavelength 800 nm, pulse duration 100 fs, repetition rate 76 MHz and mean output power 300 mW). From this beam, 96 % of the power irradiates the emitter under investigation and the remaining part is used in the electrooptic-sampling detection with 1 mm thick $\langle 110 \rangle$ oriented ZnTe crystal. The ellipticity of the sampling beam polarization is measured by a pair of balanced photodiodes.

The experimental setup we have proposed allows to evaluate the detector response and the function describing the influence of propagation in Eq. (2.26). No THz focusing optics is used, as the description of the THz pulse propagation is very difficult even in very simple cases [121]. The whole path of the THz beam is enclosed in a box pumped with nitrogen in order to avoid absorption on water vapour which results in oscillatory tails of the measured waveforms.

In order to reduce effects caused by fluctuations of the laser power and/or polarization, two additional reference signals are recorded. The first one monitors the power of the laser (diode D_3) and the second one measures power of the sampling beam reflected from the pellicle beam splitter. As the THz signal is negligible comparing to the optical bias of the diodes, signal from D_1 or D_2 can be used instead. In our experiments, the signal from the lock-in amplifier was consequently normalized by the product of the signals in D_2 and D_3. In order to justify the first reference, we measured at different excitation densities and checked, that the signal varies linearly with the optical fluence. Also Eq. (3.2) and following support this view. Justification of the latter reference is obvious from the section about electrooptic sampling, Eq. (2.11).

Figure 3.2: Scheme of experimental setup for emission measurements.

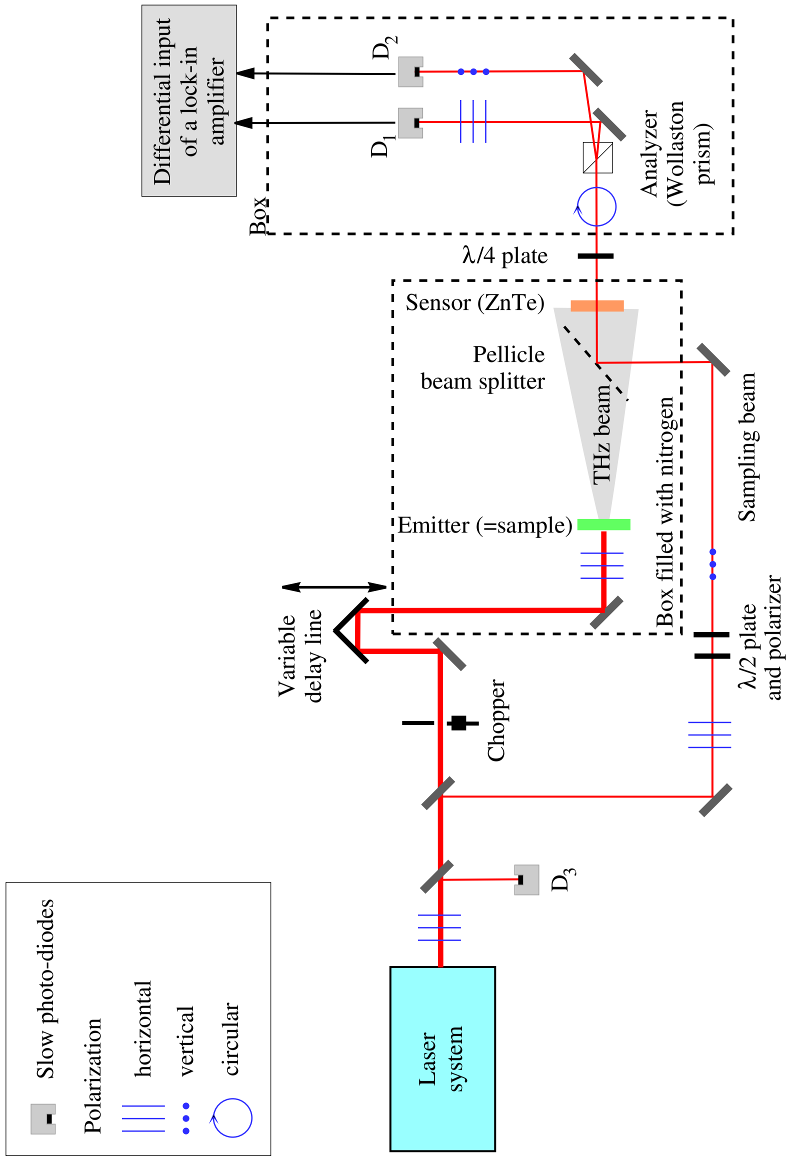

Samples were grown on 0.5 mm semi-insulating GaAs substrate. After deposition of a 72.5 nm GaAs buffer layer at 600 °C, the 1.3 μm layer was grown at substrate temperature T_g at the growth rate 1.76 μm/h. Four samples grown at temperatures $T_\mathrm{g} = 175$, 200, 225 and 250 °C were investigated. All the samples were annealed for 10 min at 600 °C. We used two different spacings (4 and 6 mm) of gold planar electrodes, which were prepared by sputtering. The bias voltage applied to them during the experiment was ranging from 800 to 2500 V. The space between electrodes was irradiated by the mentioned femtosecond laser source with different pulse energies. The commonly used free-electron densities were in the range 10^{14} to $10^{15}\,\mathrm{cm}^{-3}$. All measurements were performed under nitrogen atmosphere without any optics focusing the THz beam. Different distances between the emitter and sensor were tried in order to avoid eventual near field effects.

3.4 Model of dynamics in LT GaAs

The most important fast processes that can occur in LT GaAs due to the absorption of an infrared 800 nm photon are depicted in Fig. 3.3. (1) The photon generates an electron-hole pair or (2) reexcites the trapped electron up to the conducting band. An electron in the conducting band can (3) recombine, (4) be trapped or (5) cooled. Finally, the electron in a trap can recombine with a hole (6).

FIGURE 3.3: Processes taking place due to the absorption of an infrared photon.

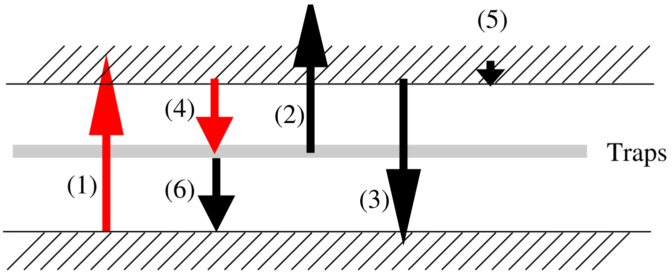

From Eq. (2.3) it is obvious, that the quantity we are able to measure is current density, i.e. we are able to determine evolution of the product of the carrier density n and the carrier velocity v:

$$j(t) = en_\mathrm{e}(t)v_\mathrm{e}(t) + en_\mathrm{h}(t)v_\mathrm{h}(t), \tag{3.1}$$

where indices e and h denote electrons and holes respectively. As our excitation density (below $10^{15}\,\mathrm{cm}^{-3}$) is much lower than the density of traps

($\lesssim 10^{18}\,\mathrm{cm}^{-3}$), we can neglect the changes in the occupancy of traps and thus assume the free-electron lifetime to be constant. Also the occupancy of both conduction and valence band does not change significantly, thus the rate of the carrier generation depends only on the optical fluence. Finally, we neglect the contribution of holes [122], as their mobility is much lower than that of electrons. This suggests a very simple equation describing the evolution of free electron density (from now, n and v denote the free electron density and velocity respectively):

$$\frac{\mathrm{d}n}{\mathrm{d}t} = -\frac{n}{\tau_\mathrm{c}} + G(t, \boldsymbol{r}), \tag{3.2}$$

where τ_c is the free electron trapping time and G the rate of electron generation, which is proportional to the intensity of the optical pulse. We are interested only in phenomena which change the dynamics on a time scale $\sim 10\,\mathrm{ps}$ or shorter, hence both the recombination rate ($\sim 160\,\mathrm{ps}$ in traps [51] and $\lesssim 2\,\mathrm{ns}$ in bulk GaAs [54]) and the diffusion processes were also completely neglected. Neither the surface recombination can be significantly involved in the dynamics as the diffusion is very slow process [54].

We based the description of evolution of the free-electron velocity on the Drude-Lorentz model, which was already successfully applied to a similar problem [8]:

$$\frac{\mathrm{d}v}{\mathrm{d}t} = -\frac{v}{\tau_\mathrm{s}} + \frac{eE_\mathrm{loc}(t, \boldsymbol{r})}{m} - \frac{vG(t, \boldsymbol{r})}{n}. \tag{3.3}$$

Here, τ_s is the velocity relaxation time, m the effective mass and $E_\mathrm{loc} = -\nabla\varphi$ the local electric field. The Drude-Lorentz model for the velocity can be well justified in our case, as the electron energy is very low and the screening is negligible due to low carrier densities involved in the experiments. The last term was added in order to correctly describe the mean velocity v of free carriers during the generation process. The mean velocity of the free carriers *just generated* is zero thus the mean velocity of *all* free carriers is decreased by the generation process. This treatment is necessary when the carrier scattering time τ_s is longer or comparable with the excitation pulse length. We do not construct an equation for the whole vector of velocity, as the carriers move dominantly in the direction of the bias electric field.

The low-temperature grown (LTG) layer is not thick enough to absorb the whole incident power (see Fig. 3.4), but a significant amount of radiation penetrates to the bulk GaAs. Thus there will be a contribution to the THz radiation from the transient currents in the bulk. Later, it will be evident that this allows determination of the relative carrier mobility of the LTG layer. The same model (Eq. (3.2) and (3.3)) can be employed for the carrier

FIGURE 3.4: Distribution of the incident power.

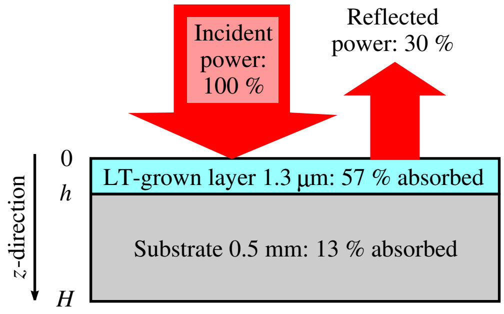

dynamics description in bulk GaAs assuming the carrier lifetime to be much greater than that in the LTG layer. The carrier scattering time in bulk GaAs, $\tau_\mathrm{s} = 270\,\mathrm{fs}$ was taken from [123]. Effective masses in bulk and LTG layer are assumed to be the same. Let us summarize the equations we should solve (the upper index L or B refers to the LTG layer or to the bulk GaAs):

$$\text{LTG layer:} \quad \frac{\mathrm{d}n^\mathrm{L}}{\mathrm{d}t} = -\frac{n^\mathrm{L}}{\tau_\mathrm{c}^\mathrm{L}} + G^\mathrm{L}(t,\boldsymbol{r}) \tag{3.4}$$

$$\frac{\mathrm{d}v^\mathrm{L}}{\mathrm{d}t} = -\frac{v^\mathrm{L}}{\tau_\mathrm{s}^\mathrm{L}} + \frac{eE_\mathrm{loc}(t,\boldsymbol{r})}{m} - \frac{v^\mathrm{L}G^\mathrm{L}(t,\boldsymbol{r})}{n^\mathrm{L}} \tag{3.5}$$

$$\text{Bulk:} \quad \frac{\mathrm{d}n^\mathrm{B}}{\mathrm{d}t} = -\frac{n^\mathrm{B}}{\tau_\mathrm{c}^\mathrm{B}} + G^\mathrm{B}(t,\boldsymbol{r}) \tag{3.6}$$

$$\frac{\mathrm{d}v^\mathrm{B}}{\mathrm{d}t} = -\frac{v^\mathrm{B}}{\tau_\mathrm{s}^\mathrm{B}} + \frac{eE_\mathrm{loc}(t,\boldsymbol{r})}{m} - \frac{v^\mathrm{B}G^\mathrm{B}(t,\boldsymbol{r})}{n^\mathrm{B}} \tag{3.7}$$

The remaining quantity in the model which is necessary to describe is the local electric field. Generally, it is necessary to solve it from Poisson's equation (for example, to describe the effects of screening which may occur for higher excitation densities). Together with system (3.4–3.7), it forms a system of coupled equations, the solution of which would be very complicated and time consuming. However, far from the emitter, the emitted waveform can be related to the *total* current I (see Eq. (2.3)):

$$E_\mathrm{THz}(t) \propto \frac{\partial I(t)}{\partial t}. \tag{3.8}$$

In the following paragraphs we prove, that under reasonable assumptions the total current density can be calculated in a such way, that any spatial dependence in the system (3.4–3.7) can be omitted.

Obviously, the total current I can be written as a sum of contributions from LTG layer and bulk:

$$\begin{aligned} I(t) &= \int\limits_{\text{sample}} j(t,S,z)\ \mathrm{d}V = \int\limits_{\mathrm{L}} j^{\mathrm{L}}(t,S,z)\ \mathrm{d}V + \int\limits_{\mathrm{B}} j^{\mathrm{B}}(t,S,z)\ \mathrm{d}V = \\ &= \int\limits_{\text{surface}} \left(\int\limits_0^h j^{\mathrm{L}}(t,S,z)\ \mathrm{d}z + \int\limits_h^H j^{\mathrm{B}}(t,S,z)\ \mathrm{d}z \right) \mathrm{d}S \end{aligned} \tag{3.9}$$

When the excitation pulse irradiates the surface perpendicularly, its spatial and temporal profile can be factorized to the form

$$G(t,\boldsymbol{r}) = g(t)f(S)\exp\left(-\alpha z\right), \tag{3.10}$$

where α is the absorption coefficient, g describes the temporal and f the spatial profile of the excitation pulse. As the free-electron density can be assumed to vanish before the pulse arrival, the solution of Eq. (3.2) can be factorized as well:

$$n(t,\boldsymbol{r}) = \hat{n}(t)f(S)\exp\left(-\alpha z\right), \tag{3.11}$$

where $\hat{n}(t)$ is its temporal profile, which is in general different from that of the excitation pulse.

We neglect the screening of the local electric field. The local electric field is then time independent. Let us assume, that its spatial profile can be factorized as

$$E_{\mathrm{loc}}(t,\boldsymbol{r}) = E\cdot s(S)k(z), \tag{3.12}$$

where the dimensionless functions s and k represent the surface and depth profile and E stands for the field strength. In this situation, also the velocity v given by Eq. (3.3) can be factorized as well:

$$v(t,\boldsymbol{r}) = \hat{v}(t)s(S)k(z), \tag{3.13}$$

where $\hat{v}$ is the temporal profile of the velocity. Substitution of Eq. (3.11) and (3.13) to Eq. (3.9) yields

$$I(t) = eE\int\limits_{\mathrm{S}} f(S)s(S)\left(\hat{n}^{\mathrm{L}}(t)\hat{v}^{\mathrm{L}}(t)\int\limits_0^h \mathrm{e}^{-\alpha z}k(z) + \hat{n}^{\mathrm{B}}(t)\hat{v}^{\mathrm{B}}(t)\int\limits_h^H \mathrm{e}^{-\alpha z}k(z) \right) \tag{3.14}$$

Obviously, if the local electric field does not vary with the depth z significantly on a dimension comparable with the absorption length, this equation becomes

$$I(t) \propto \beta^{\mathrm{L}}j^{\mathrm{L}}(t) + \beta^{\mathrm{B}}j^{\mathrm{B}}(t), \tag{3.15}$$

i.e. it is a linear combination of contributions from the known bulk material and LTG layer under the investigation, with the weights equal to the amount of optical power absorbed in appropriate parts of the sample. The goal is that the overall proportionality constant is independent of time. Let us recall the assumptions under which this expression is valid:

1. The fast dynamics is described by Eq. (3.2) and (3.3) in the whole sample. That's why the performed factorization is possible.
2. The local electric field does not vary significantly with the depth. This assumption may not be fully satisfied near electrodes. However, most of the THz radiation is generated elsewhere, thus this violation should not influence the results.

Our model is fully determined by three parameters, which we fit from the measured data. Two of them, the carrier trapping time $\tau_\mathrm{c}^\mathrm{L}$ and the carrier scattering time $\tau_\mathrm{s}^\mathrm{L}$ are directly related to the properties of the LTG layer. The last one is a proportionality constant, which is related to the intensity of the THz radiation. As we measured only its temporal profile and not its absolute value, this parameter does not hold any information about the properties of the sample.

3.5 Influence of free space propagation and detection

In order to compare the measured waveforms and the model, it is necessary to describe the influence of the free space propagation and the detection (Eq. (2.26)). In our experimental setup, we measure under the nitrogen atmosphere, thus eliminating the absorption caused by water vapour [124]. We also did not use any focusing optics, because describing its influence is difficult even in very simple case [121]. However, this lowered the signal, and consequently the signal to noise ratio became poorer. The only influences we cannot omit are thus the free space propagation and the response of the detector.

3.5.1 Propagation of elliptic beam

We suppose that the THz radiation pattern from the emitter may be well approximated by the Gaussian profile, due to the same pattern of the exciting laser beam. In order to describe the influence of propagation by the distance

z, we have to calculate the diffraction integral [9]

$$E(f;x,y,z) = \iint \frac{1}{z} E_0(f;x',y') \exp\left(-\mathrm{i}kr + \mathrm{i}k\frac{xx'+yy'}{r}\right)\,\mathrm{d}x'\,\mathrm{d}y' \quad (3.16)$$

where $k = 2\pi f/c$ is the wave-vector, $r = \sqrt{x^2+y^2+z^2}$ and E_0 is the pattern of electric field at $z = 0$. Substitution for the initial pattern

$$E_0(f;\,x,y) = E_0(f)\exp\left(-\tfrac{x^2}{w_x^2} - \tfrac{y^2}{w_y^2}\right) \quad (3.17)$$

and a few manipulations yield

$$E(z,f) = E_0(f)\frac{\mathrm{i}\pi f}{zc}\frac{w_x}{\sqrt{1+\frac{\mathrm{i}\pi f w_x^2}{zc}}}\frac{w_y}{\sqrt{1+\frac{\mathrm{i}\pi f w_y^2}{zc}}} \xrightarrow[z\to\infty]{} \frac{\mathrm{i}\pi f}{zc}w_x w_y. \quad (3.18)$$

Here only the on-axis field was calculated for simplicity. In our experimental setup $w_x = 1.8\,\mathrm{mm}$, $w_y = 1.2\,\mathrm{mm}$ and $z = 5$ to $15\,\mathrm{cm}$. Though it seems that the expression under the square root are not negligible, it was experimentally shown that the approximation marked by arrow holds very well [121].

3.5.2 Response of electrooptic detector

The response of the electrooptic detector was already studied in the time domain [45, 47]; very general situation was solved by Gallot et al. [125]. For our purposes, we derive the response function in the frequency domain. We take into account (a) Gaussian sampling pulse, (b) THz and optical dispersion in the sensor and (c) phase-matching effects. The shape of the THz pulse evolves according to the formula (see Fig. 2.8)

$$E(z,f) = E_0(f)\cdot\frac{2N}{N+1}\cdot\exp\left(\frac{2\pi\mathrm{i}fzN}{c}\right), \quad (3.19)$$

where $E_0(f)$ is a THz wave irradiating the sensor, N is the refractive index of the sensor and z is the path travelled in the sensor. The middle term stands for Fresnel-reflection losses and the last one for the propagation in the sensor. The refractive index N is in principle frequency dependent. As the intensity of the THz field is low, the detected signal can be written as (see Eq. (2.11))

$$E_{\mathrm{meas}} \propto \Delta I(t) \propto \int_0^L \int_{-\infty}^{\infty} I(t-t',z)E(z,t')\,\mathrm{d}t'\,\mathrm{d}z, \quad (3.20)$$

where I is the intensity of the sampling beam, L thickness of the sensor and t the delay between the sampling and THz pulse. We assume the sampling pulse to be Gaussian:

$$I(t,z) \propto \frac{1}{\sqrt{\tau}} \exp\left(\frac{t - zN_\mathrm{g}/c}{\tau}\right), \tag{3.21}$$

where τ is related to the width of the pulse and N_g is the group refractive index of the sensor. We substitute Eq. (3.21) and (3.19) to Eq. (3.20) and apply the Fourier transformation to Eq. (3.20). This leads to the response of the electrooptic detection $\mathcal{D}$:

$$\begin{aligned}\mathcal{D}(f) = \frac{E_\mathrm{meas}(f)}{E_0(f)} &\propto \\ &\propto \frac{2N}{N+1} \mathrm{e}^{-(\pi\tau f)^2} \frac{\sin\left((N - N_\mathrm{g})\pi f \frac{L}{c}\right)}{(N - N_\mathrm{g})\pi f \frac{L}{c}}\ \mathrm{e}^{\pi \mathrm{i} f (N - N_\mathrm{g}) \frac{L}{c}}.\end{aligned} \tag{3.22}$$

The refractive index $N(f)$ of ZnTe in the THz range was measured in our laboratory by THz time-domain spectroscopy. This is necessary, as due to different conductivity of each particular crystal these indices may differ quite significantly. We also measured the group refractive index N_g. The value agrees very well with the previously reported one [126]. The amplitude of the response given by Eq. (3.22) for our detector is plotted in Fig. 3.5.

FIGURE 3.5: Response of the electrooptic detector with 1 mm thick ⟨100⟩ oriented ZnTe crystal. The full-width half-maximum of the sampling pulse was 110 fs and the central wavelength 800 nm.

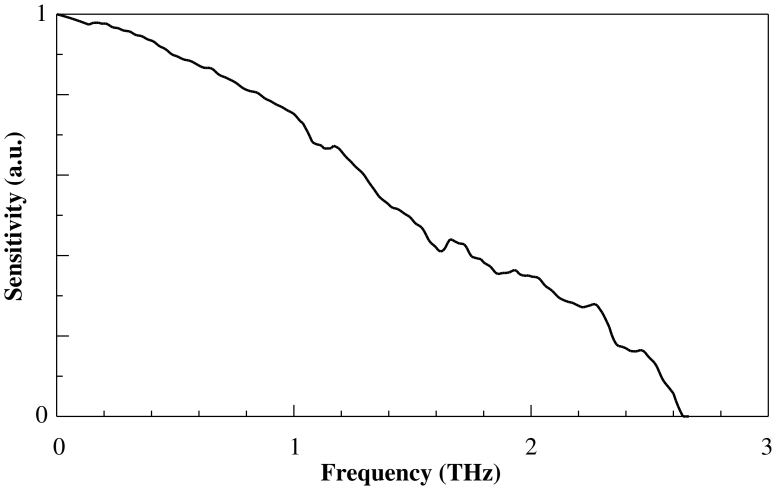

3.6 Results and discussion

The current in Eq. (3.15) was computed by numerical solution of the system of differential equations (3.4–3.7) by the fourth order Runge-Kutta method. After that we performed the convolution (Eq. (2.26)) with the free space propagation (Eq. (3.18)) and with the detector response (Eq. (3.22)). These time-domain data were then fitted to the experimental results by the least square method. The measured data along with corresponding fits are depicted in Fig. 3.7–3.10 (pp. 48–49). Decomposition of the fit to the contribution from the substrate and the LT layer is also presented.

In order to check our model, we varied several parameters involved in the experiment. We checked, that the shape of measured waveforms was independent of the optical pulse intensity over a decade, spacing between the electrodes (4 and 6 mm), applied bias voltage (in the range 800 to 2500 V), distance between the emitter and the sensor (varied from 5 to 15 cm) and spatial profile of the optical beam (it was broadened by insertion of a concave lens). The THz signal scaled linearly with the applied bias voltage and the intensity of the optical beam (the estimated carrier concentration was varied in the range 10^{14} and $10^{15}\,\mathrm{cm}^{-3}$). All these facts corroborate our model.

The results of fits (i.e. free-electron lifetimes, scattering times and mobilities) are summarized in Tab. 3.1 and also plotted in Fig. 3.6. Both quantities have similar values as those reported previously [101, 127]. We attribute the higher mobility of the sample grown at 200°C to the lower precision of the measurement and we do not consider it as to be the property of the sample. The fit for the sample grown at 175°C yielded so high tolerance for its mobility, that only the carrier lifetime is presented. Also its precision is significantly worse. The trapping time τ_c can be related to the density of defects N by the formula [122]

$$\tau_\mathrm{c} = \frac{1}{N v_\mathrm{th} \sigma} = \frac{1}{\pi N R^2 s v_\mathrm{th}}, \tag{3.23}$$

TABLE 3.1: Carrier lifetimes, mobilities and carrier scattering times obtained via THz emission spectroscopy.

T_g (°C)	τ_c (fs)	μ ($\mathrm{cm^2V^{-1}s^{-1}}$)	τ_s (fs)
250	660 ± 50	2250 ± 100	87 ± 4
225	450 ± 50	2350 ± 100	91 ± 4
200	375 ± 50	3000 ± 500	115 ± 20
175	280 ± 100	$\cdots$	$\cdots$

FIGURE 3.6: Dependence of free-electron lifetimes on growth temperature in LT GaAs.

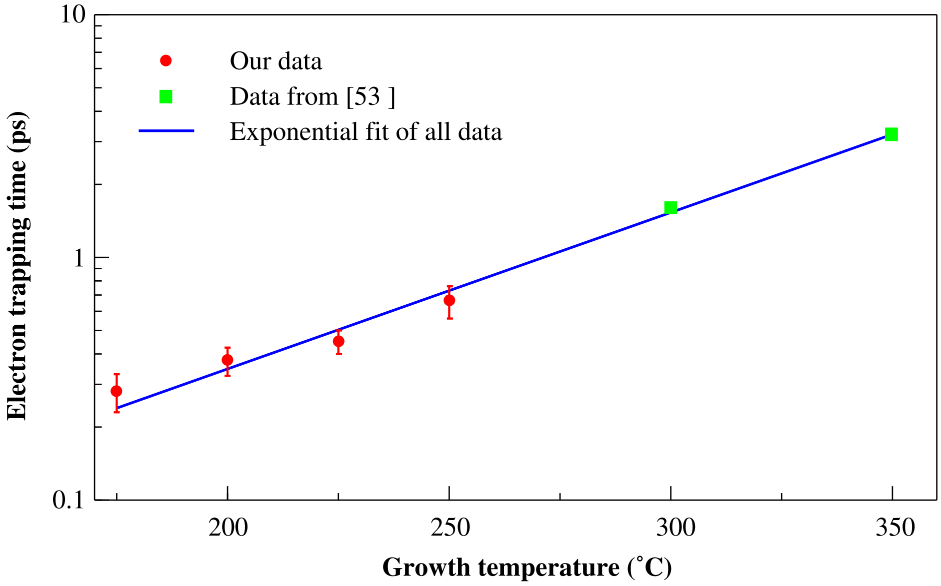

where σ is the capture cross section of the defect, the factor s describes how σ differs from the geometrical area of the defect, R is the average radius of the defect and v_{th} is the electron velocity which is in our case given by its thermal velocity. Within the unified cluster model [101] the amount of the arsenic remains preserved during annealing, i.e. the density of *defects* in as-grown (N_{g}) and annealed sample (N_{A}) are related by

$$N_{\mathrm{g}} R_{\mathrm{g}}^3 = N_{\mathrm{A}} R_{\mathrm{A}}^3, \tag{3.24}$$

where R_{g} and R_{A} are the mean radii of defects in as-grown and annealed samples respectively. In [101] it was shown, that the defect density satisfies relations

$$N_{\mathrm{g}} = N_{\mathrm{g},0} \exp(-T_{\mathrm{g}}/T_{\mathrm{g},0}) \qquad \text{and} \qquad N_{\mathrm{A}} = N_{\mathrm{A},0} \exp(-T_{\mathrm{A}}/T_{\mathrm{A},0}). \tag{3.25}$$

Substitution of Eq. (3.24) and (3.25) to Eq. (3.23) yields

$$\tau_{\mathrm{c}} = \underbrace{\frac{\exp\left(\frac{T_{\mathrm{A}}}{3T_{\mathrm{A},0}}\right)}{\pi R_{\mathrm{g}}^2 v_{\mathrm{th}} s \sqrt[3]{N_{\mathrm{A},0} N_{\mathrm{g},0}^2}}}_{\tau_0} \cdot \exp\left(\frac{2T_{\mathrm{g}}}{3T_{\mathrm{g},0}}\right), \tag{3.26}$$

i.e. the trapping time should grow exponentially with increasing growth temperature. Fit of our data together with those taken from [53] leads to

$\tau_0 \sim 25\,\text{fs}$ and $T_{\text{g},0} = 44\,\text{C}^\circ$. The value of τ_0 is very close to that reported in [101] ($\tau_0 \sim 20\,\text{fs}$). However, the reported coefficient $T_{\text{g},0} = 30°\text{C}$ obtained for the as-grown samples is lower than yields our fit. That's why we conclude, that the annealing slows down the dynamics of LT GaAs grown at higher growth temperatures. This suggests, in turn, that the ability of electron capture is reduced for As clusters comparing to the point defects.

Our results complete the data measured at similar free-carrier densities grown at 300°C and 350°C by means of optical pump – THz probe experiment [53]: out samples were grown at lower temperatures and show faster dynamics.

In conclusion, we have demonstrated the application of THz emission spectroscopy. We have built an experimental setup, in which it is possible to perform a simple and sufficiently precise comparison of the modelled current and measured waveform. Annealed LT GaAs samples grown at different temperatures were investigated by THz this technique, yielding electron lifetimes and mobilities. A simple geometrical model was used to relate these results to the previously published ones.

Figure 3.7: Emitter grown at 175°C.

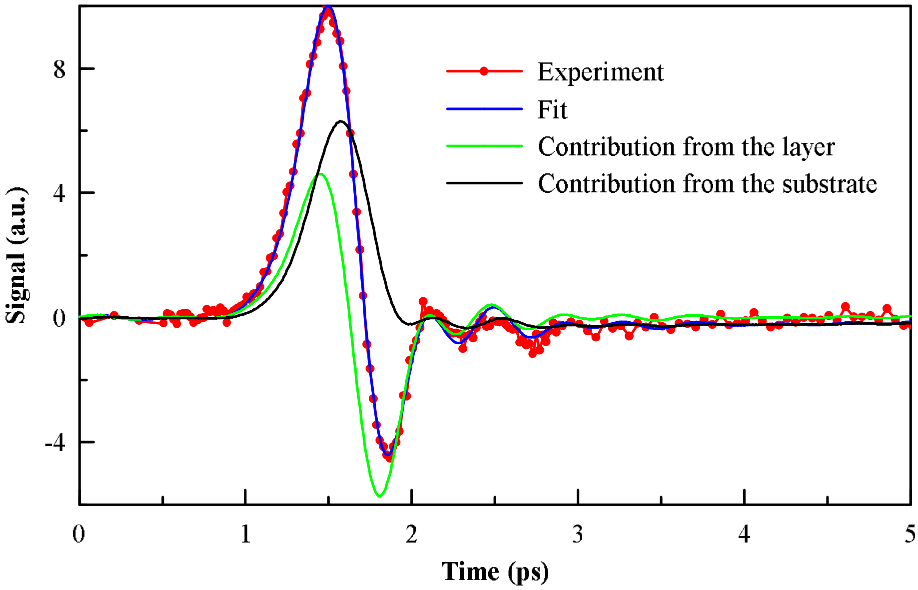

Figure 3.8: Emitter grown at 200°C.

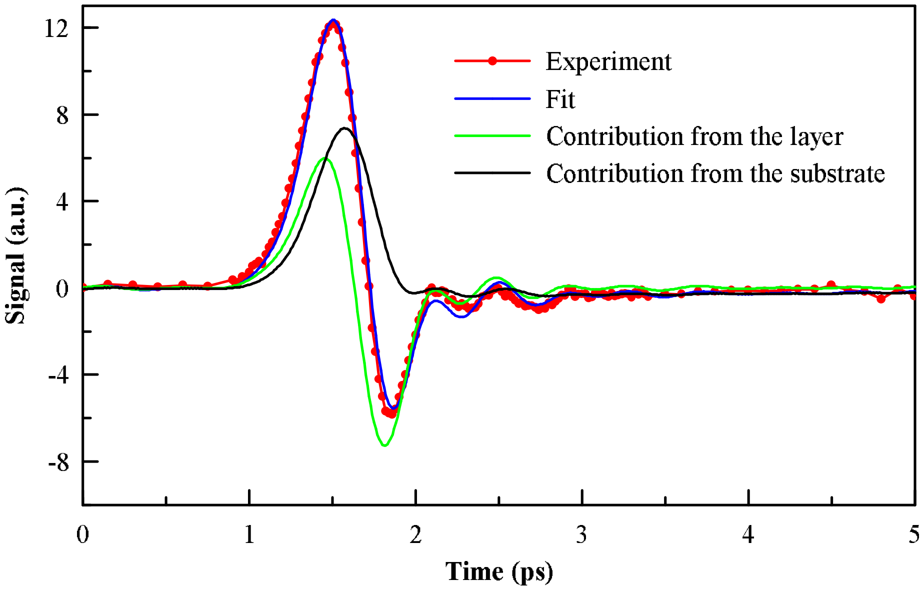

Figure 3.9: Emitter grown at 225°C.

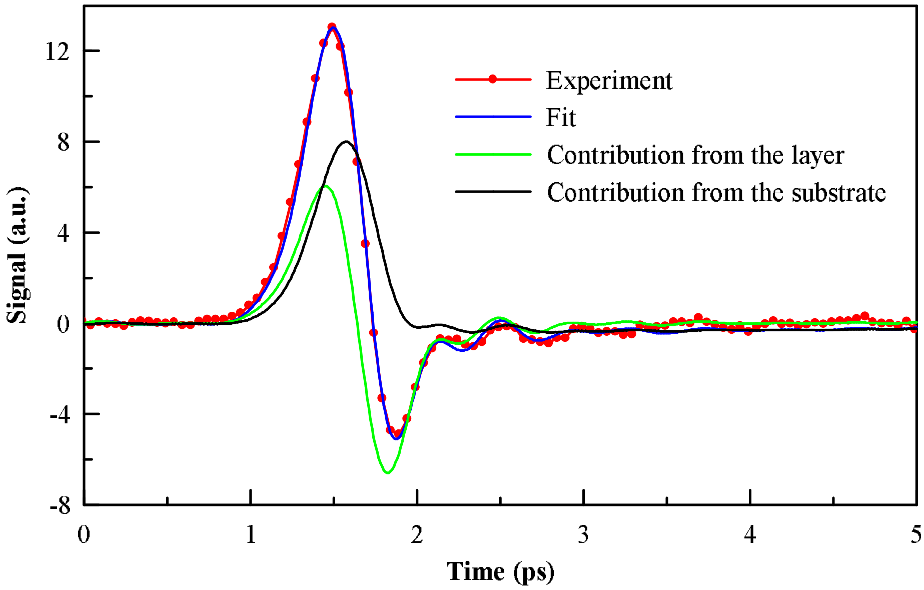

Figure 3.10: Emitter grown at 250°C.

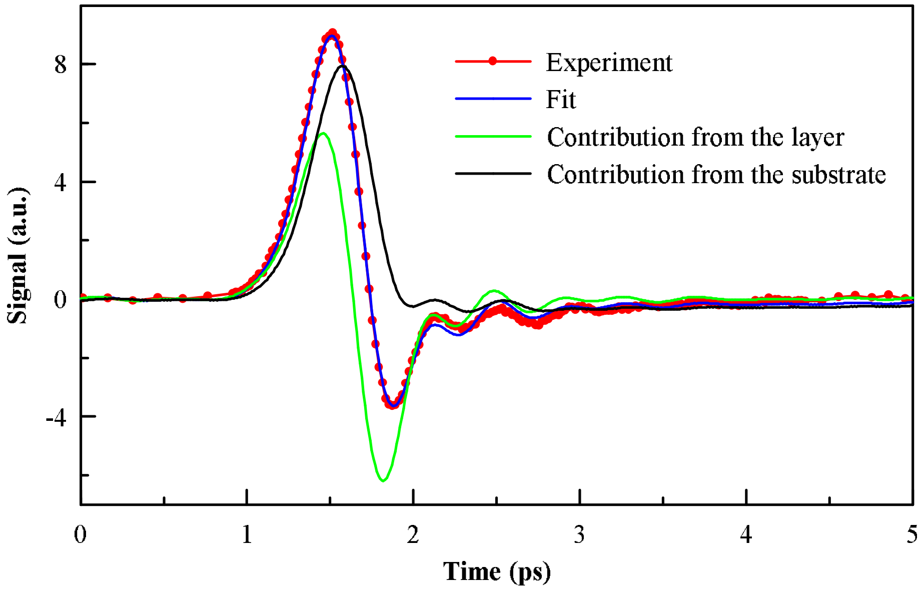

Part 4

Optical pump – THz probe: Perspective method for studying the ultrafast dynamics

Optical pump – THz probe experiments offer a new possibility for investigation of non-stationary processes in condensed matter on the picosecond or subpicosecond time scale. The scheme of the experiment is the following. First, the sample is excited at the time t_e by an ultrashort optical pulse. The induced changes of the properties of the sample are then probed by a pulse of THz radiation, with duration of several picoseconds. Up to now, this kind of experiment was applied to investigations of carrier dynamics in semiconductors [54, 78] and superconductors [71]. The principal interaction here is the absorption of the THz pulse by free carriers. There are also two publications, where the presented technique was applied to the solvation dynamics [72,85]. The THz pulse then probes polar motions due to the optically induced change of the dipole moment of a chromophore.

In order to obtain a complete information about the dynamics, two-dimensional time-scans are required: it is necessary to measure the shape of the THz waveform for different delays between the pump and probe pulse arrival. Up to now, the full two-dimensional scans were performed only in semiconductors [54, 78]. Concerning the solvation dynamics, only particular projection was scanned [72, 85].

These studies provide an access to the dielectric response of the processes initiated by an ultrashort excitation (pump) pulse. It is very convenient to describe their linear THz dielectric response in terms of susceptibility, as it can be quite simply related to the change of the THz pulse transmitted through the sample.

The process under the investigation originates from a coupling between the THz and optical electric field E_{THz} and E_{opt} respectively, i.e. it is a nonlinear process. The corresponding contribution ΔP to the polarization can be described using the third order nonlinear susceptibility $\chi^{(3)}$:

$$\Delta P(t) = \varepsilon_0 \iiint \chi^{(3)}(t', t'', t''') E_{\mathrm{opt}}(t-t''') E_{\mathrm{opt}}(t-t'') E_{\mathrm{THz}}(t-t')\ \mathrm{d}t'\, \mathrm{d}t''\, \mathrm{d}t'''. \tag{4.1}$$

Here and later, the integration is always performed only over the region, where the causality is not violated. We assume that the optical pulse is much shorter than characteristic times of interactions that can be studied using available THz pulses. In this situation, Eq. (4.1) becomes

$$\Delta P(t, t_{\mathrm{e}}) = \varepsilon_0 \int E(t') \Delta\chi(t-t', t-t_{\mathrm{e}})\ \mathrm{d}t', \tag{4.2}$$

where t_{e} is the time of the pump pulse arrival and $\Delta\chi$ is a generalized susceptibility defined as

$$\begin{aligned} \Delta\chi(t', t-t_{\mathrm{e}}) &= I_{\mathrm{opt}} \iint \chi^{(3)}(t', t'', t''') \delta(t-t'''-t_{\mathrm{e}}) \delta(t-t''-t_{\mathrm{e}})\ \mathrm{d}t'' \mathrm{d}t''' = \\ &= I_{\mathrm{opt}} \chi^{(3)}(t', t-t_{\mathrm{e}}, t-t_{\mathrm{e}}). \end{aligned} \tag{4.3}$$

The generalized susceptibility depends on two time variables: the first one is related to the response to the δ-probe-pulse, and the second to the evolution initiated by the pump pulse. If the response of the sample were dominated only by slow processes comparing to the frequency of the probing radiation, a delay-dependent susceptibility could be extracted from the experiment. For example, in usual optical pump – optical probe experiments (time resolved optical transmissivity of reflectivity measurements) a delay-dependent refractive index $N(\omega, \tau)$ — where τ is the pump-probe delay — can be directly measured. In our case, when the rate of the involved processes (picoseconds) becomes comparable with or even faster than the mean probing frequency or the duration of the THz pulse, the time variables related to the THz waveform and to the pump-probe delay mix together in experimentally accessible quantities. A direct application of the Fourier transformation formalism developed for the transmission measurements (section 2.3.1) then often leads to artifacts [71].

For samples in equilibrium, there are two major phenomena affecting the transmitted waveform: refraction on the surfaces of the sample, and dispersive propagation in the sample (bulk effects). Both phenomena also act in samples out of equilibrium. In addition, there are two new important parameters: the extinction length of the pump pulse, and deviation from the velocity-matching between the pump and probe pulse.

Up to now, an attempt of analytical description of the influence of the sample was concentrated only on the generation in the bulk. However, the results deal only with a very idealized situation (nondispersive, lossless sample with perfect velocity matching) [72, 73]. The refraction on the surfaces of the sample is completely neglected. This can be justified only for thick samples, which are sufficiently transparent in both THz and optical region. Nevertheless, the assumptions of this theory are often far from reality.

Recently, an approach based on finite-difference time-domain method has been reported [54, 128]. This method allows to take into account all the mechanisms of how the sample affects the probe-pulse, and can be applied for any strength of the nonequilibrium polarization. On the other hand, it is a numerical method, which was designed to simulate the propagation of the THz probe-pulse in a sample with known susceptibility. This makes the solution of the inverse problem, i.e. the extraction of the nonequilibrium susceptibility extremely complicated. In both cited works, the susceptibility is approximated by a function with a few free parameters, which are to be fitted to the experimental data, i.e. a model of the susceptibility behaviour should be developed prior to the data treatment.

Anyway, in both proposed methods, it is necessary to describe precisely the shape of the waveform irradiating the sample, and its reshaping due to the further propagation and the detector response. There are three dominant effects, which cause a substantial reshaping of the THz waveform: (1) propagation through dispersive media (e.g. water vapour present in the atmosphere [124] or the sample [55,62]), (2) free-space propagation of a spatially limited broadband beam [9], and consequently propagation through any focusing optics [121,129], and (3) the detection process itself [45,125]. In order to obtain valid results, it is necessary to describe all these effects very carefully. This is generally a very peculiar task. The only way to simplify it consists in a design of a suitable experimental setup.

In transmission experiments, all the mentioned effects are cancelled out simply by transformation to the frequency domain (see Eq. (2.15) and the discussion whilch follows). That's why we focused on the possibilities of application of the Fourier transformation in the optical pump – THz probe experiments, too. We show, that when the contribution of nonequilibrium effects is small comparing to the strength of the THz probe field, it is possible to develop an analogous formalism based on a *two-dimensional* Fourier transformation, applied to both time delays involved in two-dimensional scans. This approach takes into account all the mechanisms changing the shape of the waveform during propagation in the sample, and allows to construct an analytical formula for a direct calculation of nonequilibrium susceptibility from the measured two-dimensional temporal scans. Within this approach, the instrumental functions (like the shape of the emitted waveform or the detector response) are partially eliminated.

This part is structured as follows. In section 4.1, we define the times involved in the experiment. We also discuss several possibilities, how to define the relation between the generalized nonequilibrium susceptibility and the nonequilibrium polarization. We transform this relation to the frequency domain in section 4.2. Next, section 4.3 describes the changes of the transmitted THz-probe waveform when the sample is excited by the optical pulse. Then, in section 4.4 we describe the whole propagation of the THz-probe waveform from the emitter to the sensor with an inserted photoexcited sample. Finally we discuss the results and propose the best experimental protocol in section 4.5.

4.1 Definitions of times and nonequilibrium susceptibility

Up to now, we have introduced only two times: the time t_e of the excitation pulse arrival and the time of the measurement (i.e. the time of the sampling pulse arrival) t. However, in the experiment (Fig. 4.1), it is also possible to control the arrival of the THz probe pulse. Till now, it is implicitly taken into account in the form of the probe field E. For clarity, it is convenient to introduce explicitly the probe-pulse arrival t_p, and thus look upon the electric field E as to be function of $(t - t_\mathrm{p})$. Here and later, the function E thus describes only the shape of the THz pulse, not its delay with respect to either pump or sampling pulse. As the probe-pulse profile is not a δ-function,

FIGURE 4.1: Relation of the time delays to the experiment. For example, in order to scan the delays $(t - t_\mathrm{p})$ and $(t - t_\mathrm{e})$ involved in Eq. (4.4) it is necessary to fix the time of the measurement t and scan the times of probe and excitation pulse arrival t_p and t_e.

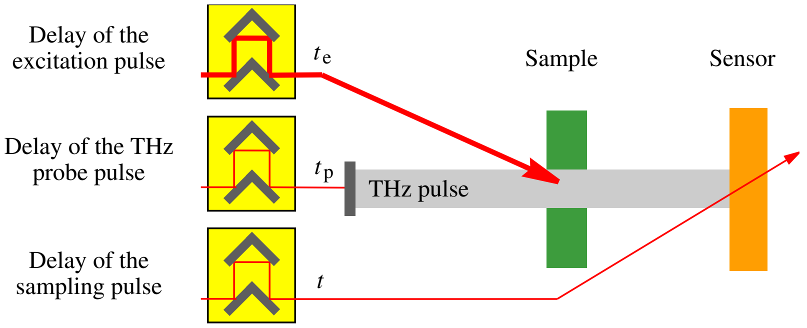

its time of arrival to the sample can be defined more or less arbitrarily. However, if the same position of the related delay line is held for a reference measurement, the arbitrary phases in the Fourier space are cancelled out.

Using this notation, it is simple to demonstrate, that the problem is independent of the choice of the time origin, i.e. that the results are not affected when the pump, probe and sampling pulses are simultaneously delayed. Within the introduced notation, Eq. (4.2) yields

$$\begin{aligned} & \varepsilon_0 \int E(t'-t_\mathrm{p}) \Delta\chi_1(t-t', t-t_\mathrm{e})\ \mathrm{d}t' = \\ = \ & \varepsilon_0 \int E(t') \Delta\chi_1(t-t_\mathrm{p}-t', t-t_\mathrm{e})\ \mathrm{d}t' = \Delta P_1(t-t_\mathrm{p}, t-t_\mathrm{e}). \end{aligned} \tag{4.4}$$

The subscript 1 indicates that the related function is defined in variables $(t-t_\mathrm{p})$ and $(t-t_\mathrm{e})$. The explicit introduction of the time t_p allows us to use the time delays (relative times) rather then absolute times. Such approach automatically reflects the symmetry of the susceptibility with respect to the choice of the time origin. In addition, it has very straightforward relation to the experiment (see Fig. 4.1). Notice, that the time delay $(t-t_\mathrm{p})$ is involved in the equilibrium transmission spectroscopy. We might also choose the time origin for example as the time of the pump pulse arrival (i.e. let t_e equal 0) and thus deal only with the times t and t_p, which correspond to delays $(t-t_\mathrm{e})$ and $(t_\mathrm{p}-t_\mathrm{e})$. This situation can be achieved in the experiment by removing the delay line marked as t_e. However, in order to change the time t_e, one has to move synchronously *two* delay lines controlling the times t and t_p.

Nevertheless, only two delays are independent:

$$t_\mathrm{p} - t_\mathrm{e} = (t - t_\mathrm{e}) - (t - t_\mathrm{p}). \tag{4.5}$$

In Eq. (4.4) the pair of proper variables $(t-t_\mathrm{p})$ and $(t-t_\mathrm{e})$ was chosen. However, another pair, e.g. $(t-t_\mathrm{p})$ and $(t_\mathrm{p}-t_\mathrm{e})$ can be used as well. Writing the polarization in these variables (we mark it by the index 2) yields

$$\Delta P_2(t-t_\mathrm{p}, t_\mathrm{p}-t_\mathrm{e}) = \varepsilon_0 \int E(t') \Delta\chi_1(t-t_\mathrm{p}-t', (t_\mathrm{p}-t_\mathrm{e}+t') + (t-t_\mathrm{p}-t'))\ \mathrm{d}t'. \tag{4.6}$$

For completeness we write also the third possibility where the pair $(t_\mathrm{p}-t_\mathrm{e})$ and $(t-t_\mathrm{e})$ is involved:

$$\Delta P_3(t_\mathrm{p}-t_\mathrm{e}, t-t_\mathrm{e}) = \varepsilon_0 \int E(t') \Delta\chi_1((t-t_\mathrm{e}) - (t_\mathrm{p}-t_\mathrm{e}+t'), t-t_\mathrm{e})\ \mathrm{d}t'. \tag{4.7}$$

The polarizations ΔP_1, ΔP_2 and ΔP_3 have different pairs of delays as proper variables, thus their mathematical form is different. However, they describe the same physical process. Consequently, their values are identical for a given set of times t, t_p and t_e:

$$\Delta P_1(t - t_\mathrm{p}, t - t_\mathrm{e}) = \Delta P_2(t - t_\mathrm{p}, t_\mathrm{p} - t_\mathrm{e}) = \Delta P_3(t_\mathrm{p} - t_\mathrm{e}, t - t_\mathrm{e}). \qquad (4.8)$$

Similarly, it is possible to introduce three representations of the susceptibility according to the proper pair of delays using Eq. (4.5):

$$\Delta\chi_2(t - t_\mathrm{p}, t_\mathrm{p} - t_\mathrm{e}) = \Delta\chi_1(t - t_\mathrm{p}, (t - t_\mathrm{p}) + (t_\mathrm{p} - t_\mathrm{e})) \qquad (4.9)$$

$$\Delta\chi_3(t_\mathrm{p} - t_\mathrm{e}, t - t_\mathrm{e}) = \Delta\chi_1((t - t_\mathrm{e}) - (t_\mathrm{p} - t_\mathrm{e}), t - t_\mathrm{e}). \qquad (4.10)$$

The proper variables of each representation are summarized in Tab. 4.1.

Table 4.1: The proper variables of representations 1, 2 and 3.

Representation	**First delay**	**Second delay**	**First frequency**	**Second frequency**
1	$(t - t_\mathrm{p})$	$(t - t_\mathrm{e})$	ω	ω_e
2	$(t - t_\mathrm{p})$	$(t_\mathrm{p} - t_\mathrm{e})$	ω	ω_p
3	$(t_\mathrm{p} - t_\mathrm{e})$	$(t - t_\mathrm{e})$	ω_p	ω_e

4.2 Fourier transformation

In the preceding section we showed, that there are three possible representations of the susceptibility and polarization. The relation between the representations is very simple in the time domain. However, we will need this relation in the Fourier space.

Let us denote the frequencies conjugated to delays $(t - t_\mathrm{p})$, $(t - t_\mathrm{e})$ and $(t_\mathrm{p} - t_\mathrm{e})$ as ω, ω_e and ω_p respectively (Tab. 4.1). We define the Fourier transform G_1 of an arbitrary function g_1 in the delays $(t - t_\mathrm{p})$ and $(t - t_\mathrm{e})$ as

$$G_1(\omega, \omega_\mathrm{e}) = \iint \mathrm{e}^{-\mathrm{i}\omega(t-t_\mathrm{p}) - \mathrm{i}\omega_\mathrm{e}(t-t_\mathrm{e})} g_1(t - t_\mathrm{p}, t - t_\mathrm{e})\ \mathrm{d}(t - t_\mathrm{p})\ \mathrm{d}(t - t_\mathrm{e}). \quad (4.11)$$

The definition for the remaining two pairs of delays is similar. Note, that within this definition, the imaginary part of the permittivity and of the refractive index is negative for media with losses. This convention thus differs from that used in parts 2 and 3 of this work.

We have selected the proper variables of the function g_1 as $(t - t_\mathrm{p})$ and $(t - t_\mathrm{e})$ and applied the Fourier transformation to these variables. However, we can keep the representation 1 of the function g, and apply the Fourier transformation also in a different pair of delays: using the identity (4.5) we find

$$\begin{gathered}
G_1(\omega, \omega_\mathrm{e}) = \int g_1(t - t_\mathrm{p}, t - t_\mathrm{e}) \mathrm{e}^{-\mathrm{i}\omega(t-t_\mathrm{p})-\mathrm{i}\omega_\mathrm{e}(t-t_\mathrm{e})} \mathrm{d}(t - t_\mathrm{p}) \mathrm{d}(t - t_\mathrm{e}) = \\
= \int g_1(t-t_\mathrm{p}, (t-t_\mathrm{p})+(t_\mathrm{p}-t_\mathrm{e})) \mathrm{e}^{-\mathrm{i}\omega(t-t_\mathrm{p})-\mathrm{i}\omega_\mathrm{e}((t-t_\mathrm{p})+(t_\mathrm{p}-t_\mathrm{e}))} \mathrm{d}(t-t_\mathrm{p}) \mathrm{d}(t_\mathrm{p}-t_\mathrm{e}) = \\
= G_2(\omega + \omega_\mathrm{e}, \omega_\mathrm{e}),
\end{gathered} \tag{4.12}$$

which is the desired relation between the representation 1 and 2 in the Fourier space. Similarly, the relation between G_1 and G_3 can be derived. According to the choice of the proper variables in the Fourier space, the results can be summarized as follows:

$$\begin{array}{rcccl}
G_1(\omega, \omega_\mathrm{e}) & = & G_2(\omega + \omega_\mathrm{e}, \omega_\mathrm{e}) & = & G_3(-\omega, \omega + \omega_\mathrm{e}) \\
G_1(\omega - \omega_\mathrm{p}, \omega_\mathrm{p}) & = & G_2(\omega, \omega_\mathrm{p}) & = & G_3(\omega_\mathrm{p} - \omega, \omega) \\
G_1(-\omega_\mathrm{p}, \omega_\mathrm{e} + \omega_\mathrm{p}) & = & G_2(\omega_\mathrm{e}, \omega_\mathrm{p} + \omega_\mathrm{e}) & = & G_3(\omega_\mathrm{p}, \omega_\mathrm{e}).
\end{array} \tag{4.13}$$

This allows us to work in a single representation, and then to transform important results into any representation using the relations above.

4.3 Influence of the sample

As it was pointed out in the introduction to this part, there is a number of effects affecting the shape of the waveform which passes through the sample. In order to describe them all, we start directly from Maxwell's equations

$$\mathrm{rot}\, \boldsymbol{E} = -\frac{\partial \boldsymbol{B}}{\partial t} \qquad \mathrm{rot}\, \boldsymbol{H} = \frac{\partial \boldsymbol{D}}{\partial t} \tag{4.14}$$

$$\mathrm{div}\, \boldsymbol{D} = 0 \qquad \mathrm{div}\, \boldsymbol{B} = 0, \tag{4.15}$$

where $\boldsymbol{E}$ and $\boldsymbol{H}$ is the electric and magnetic intensity and $\boldsymbol{D}$ and $\boldsymbol{B}$ is the electric and magnetic induction, respectively. We assume the sample to be homogenous, with an equilibrium relative permittivity $\varepsilon(t)$ (in the time domain) or the related complex refractive index N. The permeability is assumed to be the vacuum one μ_0, thus $\boldsymbol{B} = \mu_0 \boldsymbol{H}$. In order to satisfy the Maxwell's *div* equations (Eq. (4.15)), we suppose the electromagnetic transients to be plane waves, which propagate in the z-direction and which are linearly polarized along the x-direction (see Fig. 4.2). Now, we add a small nonequilibrium polarization ΔP parallel to the x-axis caused by the

FIGURE 4.2: Orientation of the axes, electric and magnetic field.

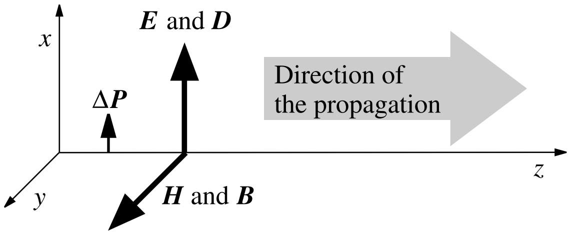

optical excitation pulse. We assume, that this polarization varies only along the coordinate z. In this situation, the Maxwell's *rot* equations (4.14) put together yield an equation for the total electric field E:

$$\frac{\partial^2 E}{\partial z^2} = \frac{1}{c^2}\frac{\partial^2(\varepsilon(t) * E)}{\partial t^2} + \frac{1}{\varepsilon_0 c^2}\frac{\partial^2 \Delta P}{\partial t^2}. \tag{4.16}$$

The asterisk denotes a convolution acting to the time variable t. We decompose the electric field E to the value E_0 present in the equilibrium and a nonequilibrium (secondary) contribution ΔE:

$$E = E_0 + \Delta E. \tag{4.17}$$

At this point, we use the most important assumption of our theory: $\Delta E \ll E_0$, i.e. the additional field due to the nonequilibrium susceptibility should be very small comparing to the field present when the sample is in equilibrium. This allows us to write a similar wave equation for ΔE

$$\frac{\partial^2 \Delta E}{\partial z^2} = \frac{1}{c^2}\frac{\partial^2(\varepsilon * \Delta E)}{\partial t^2} + \frac{1}{\varepsilon_0 c^2}\frac{\partial^2 \Delta P}{\partial t^2}. \tag{4.18}$$

Unlike Eq. (4.16), this equation is already linear, because the nonequilibrium polarization ΔP can be written within this approximation using the equilibrium field E_0 instead of the total electric intensity $E = E_0 + \Delta E$:

$$\Delta P = \varepsilon_0 \int \Delta\chi(t - t', t - (t_{\mathrm{e}} + z/v_{\mathrm{g}})) \exp(-\alpha z) E_0(t', z) \, \mathrm{d}t'. \tag{4.19}$$

Here, α is the extinction coefficient of the excitation pulse and v_{g} is its (group) velocity of propagation.

It is clear, that both the electric and magnetic field is additionally parameterized by the time of the excitation pulse arrival t_{e}. By selecting $t_{\mathrm{p}} = 0$, we can treat the times t and t_e as delays $(t - t_\mathrm{p})$ and $-(t_\mathrm{p} - t_\mathrm{e})$ instead. Eq. (4.18) is usually solved by Fourier transformation applied to the time variable t. However, such attempt fails, as there remains an integral relation in Eq. (4.19). Instead, an application of the two-dimensional Fourier transformation in the two delays $(t - t_\mathrm{p})$ and $(t_\mathrm{p} - t_\mathrm{e})$ solves the problem (see section 4.2 for the definition). Eq. (4.18) is transformed to an ordinary linear differential equation of the second order with constant coefficients and a nonvanishing right-hand side:

$$\frac{\mathrm{d}^2\Delta E}{\mathrm{d}z^2}+\frac{\omega^2}{c^2}N^2(\omega)\Delta E = -\frac{\omega^2}{c^2}E_0(\omega-\omega_\mathrm{p}, z)\mathrm{e}^{-\alpha z+\mathrm{i}\omega_\mathrm{p}/v_\mathrm{g}}\Delta\chi_1(\omega-\omega_\mathrm{p}, \omega_\mathrm{p}). \quad (4.20)$$

Exactly, one should take into account all the internal reflections in the sample (section 4.3.3). However, it is often possible to proceed the temporal windowing. We thus deal only with the direct pass beam, i.e. we cut the pulses coming from internal reflections in the sample. This allows to treat each face of the sample as an interface between two half-spaces (sections 4.3.1 and 4.3.2). This approximation can be well justified for thick samples, where the temporal windowing is possible. Application of the temporal windowing to the primary beam E_0 allows to write its evolution as

$$E_0(\omega - \omega_\mathrm{p}, z) = e_0\mathrm{e}^{-\mathrm{i}(\omega-\omega_\mathrm{p})N(\omega-\omega_\mathrm{p})z/c}, \quad (4.21)$$

where $e_0 = E_0(\omega - \omega_\mathrm{p}, z = 0+)$ is the THz wave which has just been transmitted trough the input interface (surrounding environment/sample) using equilibrium Fresnel equations. Due to the exponential form of this expression, we can write the general solution of Eq. (4.20) as

$$\Delta E = \gamma\mathrm{e}^{\mathrm{i}kz} + \delta\mathrm{e}^{-\mathrm{i}kz} - \frac{A\mathrm{e}^{-\mathrm{i}Kz}}{N^2 - K^2/k_0^2}, \quad (4.22)$$

where γ and δ are constants which will be determined from the boundary conditions,

$$\begin{aligned} k_0 &= \frac{\omega}{c}, && (4.23)\\ k &= \frac{\omega N(\omega)}{c} = k_0 N, && (4.24)\\ K &= \frac{(\omega-\omega_\mathrm{p})N(\omega-\omega_\mathrm{p})}{c} + \frac{\omega_\mathrm{p}}{v_\mathrm{g}} - \mathrm{i}\alpha, && (4.25)\\ \text{and} \quad A &= e_0\Delta\chi_1(\omega-\omega_\mathrm{p}, \omega_\mathrm{p}). && (4.26) \end{aligned}$$

The nonequilibrium contribution ΔH to the magnetic intensity can be found by Fourier transformation of the second equation in (4.14) and substitution for ΔE:

$$\mu_0 \omega \Delta H = \mathrm{i} \cdot \frac{\mathrm{d}\Delta E}{\mathrm{d}z} = -k\gamma \mathrm{e}^{\mathrm{i}kz} + k\delta \mathrm{e}^{-\mathrm{i}kz} - \frac{AK\mathrm{e}^{-\mathrm{i}Kz}}{N^2 - K^2/k_0^2}. \tag{4.27}$$

4.3.1 Input face of the sample

The first boundary condition is related to the coupling of the fields at the interface. The tangential components of both the electric and magnetic intensity should be continuous, thus

$$E_{\mathrm{in}} + E_{\mathrm{R}} = E_{\mathrm{T}} \quad \text{and} \quad H_{\mathrm{in}} + H_{\mathrm{R}} = H_{\mathrm{T}}. \tag{4.28}$$

Indices *in*, R and T refer to the pulses incident, reflected and transmitted through the interface (see Fig. 4.3). For clarity, we treat the condition for the electric intensity in more detail. We decompose it to the equilibrium and nonequilibrium contribution, i.e.

FIGURE 4.3: Description of the sample out of equilibrium.

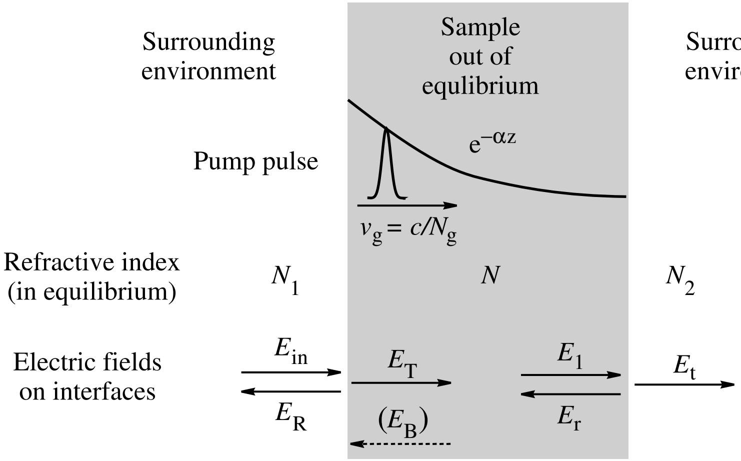

$$E_{\mathrm{in},0} + E_{\mathrm{R},0} + \Delta E_{\mathrm{R}} = E_{\mathrm{T},0} + \Delta E_{\mathrm{T}}. \tag{4.29}$$

In equilibrium, the continuity condition is satisfied, thus this relation is reduced to $\Delta E_{\mathrm{R}} = \Delta E_{\mathrm{T}}$. Similarly, the condition for continuity of the magnetic intensity yields $\Delta H_{\mathrm{R}} = \Delta H_{\mathrm{T}}$. As the surrounding environment is in equilibrium, the magnetic and electric components of the reflected field are connected via expression

$$\Delta H_{\mathrm{R}} = -\frac{N_1}{\mu_0 c}\Delta E_{\mathrm{R}}, \tag{4.30}$$

thus the first boundary condition is simplified to

$$\frac{N_1}{\mu_0 c}\Delta E_{\mathrm{T}} + \Delta H_{\mathrm{T}} = 0, \tag{4.31}$$

where $\Delta E_{\mathrm{T}} = \Delta E(z=0)$ and $\Delta H_{\mathrm{T}} = \Delta H(z=0)$. As ΔE_{T} is related to the wave propagating in the forward direction only, $\Delta E(z)$ should vanish as $z \to \infty$ — this is the second boundary condition. It immediately yields $\gamma = 0$, as the imaginary part of the refractive index N is negative. The condition (4.31) then gives δ — its substitution back to Eq. (4.22) yields

$$\begin{aligned} \Delta E &= -A\mathrm{e}^{-\mathrm{i}kz}\left[\frac{\mathrm{e}^{-\mathrm{i}(K-k)z}-1}{N^2-K^2/k_0^2} + \frac{1}{(N+N_1)(N+K/k_0)}\right] & (4.32)\\ \mu_0\omega\Delta H &= -A\mathrm{e}^{-\mathrm{i}kz}\left[K\frac{\mathrm{e}^{-\mathrm{i}(K-k)z}-1}{N^2-K^2/k_0^2} + \frac{k_0 N_1}{(N+N_1)(N+K/k_0)}\right] & (4.33)\end{aligned}$$

It is interesting to study the electric field in the phase-matched case for nondispersive lossless samples. The phase-matching condition can be defined as $K \to k$ (i.e. the pump pulse propagates with the same velocity as does the probe pulse, see Eq. (4.25)). Thus

$$\frac{\Delta E(z)}{E_0(\omega-\omega_{\mathrm{p}},0+)} = \mathrm{e}^{-\mathrm{i}kz}\left[-\frac{1}{2N(N+N_1)} - \frac{\mathrm{i}\omega\cdot z}{2Nc}\right]\cdot\Delta\chi(\omega-\omega_{\mathrm{p}},\omega_{\mathrm{p}}). \tag{4.34}$$

We can identify the first term with the nonequilibrium contribution to the Fresnel transmission coefficient. The second term describes the secondary radiation generated during the propagation in the medium. This term was calculated recently [72] within the phase-matching limit — in the time domain, the electric field of the secondary radiation is proportional to the time derivative of the nonequilibrium polarization ΔP.

In sufficiently thick and optically transparent samples, the second term is clearly the leading one. However, the importance of the first term grows in the opposite case, or when the deviation from the phase-matching condition becomes significant. This term thus dominates e.g. for semiconductors excited above the band gap.

4.3.2 Output face of the sample

The second interface can be treated similarly as the first one. The continuity of tangential components of both the electric and magnetic intensity leads to a similar condition for nonequilibrium contributions, i.e.

$$\Delta E_1 + \Delta E_{\mathrm{r}} = \Delta E_{\mathrm{t}} \quad \text{and} \quad \Delta H_1 + \Delta H_{\mathrm{r}} = \Delta H_{\mathrm{t}}. \tag{4.35}$$

Indices *1*, *r* and *t* denote the pulses incident, reflected and transmitted through the interface (see Fig. 4.3). We neglect the reflection of the optical pump beam, as for the majority of cases of interest its intensity is very small. We also neglect the secondary radiation generated by the reflected probe pulse. This last approximation is expected to work well, as (1) the phase-matching condition can never be achieved as the optical pulse and the reflected THz wave are counter-propagating, and (2) the backward propagating THz pulse comes to the detector delayed by an additional time $2NL/c$. In this situation, the incident fields are given by Eq. (4.32) and (4.33) with $z = L$ and the reflected field corresponds to the term $\gamma \mathrm{e}^{+\mathrm{i}kz}$ in Eq. (4.22), which does not vanish now. The transmitted pulse propagates in an equilibrium environment, thus its electric and magnetic intensity are related by

$$\Delta H_{\mathrm{t}} = +\frac{N_2}{\mu_0 c}\Delta E_{\mathrm{t}}. \tag{4.36}$$

Elimination of γ yields the formula for the nonequilibrium contribution to the electric intensity transmitted through the sample and both its surfaces:

$$\Delta E_{\mathrm{t}} = \frac{A\mathrm{e}^{-\mathrm{i}kL}}{N+N_2}\left[\frac{1-\mathrm{e}^{-\mathrm{i}(K-k)L}}{N-K/k_0} - \frac{2N}{(N+N_1)(N+K/k_0)} + \frac{1}{N+K/k_0}\right] \tag{4.37}$$

The first term is the bulk contribution which strongly depends on the phase-matching condition. The second term corresponds to the first term in the expression Eq. (4.32) having passed through the output interface without photo-exciting perturbation, it is thus clearly generated at the first interface. Finally, the third term has no equivalent in Eq. (4.32) and it can be identified with a contribution coming from the second interface.

It is convenient to summarize Eq. (4.37) using the product

$$\Delta E_{\mathrm{t}}(\omega, \omega_{\mathrm{p}}) = E_0(\omega) \cdot Q(\omega, \omega_{\mathrm{p}}) \cdot \Delta\chi_1(\omega - \omega_{\mathrm{p}}, \omega_{\mathrm{p}}), \tag{4.38}$$

where the filter function Q is defined as

$$Q(\omega, \omega_{\mathrm{p}}) = \frac{\mathrm{e}^{-\mathrm{i}kL}}{N+N_2}\left[\frac{1-\mathrm{e}^{-\mathrm{i}(K-k)L}}{N-K/k_0} - \frac{2N}{(N+N_1)(N+K/k_0)} + \frac{1}{N+K/k_0}\right]. \tag{4.39}$$

Obviously, it depends only on equilibrium properties of the sample and surrounding environments.

In Fig. 4.4 we plot the generated amplitude of the wave ΔE_{t} as a function of the length of the sample for different absorption coefficients α and pulse walk-off

$$\Delta w = \frac{N}{c} - \frac{1}{v_{\mathrm{g}}} \tag{4.40}$$

which describes how closely the phase-matching condition is satisfied. As the magnitude of the nonlinear susceptibility can be expected to be proportional to the absorbed power, Fig. 4.4 in fact shows the product $\alpha|Q|$.

These figures correspond to experimental situations that can be encountered in the study of solvation dynamics: for a given solvent (characterized by Δw) one looks for a suitable length of the cuvette and concentration of the chromophore, which linearly scales α. In this case, typically $N_1 \approx N$, thus the second and third term in Eq. (4.37) practically compensate each other and the bulk (phase-matched) contribution becomes the leading one — the amplitude practically vanishes for $L = 0$ (see Fig. 4.4).

On the contrary, in semiconductors only the first term of Eq. (4.37) contributes to the signal, as the pump beam is usually absorbed within few microns near the input face. This is illustrated in Fig. 4.5, where the signal amplitude $\alpha|Q|$ is plotted versus the absorption coefficient. The situation encountered in solutions corresponds to the initial increase of the signal amplitude where the bulk term is dominant and the surface term compensate each other. The semiconductors or other highly absorbing materials are represented by the second increase of the signal amplitude which is independent of the sample thickness and where the terms coming from the first surface becomes dominant while the sum of the remaining terms vanish.

4.3.3 Thin sample

Up to now, we have taken into account only the direct primary pulse, and the forward propagating secondary radiation. However, both can reflect on each interface. Thus also the backward propagating wave irradiating the first interface (dashed arrow in Fig. 4.3) is taken into consideration. This situation is important for thin samples, where the pulses coming from different reflections cannot be resolved in time.

We start the description using Eq. (4.20). In this expression, we only need to modify the expression for the primary field E_0, in order to account for multiple internal reflections:

$$E_0(\omega - \omega_{\mathrm{p}}, z) = e_0 \left(F \mathrm{e}^{-\mathrm{i}\tilde{k}z} + B \mathrm{e}^{+\mathrm{i}\tilde{k}z} \right), \tag{4.41}$$

FIGURE 4.4: Amplitude of the secondary wave ΔE_t represented by the quantity $\alpha|Q|$ (see text) as a function of the sample length L for different optical absorption coefficients α and different walk-offs Δw. Parameters: $\omega/\omega_p = 2$, $N = 1.5$ and $N_1 = N_2 = 2$. The curves which are shown were calculated at 1 THz, but as Q scales practically linearly with frequency under these conditions, the same curves are obtained for other frequencies.

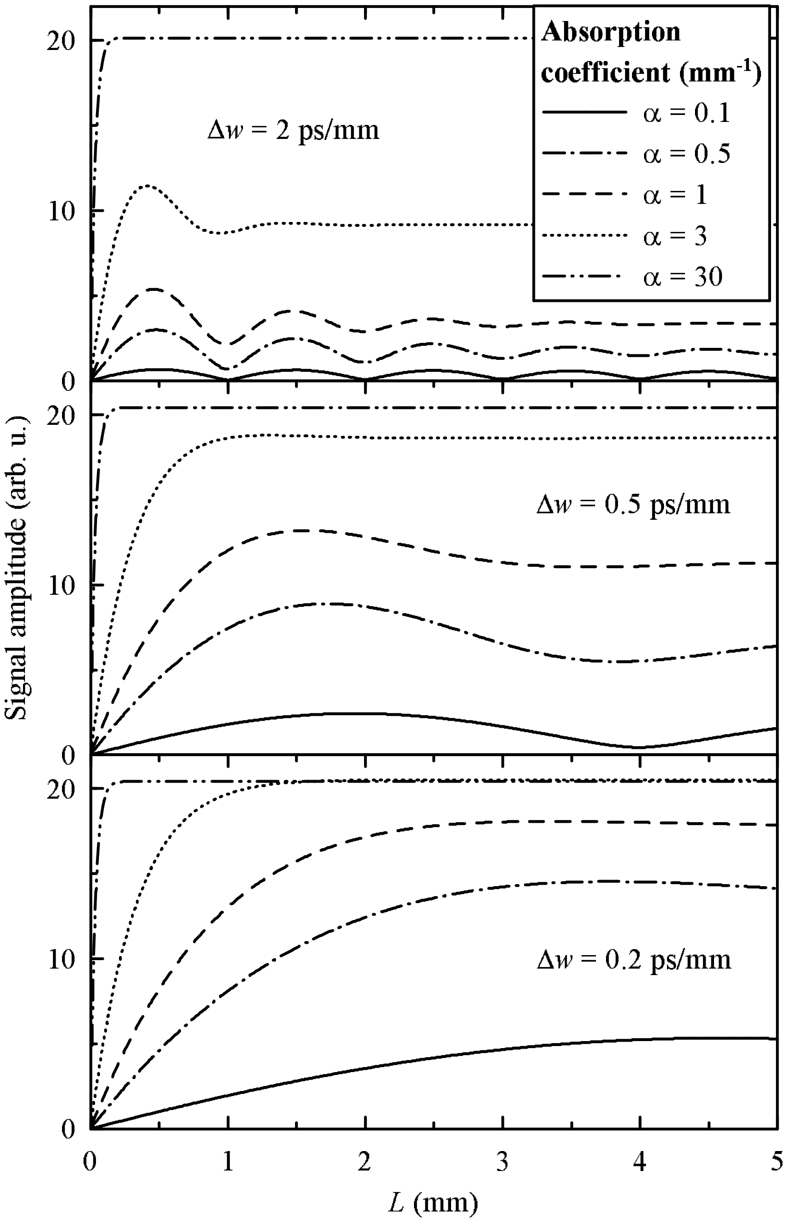

FIGURE 4.5: (a) Amplitude of the secondary wave ΔE_{t} at 1 THz (represented by the quantity $\alpha|Q|$) versus optical absorption coefficient α. (b) Decomposition into contributions given by the 3 terms of Eq. (4.37) and discussed in the text. Parameters: $\omega/\omega_{\mathrm{p}} = 2$, $N = 3.5$, $N_1 = N_2 = 1$ and $\Delta w = 0.2\,\mathrm{ps/mm}$.

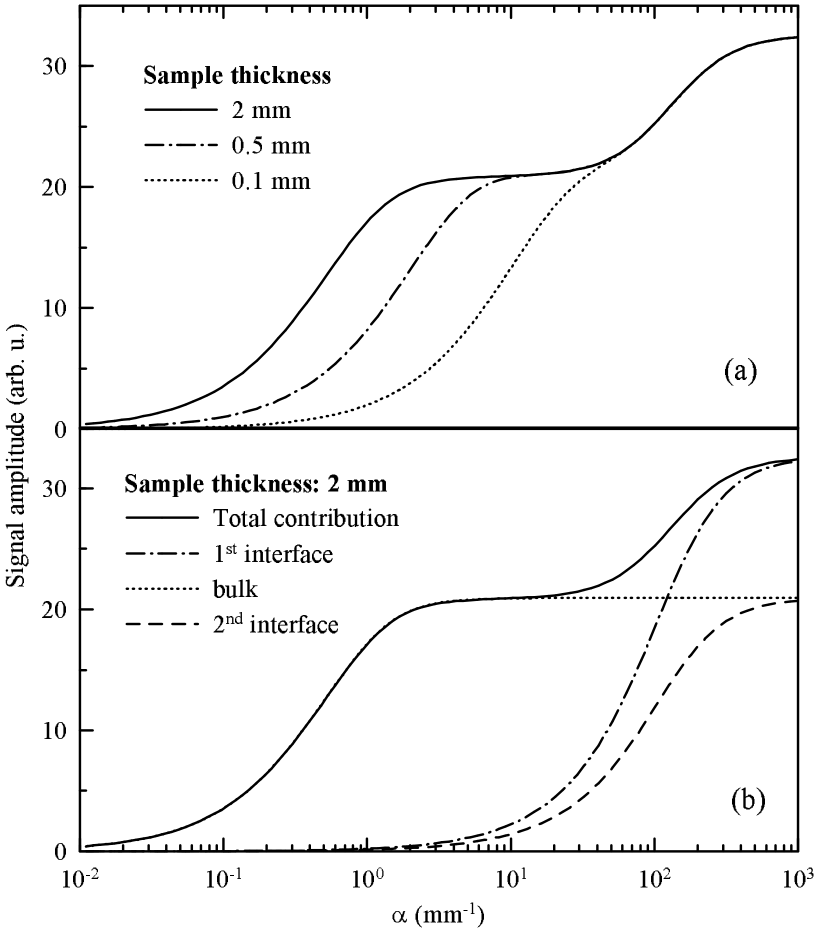

$$\begin{aligned}
\text{where}\qquad \tilde{k} &= (\omega-\omega_{\mathrm{p}})N(\omega-\omega_{\mathrm{p}})/c && (4.42)\\
F &= \sum_{j=0}^{\infty}(r_1r_2)^j \mathrm{e}^{-2\mathrm{i}j\tilde{k}L}, && (4.43)\\
B &= r_2\mathrm{e}^{-2\mathrm{i}\tilde{k}L}\sum_{j=0}^{\infty}(r_1r_2)^j \mathrm{e}^{-2\mathrm{i}j\tilde{k}L} && (4.44)\\
\text{and}\qquad r_m &= \frac{N(\omega-\omega_{\mathrm{p}})-N_m(\omega-\omega_{\mathrm{p}})}{N(\omega-\omega_{\mathrm{p}})+N_m(\omega-\omega_{\mathrm{p}})},\quad m=1,2. && (4.45)
\end{aligned}$$

Consequently, the general solution of Eq. (4.20) can be written as

$$\Delta E = \gamma \mathrm{e}^{\mathrm{i}kz} + \delta \mathrm{e}^{-\mathrm{i}kz} - \frac{k_0^2 A F \mathrm{e}^{-\mathrm{i}Kz}}{k^2 - K^2} - \frac{k_0^2 A B \mathrm{e}^{-\mathrm{i}K_\mathrm{B} z}}{k^2 - K_\mathrm{B}^2}, \tag{4.46}$$

where parameters γ and δ are determined by boundary conditions, K is given by Eq. (4.25) and

$$K_\mathrm{B} = -\frac{(\omega - \omega_\mathrm{p}) N(\omega - \omega_\mathrm{p})}{c} + \frac{\omega_\mathrm{p}}{v_\mathrm{g}} - \mathrm{i}\alpha. \tag{4.47}$$

Both the forward and backward propagating waves are incorporated in Eq. (4.46) — their separation is not necessary. This allows to write the conditions for the continuity of the electric and magnetic field simply as

$$\begin{aligned}
\Delta E(z=0) &= \Delta E_\mathrm{R} && (4.48)\\
\mu_0 \omega \Delta H(z=0) &= \mu_0 \omega \Delta H_\mathrm{R} = -k_0 N_1 \Delta E_\mathrm{R} && (4.49)\\
\Delta E(z=L) &= \Delta E_\mathrm{t} && (4.50)\\
\mu_0 \omega \Delta H(z=L) &= \mu_0 \omega \Delta H_\mathrm{t} = +k_0 N_2 \Delta E_\mathrm{t}. && (4.51)
\end{aligned}$$

Elimination of γ and δ yields the desired expression for the filter function Q_∞:

$$\begin{aligned}
&Q_\infty(\omega, \omega_\mathrm{p}) =\\
&= \frac{F \mathrm{e}^{-\mathrm{i}kL}}{(N_2 + N)\left[1 - \tilde{r}_1 \tilde{r}_2 \mathrm{e}^{-2\mathrm{i}kL}\right]} \left[\left(1 - \frac{2N}{N_1 + N}\right) \frac{1 - \mathrm{e}^{-\mathrm{i}(K+k)L}}{N + K/k_0} + \frac{1 - \mathrm{e}^{-\mathrm{i}(K-k)L}}{N - K/k_0}\right] +\\
&+ \frac{B \mathrm{e}^{-\mathrm{i}kL}}{(N_2 + N)\left[1 - \tilde{r}_1 \tilde{r}_2 \mathrm{e}^{-2\mathrm{i}kL}\right]} \left[\left(1 - \frac{2N}{N_1 + N}\right) \frac{1 - \mathrm{e}^{-\mathrm{i}(K_\mathrm{B}+k)L}}{N + K_\mathrm{B}/k_0} + \frac{1 - \mathrm{e}^{-\mathrm{i}(K_\mathrm{B}-k)L}}{N - K_\mathrm{B}/k_0}\right]
\end{aligned} \tag{4.52}$$

The reflection coefficients $\tilde{r}_1$ and $\tilde{r}_2$ are defined by Eq. (4.45) with the frequency ω instead of $\omega - \omega_\mathrm{p}$. The internal reflections of the primary waves are encoded into the coefficients F and B. The internal reflections of the generated secondary pulses are expressed by the term in the square bracket via the identity

$$\frac{1}{1 - \tilde{r}_1 \tilde{r}_2 \mathrm{e}^{-2\mathrm{i}kL}} = \sum_{m=0}^{\infty} (\tilde{r}_1 \tilde{r}_2)^m \mathrm{e}^{-2\mathrm{i}mkL}. \tag{4.53}$$

The exponential term containing the sum $K + k$ or $K_\mathrm{r} + k$ can never become phase-matched for the forward or backward wave respectively: this exponential describes thus only a higher order term from the point of view of the temporal windowing. One can simply check, that the first order terms lead to Eq. (4.39). The lowest-order terms coming from the backward propagation read

$$\frac{r_2 \mathrm{e}^{-\mathrm{i}kL-2\mathrm{i}(\omega-\omega_\mathrm{p})N(\omega-\omega_\mathrm{p})L/c}}{N_2+N}\left[\left(1-\frac{2N}{N_1+N}\right)\frac{1}{N+K_\mathrm{B}/k_0}+\frac{1-\mathrm{e}^{-\mathrm{i}(K_\mathrm{B}-k)L}}{N-K_\mathrm{B}/k_0}\right] \quad (4.54)$$

In principle, these terms are delayed in time with respect to those of Eq. (4.39) as the propagator is roughly equal to $-3\mathrm{i}kL$. This justifies for the majority of cases the omission of the reflected primary wave. The second term in the square bracket in Eq. (4.54) can become resonant only in the hypothetical case when the phase-matching condition ($\Delta w = 0$) is satisfied, and the primary field has a static component ($\omega = \omega_\mathrm{p}$). On the other hand, if we are far from the phase-matching condition, the generated signal owing to this term will be small. At the same time the non-vanishing positive argument of the exponential term $\exp(-\mathrm{i}(K_\mathrm{B} - k)L)$ will decrease the effective time delay of this contribution. The interpretation of this contribution is the following: out of the phase matching the back-propagating primary wave generates in the bulk a small part of the secondary wave with an opposite propagation direction (i.e. this secondary wave propagates directly forward after the generation). This secondary wave then comes into the detector at intermediate times (with delay between NL/c and $3NL/c$), thus the temporal windowing procedure cannot be strictly defined. Consequently, a small systematic error is introduced into the treated data if the expression (4.39) and the time-windowing are applied in this case.

4.4 Propagation of the terahertz beam

In the preceding section, we derived the relation between the incoming pulse E_0 and the waveform ΔE_t transmitted through the sample. However, the emitted pulse E_E undergoes a substantial reshaping before it reaches the sample, and also the detected pulse differs from the shape of the transmitted pulse ΔE_t at least due to the detector response (follow Fig. 4.6). Both these effects are taken into account in this section.

First, the generated field E_E reshapes to the field E_0 just after the input face of the sample. The effects of the free space propagation of spatially limited beams, focusing optics, propagation through dispersive media and other can be accounted for by a response function $\mathcal{P}_1$. The field E_0 can be thus described by

$$E_0(t-t_\mathrm{p}) = E_\mathrm{E}(t-t_\mathrm{p}) \underset{t}{*} \mathcal{P}_1(t), \quad (4.55)$$

FIGURE 4.6: Block scheme of the optical pump – THz probe experiment: notation of THz waveforms, times and instrumental functions.

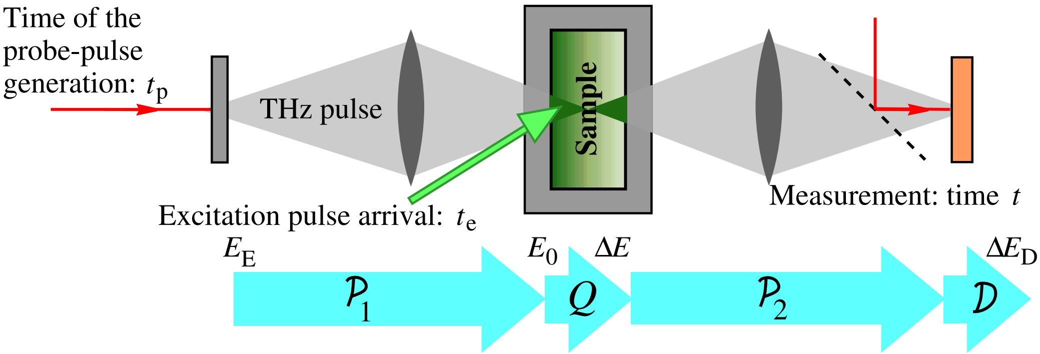

where the asterisk ($*$) denotes the convolution operation which acts on the variable written beyond this symbol. Second, we have shown in section 4.3, that the influence of the sample is given by Eq. (4.37), i.e.

$$\Delta E_\mathrm{t}(\omega,\omega_\mathrm{p}) = Q(\omega,\omega_\mathrm{p})\Delta\chi_1(\omega-\omega_\mathrm{p},\omega_\mathrm{p})E_0(\omega). \tag{4.56}$$

During the propagation between the sample and the sensor, the waveform ΔE_t exhibits also a reshaping. The effects are analogous to those before the sample, and we describe them by a response function $\mathcal{P}_2$. Finally, the response of the sensor $\mathcal{D}$ is at the origin of the difference between the waveform incident on the sensor and the measured one. The measured waveform can be thus described as

$$\Delta E_\mathrm{D}(t-t_\mathrm{p},t_\mathrm{p}-t_\mathrm{e}) = \Delta E_\mathrm{t}(t-t_\mathrm{p},t_\mathrm{p}-t_\mathrm{e}) \underset{t}{*} \mathcal{P}_2(t) \underset{t}{*} \mathcal{D}(t). \tag{4.57}$$

Substitution of Eq. (4.55) and (4.56) into Eq. (4.57) and application of the two-dimensional Fourier transformation leads to the desired result in variables ω and ω_p. With the aid of Eq. (4.13), it is straightforward to write the results for any representation:

$$\Delta E^1_\mathrm{D}(\omega,\omega_\mathrm{e}) = E_0(\omega)Q(\omega+\omega_\mathrm{e},\omega_\mathrm{e})\Delta\chi_1(\omega,\omega_\mathrm{e})\mathcal{P}_2(\omega+\omega_\mathrm{e})\mathcal{D}(\omega+\omega_\mathrm{e}) \tag{4.58}$$

$$\Delta E^2_\mathrm{D}(\omega,\omega_\mathrm{p}) = E_0(\omega-\omega_\mathrm{p})Q(\omega,\omega_\mathrm{p})\Delta\chi_1(\omega-\omega_\mathrm{p},\omega_\mathrm{p})\mathcal{P}_2(\omega)\mathcal{D}(\omega) \tag{4.59}$$

$$\Delta E^3_\mathrm{D}(\omega_\mathrm{p},\omega_\mathrm{e}) = E_0(-\omega_\mathrm{p})Q(\omega_\mathrm{e},\omega_\mathrm{p}+\omega_\mathrm{e})\Delta\chi_1(-\omega_\mathrm{p},\omega_\mathrm{e}+\omega_\mathrm{p})\mathcal{D}(\omega_\mathrm{e}) \tag{4.60}$$

where $E_0(\Omega) = E_\mathrm{E}(\Omega)\mathcal{P}_1(\Omega)$. In order to follow the idea of the transmission spectroscopy (see Eq. (2.15) and the related discussion), we should define the reference waveform. In most situations, the equilibrium properties of the sample are well known to serve as a reference. Assuming the equilibrium transmission of the sample to be $T(\omega)$ and denoting the detected reference waveform as $E_{\mathrm{D}}^{\mathrm{ref}}(\omega)$, we may write

$$\begin{aligned}\frac{\Delta E_{\mathrm{D}}^{1}(\omega,\omega_{\mathrm{e}})}{E_{\mathrm{D}}^{\mathrm{ref}}(\omega)} &= \frac{E_0(\omega)Q(\omega+\omega_{\mathrm{e}},\omega_{\mathrm{e}})\Delta\chi_1(\omega,\omega_{\mathrm{e}})\mathcal{P}_2(\omega+\omega_{\mathrm{e}})\mathcal{D}(\omega+\omega_{\mathrm{e}})}{E_0(\omega)T(\omega)\mathcal{P}_2(\omega)\mathcal{D}(\omega)} = \\ &= \Delta\chi_1(\omega,\omega_{\mathrm{e}})\cdot\frac{Q(\omega+\omega_{\mathrm{e}},\omega_{\mathrm{e}})}{T(\omega)}\cdot\frac{\mathcal{D}(\omega+\omega_{\mathrm{e}})}{\mathcal{D}(\omega)}\cdot\frac{\mathcal{P}_2(\omega+\omega_{\mathrm{e}})}{\mathcal{P}_2(\omega)}\end{aligned} \tag{4.61}$$

and

$$\begin{aligned}\frac{\Delta E_{\mathrm{D}}^{2}(\omega,\omega_{\mathrm{p}})}{E_{\mathrm{D}}^{\mathrm{ref}}(\omega)} &= \frac{E_0(\omega-\omega_{\mathrm{p}})Q(\omega,\omega_{\mathrm{p}})\Delta\chi_1(\omega-\omega_{\mathrm{p}},\omega_{\mathrm{p}})\mathcal{P}_2(\omega)\mathcal{D}(\omega)}{E_0(\omega)T(\omega)\mathcal{P}_2(\omega)\mathcal{D}(\omega)} = \\ &= \frac{E_0(\omega-\omega_{\mathrm{p}})}{E_0(\omega)}\cdot\frac{Q(\omega,\omega_{\mathrm{p}})}{T(\omega)}\cdot\Delta\chi_1(\omega-\omega_{\mathrm{p}},\omega_{\mathrm{p}}).\end{aligned} \tag{4.62}$$

From both expressions, it is possible to calculate *directly* the nonequilibrium contribution $\Delta\chi$ to the susceptibility.

Now, the importance of the representation, in which we perform the two-dimensional scan of ΔE_{D}, becomes clear. In the first case, it is not necessary to know the field E_0 which is at the input face of the sample; on the other hand, in the second case, the propagation behind the sample and the detector response cancels out while the field E_0 is required for calculations. The proposed reference becomes meaningless for the $\Delta E_{\mathrm{D}}(\omega_{\mathrm{p}},\omega_{\mathrm{e}})$, as the transmission of the reference sample cannot be defined using either the frequency ω_{p} or ω_{e}.

4.5 Discussion

The choice of the time delays involved in the experiment is not principally restricted. However, as we wish to perform a two-dimensional Fourier transformation, it is very convenient to scan directly the desired pair of delays, in order to prepare a good situation for the application of the fast Fourier transform algorithm (it is applied to rectangular areas marked in Fig. 4.7*a* and *b*). Thus two different suitable experimental protocol are related to the expressions (4.61) and (4.62). We discuss each protocol separately, and we omit the last representation (ω_{p}, ω_{e}) owing to the missing reference.

4.5.1 Representation 1 (frequencies ω and ω_{e})

In this experiment, the delay line scanning the sampling pulse arrival (t) is kept fixed and the two remaining delay lines (t_{e}, t_{p}) scan the useful part of the waveforms (see Fig. 4.7a). The nonequilibrium susceptibility can be directly calculated from Eq. (4.61):

$$\Delta\chi(\omega, \omega_\mathrm{e}) = \frac{T(\omega)}{Q(\omega + \omega_\mathrm{e}, \omega_\mathrm{e})} \cdot \frac{\Delta E^1_\mathrm{D}(\omega, \omega_\mathrm{e})}{E^\mathrm{ref}_\mathrm{D}} \cdot \frac{\mathcal{P}_2(\omega)\mathcal{D}(\omega)}{\mathcal{P}_2(\omega + \omega_\mathrm{e})\mathcal{D}(\omega_\mathrm{e} + \omega)}. \tag{4.63}$$

The spectrum of the incident pulse E_0 is cancelled out, however it still limits the frequency range where the susceptibility can be extracted (Fig. 4.7c). The reference transmission function T can be experimentally determined. The

Figure 4.7: Upper part: Two-dimensional time-domain scans to be performed. The scan in the delay $(t - t_\mathrm{p})$ is limited due to the time windowing procedure, but the scan in the second delay is practically unlimited. (a) Representation 1, (b) representation 2. Lower part: Accessible ranges in the corresponding two-dimensional Fourier spaces. Gray shadowing represents areas where $\Delta\chi$ can be obtained. Delimiting lines are related to the temporal windowing (1), spectrum of the incident pulse (2), sensor (3), sample in equilibrium state (4), sampling rates in $(t-t_\mathrm{p})$, $(t-t_\mathrm{e})$ and $(t_\mathrm{p}-t_\mathrm{e})$ (5), (6) and (7), scan lengths in $(t - t_\mathrm{e})$ and $(t_\mathrm{p} - t_\mathrm{e})$ (8) and (9), filter function Q (10), diffraction (11) and pump pulse length (12).

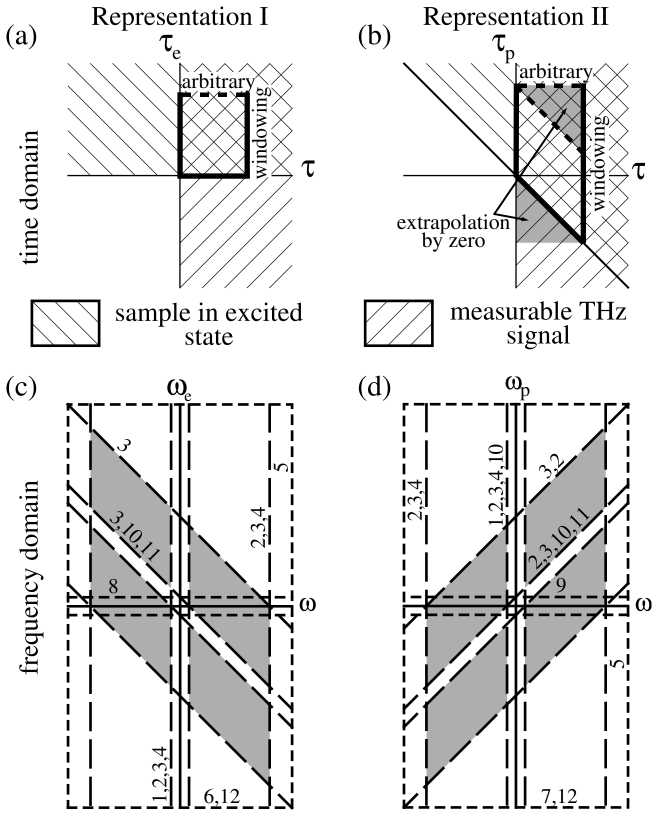

theory of the response of electrooptic detectors is well known (section 3.5.2 and [45,125]); the response function $\mathcal{D}$ can be also determined. However, the spatiotemporal transformations included in $\mathcal{P}_2$ are generally very difficult to describe. It is thus necessary to follow the protocol for the emission experiment (part 3) and exclude any focusing optics. We are left only with the near-field far-field transformation, which can be described as

$$\frac{\mathcal{P}_2(\omega)}{\mathcal{P}_2(\omega+\omega_\mathrm{e})} \propto \frac{\mathrm{i}\omega}{\mathrm{i}(\omega+\omega_\mathrm{e})}\mathrm{e}^{-\mathrm{i}\omega_\mathrm{e}(N_2 d - D)/c}, \tag{4.64}$$

where d is the length of the environment surrounding the sample (e.g. cuvette) and D is the distance between the cuvette and sensor. The large phase factor corresponds to the the time shift of the resulting susceptibility by $(N_2 d + D)/c$ in the second variable $(t - t_\mathrm{e})$. This follows from the definition of the times: t is the time of the measurement and t_e denotes the time when the pump pulse arrives into the sample. It is thus possible to omit this factor provided that the time origin of $(t - t_\mathrm{e})$ is defined in the experiment as the delay when the first signal related to the optical excitation has been detected.

The main advantages of this protocol are the complete elimination of the shape of the incident pulse E_0 and the fact, that the sensor needs to be properly characterized only once. The major disadvantage is the measurement in the far field — as the THz beam is not focused to the sensor, the signal to noise ratio is significantly lower. In order to improve the signal, one needs to use focusing optics. However, it would be necessary to calculate appropriate response function $\mathcal{P}_2$: this is a complicated problem even in simple cases [121].

4.5.2 Representation 2 (frequencies ω and ω_p)

The scheme described by Eq. (4.62) requires the delay line controlling the probe-pulse arrival (t_p) to be held fixed, and the other two lines (t, t_e) to scan the waveforms (Fig. 4.7*b*). Unlike in the preceding case, it is necessary to determine the waveform E_0 incident on the sample, On the other hand, the propagation function $\mathcal{P}_2$ and the response of the detector are eliminated (again, the detector response reduces the useful part of spectra, see Fig. 4.7*d*). In order to determine E_0, it is necessary to replace the sample by an auxiliary detector, and to measure the field E_M in the place of the sample. These fields are related by

$$E_\mathrm{M}(\omega) = \widetilde{\mathcal{D}}(\omega)E_0(\omega), \tag{4.65}$$

where $\widetilde{\mathcal{D}}$ is the response of the auxiliary detector. Eq. (4.62) thus yields

$$\Delta\chi(\omega,\omega_\mathrm{p}) = \frac{T(\omega)}{Q(\omega,\omega_\mathrm{p})} \cdot \frac{E_\mathrm{D}(\omega,\omega_\mathrm{p})}{E_\mathrm{D}^\mathrm{ref}(\omega)} \cdot \frac{E_\mathrm{M}(\omega)\widetilde{\mathcal{D}}(\omega-\omega_\mathrm{p})}{E_\mathrm{M}(\omega-\omega_\mathrm{p})\widetilde{\mathcal{D}}(\omega)}. \tag{4.66}$$

Similarly as in Eq. (4.63), there should appear a phase factor

$$\exp\left(-\mathrm{i}\omega_\mathrm{p}(N_1 d + \Delta D)/c\right) \tag{4.67}$$

due to the finite thickness d of the input window of the cuvette and due to the possible distance ΔD between the input face of the auxiliary detector and the input face of the sample. If the experimental setup provides a possibility to minimize the uncertainty in ΔD, it is possible to calculate this phase factor.

If the experimental setup is sufficiently stable in time, it is possible to determine the complex spectrum of the incident waveform E_0 only once for a whole set of nonequilibrium measurements. However, for this purpose, it is still necessary to evaluate the response of the detector $\widetilde{\mathcal{D}}$ too.

4.5.3 Comparative measurements at different conditions

There is another special possibility of the choice of the reference. It can be sometimes interesting to prepare the sample to be studied at different conditions, e.g. at different temperatures or to use different excitation wavelengths or excitation intensities. Concerning the solvation dynamics, it may be interesting to excite the chromophore to different states. In semiconductors, excitation to different levels above the band gap may be interesting. Variations of the intensity may be used to quantify higher order nonlinearities.

In this case, it is possible to extract the *ratios* of susceptibilities *without* the knowledge of any of the instrumental function ($\mathcal{P}_1$, $\mathcal{P}_2$ and $\mathcal{D}$), therefore it can be determined more precisely. This scheme allows to use any of the representations, resulting in

$$\frac{\Delta^\alpha E_\mathrm{D}^1(\omega,\omega_\mathrm{e})}{\Delta^\beta E_\mathrm{D}^1(\omega,\omega_\mathrm{e})} = \frac{\Delta\chi_1^\alpha(\omega,\omega_\mathrm{e})}{\Delta\chi_1^\beta(\omega,\omega_\mathrm{e})}, \tag{4.68}$$

$$\frac{\Delta^\alpha E_\mathrm{D}^2(\omega,\omega_\mathrm{p})}{\Delta^\beta E_\mathrm{D}^2(\omega,\omega_\mathrm{p})} = \frac{\Delta\chi_1^\alpha(\omega-\omega_\mathrm{p},\omega_\mathrm{p})}{\Delta\chi_1^\beta(\omega-\omega_\mathrm{p},\omega_\mathrm{p})}, \tag{4.69}$$

$$\frac{\Delta^\alpha E_\mathrm{D}^3(\omega_\mathrm{p},\omega_\mathrm{e})}{\Delta^\beta E_\mathrm{D}^3(\omega_\mathrm{p},\omega_\mathrm{e})} = \frac{\Delta\chi_1^\alpha(-\omega_\mathrm{p},\omega_\mathrm{e}+\omega_\mathrm{p})}{\Delta\chi_1^\beta(-\omega_\mathrm{p},\omega_\mathrm{e}+\omega_\mathrm{p})}, \tag{4.70}$$

where indices α and β denote the particular conditions (e.g. temperature, excitation wavelength or intensity). However, if the external parameter changes also the equilibrium properties of the sample (this is for example the case of the temperature), it is necessary to include the corresponding filter functions Q^{α} and Q^{β} to these formulae.

Notice, that this approach is also limited only to the areas, where the sample is sufficiently transparent for the THz radiation. It also becomes clear, why the two-dimensional Fourier transform of the waveform measured with the sample in equilibrium cannot be used as a reference for the measurements given by (4.58–4.60). The two-dimensional Fourier transformation of the equilibrium susceptibility $\chi(t)$ leads to $\chi(\omega)\delta(\omega_{\mathrm{e}})$ or $\chi(\omega)\delta(\omega_{\mathrm{p}})$, i.e. the sample formally appears to be "opaque", when the second variable (i.e. ω_{e} or ω_{p}) is nonzero.

4.5.4 Conclusion

We have analytically solved the problem of the propagation of THz electromagnetic transients in photoexcited media up to the first order. We have shown, that the application of two-dimensional Fourier transformation yields an explicit formula for the spectrum of generalized susceptibility describing the response of the medium after the optical excitation. In our model, all the important effects including refraction on the surfaces of the sample, secondary radiation generated in the bulk, dispersion, absorption of both the THz and optical beam and deviation from the phase-matching condition have been taken into account.

We have proposed two experimental schemes and discussed their advantages and drawbacks. One of the instrumental functions $\mathcal{P}_1$ or $\mathcal{P}_2$ corresponding to the propagation before or after the sample is cancelled out from the expression for calculation of the susceptibility. The equilibrium properties of the sample, its surrounding environment and the response of the detector need to be preliminarily determined. The model allows to examine the spectral range, where the nonequilibrium susceptibility can be determined from the THz experiment. In addition, the relative variation of the nonequilibrium susceptibility as a function of another external parameter can be determined without knowledge of any instrumental function. In this respect, our approach appears to be more convenient for weak response than recent time-domain treatments, where all the instrumental functions $\mathcal{P}_1$, $\mathcal{P}_2$, $\mathcal{D}$ and the emitted waveform E_0 have to be determined. Moreover, the only reported method — finite difference time-domain method — does not allow a direct evaluation of $\Delta\chi$.

Part 5

Summary

In this part, we summarize the contribution of this work. Following original results were achieved:

- We pointed out and discussed the limitations of the reflection spectroscopy. These are due to an extreme sensitivity to any displacement of the sample and to any instability of the whole apparatus. Even submicron displacements may prohibit correct interpretation of the measured data.

- We successfully built a setup for the THz emission spectroscopy. In this setup, we established the relation of the transient current in the sample and the measured THz waveform. This enabled us to study ultrafast carrier dynamics in low-temperature grown GaAs. Four samples grown at different temperatures were investigated: their carrier trapping times and mobilities were determined from the shape of the emitted waveform. These results were interpreted within a simple geometrical model. We also gave a brief overview of other methods used for investigation of ultrafast dynamics in semiconductors.

- We performed a thorough theoretical study of the relation between a generalized susceptibility involved in fast nonequilibrium dynamics of photoexcited systems (e.g. solvation dynamics photoexcited carrier dynamics) and between the quantities accessible via optical pump – THz probe spectroscopy. For weak nonequilibrium response we derived a method which allows to extract directly the generalized susceptibility from two-dimensional scans in optical pump – THz probe experiments. This is the first complete analytical study of the methodology of optical pump – THz probe experiment.

Bibliography

[1] D. H. Auston, K. P. Cheung, and P. R. Smith. Picosecond photoconducting Hertzian dipoles. *Appl. Phys. Lett.* **45** (3), 284–286 (1984).

[2] L. Xu, X. C. Zhang, and D. H. Auston. Terahertz beam generation by femtosecond optical pulses in electrooptic materials. *Appl. Phys. Lett.* **61** (15), 1784–1786 (1992).

[3] A. Leitenstorfer, S. Hunsche, J. Shah, M. C. Nuss, and W. H. Knox. Detectors and sources for ultrabroadband electro-optic sampling: Experiment and theory. *Appl. Phys. Lett.* **74** (11), 1516–1518 (1999).

[4] H. G. Roskos, M. C. Nuss, J. Shah, K. Leo, D. A. B. Miller, A. M. Fox, S. Schmitt-Rink, and K. Köhler. Coherent submillimetre-wave emission from charge oscillations in a double-well potential. *Phys. Rev. Lett.* **68** (14), 2216–2219 (1992).

[5] C. Waschke, H. G. Roskos, R. Schwedler, K. Leo, H. Kurz, and K. Köhler. Coherent submillimetre-wave emission from Bloch oscillations in a semiconductor superlattice. *Phys. Rev. Lett.* **70** (21), 3319–3322 (1993).

[6] C. Fattinger and D. Grischkowsky. Point source terahertz optics. *Appl. Phys. Lett.* **53** (16), 1480–1482 (1988).

[7] P. U. Jepsen and S. R. Keiding. Radiation patterns from lens-coupled terahertz antennas. *Opt. Lett.* **20** (8), 807–809 (1995).

[8] P. U. Jepsen, R. H. Jacobsen, and S. R. Keiding. Generation and detection of terahertz pulses from biased semiconductor antennas. *J. Opt. Soc. Am. B* **13** (11), 2424–2436 (1996).

[9] R. W. Ziolkowski and J. B. Judkins. Propagation characteristics of ultrawide-bandwidth pulsed Gaussian beams. *J. Opt. Soc. Am. A* **9** (11), 2021–2030 (1992).

[10] J. T. Darrow, X.-C. Zhang, and D. H. Auston. Power scaling of large-aperture photoconducting antennas. *Appl. Phys. Lett.* **58** (1), 25–27 (1991).

[11] J. T. Darrow, X.-C. Zhang, D. H. Auston, and J. D. Morse. Saturation properties of large-aperture photoconducting antennas. *IEEE J. of Quantum Electron.* **28** (6), 1607–1616 (1992).

[12] P. K. Benicewicz and A. J. Taylor. Scaling of terahertz radiation from large-aperture biased InP photoconductors. *Opt. Lett.* **18** (16), 1332–1334 (1993).

[13] H. Němec, A. Pashkin, P. Kužel, M. Khazan, S. Schnüll, and I. Wilke. Carrier dynamics in low-temperature grown GaAs studied by terahertz emission spectroscopy. *J. Appl. Phys.* **90** (3), 1303–1306 (2001).

[14] X.-C. Zhang, B. B. Hu, J. T. Darrow, and D. H. Auston. Generation of femtosecond electromagnetic pulses from semiconductor surfaces. *Appl. Phys. Lett.* **56** (11), 1011–1013 (1990).

[15] G.-R. Lin and C.-L. Pan. Characterization of optically excited terahertz radiation from arsenic-ion-implanted GaAs. *Appl. Phys. B* **72** (2), 151–155 (2001).

[16] X.-C. Zhang and D. H. Auston. Optoelectronic measurement of semiconductor surfaces and interfaces with femtosecond optics. *J. Appl. Phys.* **71** (1), 326–338 (1992).

[17] M. Bass, P. A. Franken, J. F. Ward, and G. Weinreich. Optical rectification. *Phys. Rev. Lett.* **9** (11), 446–448 (1962).

[18] D. H. Auston, A. M. Glass, and A. A. Ballman. Optical rectification by impurities in polar crystals. *Phys. Rev. Lett.* **28** (14), 897–900 (1972).

[19] A. Nahata, A. S. Weling, and T. F. Heinz. A wideband coherent terahertz spectroscopy system using optical rectification and electro-optic sampling. *Appl. Phys. Lett.* **69** (16), 2321–2323 (1996).

[20] A. Nahata, D. H. Auston, C. Wu, and J. T. Yardley. Generation of terahertz radiation from a poled polymer. *Appl. Phys. Lett.* **67** (10), 1358–1360 (1995).

[21] R. Huber, A. Brodschelm, F. Tauser, and A. Leitenstorfer. Generation and field-resolved detection of femtosecond electromagnetic pulses tunable up to 41 THz. *Appl. Phys. Lett.* **76** (22), 3191–3193 (2000).

[22] X.-C. Zhang, Y. Jin, and X. F. Ma. Coherent measurement of THz optical rectification from electro-optic crystals. *Appl. Phys. Lett.* **61** (23), 2764–2766 (1992).

[23] X.-C. Zhang, Y. Jin, K. Yang, and L. J. Schowalter. Resonant nonlinear susceptibility near the GaAs band gap. *Phys. Rev. Lett.* **69** (15), 2303–2306 (1992).

[24] A. Rice, Y. Jin, X. F. Ma, , X.-C. Zhang, D. Bliss, J. Larkin, and M. Alexander. Terahertz optical rectification from $\langle 110 \rangle$ zinc-blende crystals. *Appl. Phys. Lett.* **64** (11), 1324–1326 (1994).

[25] G. A. Askaryan. Cerenkovskoe i perechodnoe izlucenja ot elektromagnetnych voln. *Zh. Eksp. Teor. Fiz.* **42** (5), 1360–1364 (1962).

[26] D. H. Auston, K. P. Cheung, J. A. Valdmanis, and D. A. Kleinman. Cherenkov radiation from femtosecond optical pulses in electro-optic media. *Phys. Rev. Lett.* **53** (16), 1555–1558 (1984).

[27] C. Fattinger and D. R. Grischkowsky. A Cherenkov source for freely-propagating terahertz beams. *IEEE J. of Quantum Electron.* **25** (12), 2608–2610 (1989).

[28] X.-C. Zhang, X. F. Ma, Y. Jin, T.-M. Lu, E. P. Boden, P. D. Phelps, K. R. Stewart, and C. P. Yakymyshyn. Terahertz optical rectification from a nonlinear organic crystal. *Appl. Phys. Lett.* **61** (26), 3080–3082 (1992).

[29] H. Hashimoto, H. Takahashi, T. Yamada, K. Kuroyanagi, and T. Kobayashi. Characteristics of the terahertz radiation from single crystals of N-substituted 2-methyl-4-nitroaniline. *J. Phys.: Condens. Matter* **13** (23), 529–537 (2001).

[30] S. L. Chuang, S. Schmitt-Rink, B. I. Greene, P. N. Saeta, and A. F. J. Levi. Optical rectification at semiconductor surfaces. *Phys. Rev. Lett.* **68** (1), 102–105 (1992).

[31] G. Grüner. *Millimeter and Submillimeter Wave Spectroscopy of Solids.* Springer-Verlag, Berlin, Heidelberg (1998).

[32] S. B. University of California. Links to most of the free electron lasers pages. Address: `http://sbfel3.ucsb.edu/www/vl_fel.html`.

[33] S. B. University of California. Properties of free electron lasers. Address: `http://sbfel3.ucsb.edu`.

[34] M. C. Nuss, D. H. Auston, and F. Capasso. Direct subpicosecond measurement of carrier mobility of photoexcited electrons in gallium arsenide. *Phys. Rev. Lett.* **58** (22), 2355–2358 (1987).

[35] P. R. Smith, D. H. Auston, and M. C. Nuss. Subpicosecond photoconducting dipole antennas. *IEEE J. of Quantum Electron.* **24** (2), 255–260 (1988).

[36] Q. Wu and X.-C. Zhang. Free-space electro-optic sampling of terahertz beams. *Appl. Phys. Lett.* **67** (24), 3523–3525 (1995).

[37] J. A. Riordan, F. G. Sun, Z. G. Lu, and X.-C. Zhang. Free-space transient magneto-optic sampling. *Appl. Phys. Lett.* **71** (11), 1452–1454 (1997).

[38] B. I. Greene, J. F. Federici, D. R. Dykaar, R. R. Jones, and P. H. Bucksbaum. Interferometric characterization of 160 fs far-infrared light-pulses. *Appl. Phys. Lett.* **59** (8), 893–895 (1991).

[39] S. Kono, M. Tani, P. Gu, and K. Sakai. Detection of up to 20 THz with a low-temperature-grown GaAs photoconductive antenna gated with 15 fs light pulses. *Appl. Phys. Lett.* **77** (25), 4104–4106 (2000).

[40] M. Tani, K. Sakai, and H. Mimura. Ultrafast photoconductive detectors based on semi-insulating GaAs and InP. *Jpn. J. Appl. Phys.* **36** (9AB), 1175–1178 (1997).

[41] F. G. Sun, G. A. Wagoner, and X.-C. Zhang. Measurement of free-space terahertz pulses via long-lifetime photoconductors. *Appl. Phys. Lett.* **67** (12), 1656–1658 (1995).

[42] Z. Jiang, F. G. Sun, Q. Chen, and X.-C. Zhang. Electro-optic sampling near zero optical transmission point. *Appl. Phys. Lett.* **74** (9), 1191–1193 (1999).

[43] Z. Jiang and X.-C. Zhang. Electro-optic measurement of THz field pulses with a chirped optical beam. *Appl. Phys. Lett.* **72** (16), 1945–1947 (1998).

[44] Q. Wu, M. Litz, and X.-C. Zhang. Broadband detection capability of ZnTe electro-optic field detectors. *Appl. Phys. Lett.* **68** (21), 2924–2926 (1996).

[45] H. J. Bakker, G. C. Cho, H. Kurz, Q. Wu, and X.-C. Zhang. Distortion of terahertz pulses in electro-optic sampling. *J. Opt. Soc. Am. B* **15** (6), 1795–1801 (1998).

[46] M. Schall and P. U. Jepsen. Freeze-out of difference-phonon modes in ZnTe and its application in detection of THz pulses. *Appl. Phys. Lett.* **77** (18), 2801–2803 (2000).

[47] Q. Wu and X.-C. Zhang. 7 terahertz broadband GaP electro-optic sensor. *Appl. Phys. Lett.* **70** (14), 1784–1786 (1997).

[48] P. Y. Han, , M. Tani, F. Pan, and X.-C. Zhang. Use of the organic crystal DAST for terahertz beam applications. *Opt. Lett.* **25** (9), 675–677 (2000).

[49] P. U. Jepsen, C. Winnewisser, M. Schall, V. Schyja, S. R. Keiding, and H. Helm. Detection of THz pulses by phase retardation in lithium tantalate. *Phys. Rev. E* **53** (4), 3052–3054 (1996).

[50] C. Winnewisser, P. U. Jepsen, M. Schall, V. Schyja, and H. Helm. Electro-optic detection of THz radiation in $LiTaO_3$, $LiNbO_3$ and ZnTe. *Appl. Phys. Lett.* **70** (23), 3069–3071 (1997).

[51] T. Dekorsy, X. Q. Zhou, K. Ploog, and H. Kurz. Subpicosecond electric field dynamics in low-temperature-grown GaAs observed by reflective electro-optic sampling. *Mater. Sci. Eng. B* **22** (1), 68–71 (1993).

[52] M. C. Beard, G. M. Turner, and C. A. Schmuttenmaer. Measurement of electromagnetic radiation emitted during rapid intramolecular electron transfer. *J. Am. Chem. Soc.* **122** (46), 11 541–11 542 (2000).

[53] S. S. Prabhu, S. E. Ralph, M. R. Melloch, and E. S. Harmon. Carrier dynamics of low-temperature-grown GaAs observed via THz spectroscopy. *Appl. Phys. Lett.* **70** (18), 2419–2421 (1997).

[54] M. C. Beard, G. M. Turner, and C. A. Schmuttenmaer. Transient photoconductivity in GaAs as measured by time-resolved terahertz spectroscopy. *Phys. Rev. B* **62** (23), 15 764–15 777 (2000).

[55] P. Kužel and J. Petzelt. Time-resolved terahertz transmission spectroscopy of dielectrics. *Ferroelectrics* **239** (1–4), 949–956 (2000).

[56] M. van Exter and D. Grischkowsky. Optical and electronic properties of doped silicon from 0.1 to 2 THz. *Appl. Phys. Lett.* **56** (17), 1694–1696 (1990).

[57] M. C. Nuss, P. M. Mankiewich, M. L. O'Malley, and E. H. Westerwick. Dynamic conductivity and "coherence peak" in $YBa_2Cu_3O_7$ superconductors. *Phys. Rev. Lett.* **66** (25), 3305–3308 (1991).

[58] T.-I. Jeon, D. Grischkowsky, A. K. Mukherjee, and R. Menon. Electrical characterization of conducting polypyrrole by THz time-domain spectroscopy. *Appl. Phys. Lett.* **77** (16), 2452–2454 (2000).

[59] J. T. Kindt and C. A. Schmuttenmaer. Far-infrared dielectric properties of polar liquids probed by femtosecond terahertz pulse spectroscopy. *J. Phys. Chem.* **100** (24), 10 373–10 379 (1996).

[60] H. Harde, N. Katzenellenbogen, and D. Grischkowsky. Terahertz coherent transients from methyl chloride vapour. *J. Opt. Soc. Am. B* **11** (6), 1018–1030 (1994).

[61] R. A. Cheville and D. Grischkowsky. Far-infrared terahertz time-domain spectroscopy of flames. *Opt. Lett.* **20** (15), 1646–1648 (1995).

[62] L. Duvillaret, F. Garet, and J.-L. Coutaz. A reliable method for extraction of material parameters in terahertz time-domain spectroscopy. *IEEE J. Selected Topics in Quantum Electron.* **2** (3), 739–745 (1996).

[63] L. Duvillaret, F. Garet, and J.-L. Coutaz. Highly precise determination of optical constants and sample thickness in terahertz time-domain spectroscopy. *Appl. Opt.* **38** (2), 409–415 (1999).

[64] N. Negre and S. Crooker. In *26th International Conference on Infrared and Millimeter Waves IRMMW 2001* (2001).

[65] D. Hashimshony, I. Geltner, G. Cohen, Y. Avitzour, A. Zigler, and C. Smith. Characterization of the electrical properties and thickness of thin epitaxial semiconductor layers by THz reflection spectroscopy. *J. Appl. Phys.* **90** (11), 5778–5781 (2001).

[66] T.-I. Jeon and D. Grischkowsky. Characterization of optically dense, doped semiconductors by reflection THz time domain spectroscopy. *Appl. Phys. Lett.* **72** (23), 3032–3034 (1998).

[67] S. C. Howells and L. A. Schlie. Transient terahertz reflection spectroscopy of undoped InSb from 0.1 to 1.1 THz. *Appl. Phys. Lett.* **69** (4), 550–552 (1996).

[68] P. C. M. Planken, M. C. Nuss, I. Brener, and K. W. Goossen. Terahertz emission in single quantum wells after coherent excitation of light hole and heavy hole excitons. *Phys. Rev. Lett.* **69** (26), 3800–3803 (1992).

[69] R. Kersting, K. Unterrainer, G. Strasser, H. F. Kauffmann, and E. Gornik. Few-cycle THz emission from cold plasma oscillations. *Phys. Rev. Lett.* **79** (16), 3038–3041 (1997).

[70] R. McLaughlin, A. Corchia, M. B. Johnston, Q. Chen, C. M. Ciesla, D. D. Arnone, G. A. C. Jones, E. H. Linfield, A. G. Davies, and M. Pepper. Enhanced coherent terahertz emission from indium arsenide in the presence of a magnetic field. *Appl. Phys. Lett.* **76** (15), 2038–2040 (2000).

[71] R. D. Averitt, G. Rodriguez, J. L. W. Siders, S. A. Trugman, and A. J. Taylor. Conductivity artifacts in optical-pump THz-probe measurements of $YBa_2Cu_3O_7$. *J. Opt. Soc. Am. B* **17** (2), 327–331 (2000).

[72] R. McElroy and K. Wynne. Ultrafast dipole solvation measured in the far infrared. *Phys. Rev. Lett.* **79** (16), 3078–3081 (1997).

[73] J. T. Kindt and C. A. Schmuttenmaer. Theory for determination of the low-frequency time-dependent response function in liquids using time-resolved terahertz pulse spectroscopy. *J. Chem. Phys.* **110** (17), 8589–8596 (1999).

[74] D. Grischkowsky, S. Keiding, M. van Exter, and C. Fattinger. Far-infrared time-domain spectroscopy with terahertz beams of dielectrics and semiconductors. *J. Opt. Soc. Am. B* **7** (10), 2006–2015 (1990).

[75] S. Kamba, J. Petzelt, E. Buixaderas, D. Haubrich, P. Vanek, P. Kuzel, I. N. Jawahar, M. T. Sebastian, and P. Mohanan. High frequency dielectric properties of $A_5B_4O_{15}$ microwave ceramics. *J. Appl. Phys.* **89** (7), 3900–3906 (2001).

[76] A. Pashkin, E. Buixaderas, P. Kužel, M.-H. Liang, C.-T. Hu, and I.-N. Lin. THz transmission spectroscopy applied to dielectrics and microwave ceramics. *Ferroelectrics* **254**, 113–120 (2001).

[77] H. J. Bakker, S. Hunsche, and H. Kurz. Investigation of anharmonic lattice-vibrations with coherent phonon polaritons. *Phys. Rev. B* **50** (2), 914–920 (1994).

[78] M. C. Beard, G. M. Turner, and C. A. Schmuttenmaer. Subpicosecond carrier dynamics in low-temperature grown GaAs as measured by time-resolved terahertz spectroscopy. *J. Appl. Phys.* **90** (12), 5915–5923 (2001).

[79] C. Messner, H. Kostner, and R. A. Höpfel. Time-resolved THz spectroscopy of proton-bombarded InP. *J. Opt. Soc. Am. B* **18** (9), 1369–1371 (2001).

[80] A. Leitenstorfer, S. Hunsche, J. Shah, M. C. Nuss, and W. H. Knox. Femtosecond charge transport in polar semiconductors. *Phys. Rev. Lett.* **82** (25), 5140–5143 (1999).

[81] J. N. Heyman, P. Neocleous, D. Hebert, P. A. Crowell, T. Müller, and K. Unterrainer. Terahertz emission from GaAs and InAs in a magnetic field. *Phys. Rev. B* **64** (8), 5202–5208 (2001).

[82] C. Rønne, P.-O. Åstrand, and S. R. Keiding. THz spectroscopy of liquid H_2O and D_2O. *Phys. Rev. Lett.* **82** (14), 2888–2891 (1999).

[83] B. N. Flanders, R. A. Cheville, D. Grischkowsky, and N. F. Scherer. Pulsed terahertz transmission spectroscopy of liquid $CHCl_3$, CCl_4, and their mixtures. *J. Phys. Chem.* **100** (29), 11 824–11 835 (1996).

[84] E. Knoesel, M. Bonn, J. Shan, and T. F. Heinz. Charge transport and carrier dynamics in liquids probed by THz time-domain spectroscopy. *Phys. Rev. Lett.* **86** (2), 340–343 (2001).

[85] G. Haran, W.-D. Sun, K. Wynne, and R. M. Hochstrasser. Femtosecond far-infrared pump–probe spectroscopy: a new tool for studying low-frequency vibrational dynamics in molecular condensed phases. *Chem. Phys. Lett.* **274** (4), 365–371 (1997).

[86] F. W. Smith, A. R. Calawa, C.-L. Chen, M. J. Manfra, and L. J. Mahoney. New MBE buffer used to eliminate backgating in GaAs-MESFET's. *IEEE Electron. Device Lett.* **9** (2), 77–80 (1988).

[87] M. Kaminska, Z.-L. Weber, E. R. Weber, T. George, J. B. Kortright, F. W. Smith, B.-Y. Tsaur, and A. R. Calawa. Structural properties of As-rich GaAs grown by molecular beam epitaxy at low temperatures. *Appl. Phys. Lett.* **54** (19), 1881–1883 (1989).

[88] M. Kaminska, E. R. Weber, Z.-L. Weber, R. Leon, and Z. U. Rek. Stoichiometry-related defects in GaAs grown by molecular-beam epitaxy at low temperatures. *J. Vac. Sci. Tech. B* **7** (4), 710–713 (1989).

[89] F. W. Smith, H. Q. Le, V. Diadiuk, M. A. Hollis, A. R. Calawa, S. Gupta, M. Frankel, D. R. Dykaar, G. A. Mourou, and T. Y. Hsiang. Picosecond GaAs-based photoconductive optoelectronic detectors. *Appl. Phys. Lett.* **54** (10), 890–892 (1989).

[90] M. Y. Frankel, J. F. Whitaker, G. A. Mourou, F. W. Smith, and A. R. Calawa. High-voltage picosecond photoconductor switch based on low-temperature-grown GaAs. *IEEE Trans. Electron Devices* **37** (12), 2493–2498 (1990).

[91] M. Haiml, U. Siegner, F. Morier-Genoud, U. Keller, M. Luysberg, P. Spetch, and E. R. Weber. Femtosecond response time and high optical nonlinearity in beryllium-doped low-temperature grown GaAs. *Appl. Phys. Lett.* **74** (9), 1269–1271 (1999).

[92] G. M. Metze, A. R. Calawa, and J. G. Mavroides. An investigation of GaAs films grown by MBE at low substrate temperatures and growth rates. *J. Vac. Sci. Tech. B* **1** (2), 166–169 (1983).

[93] H. J. von Bardeleben, M. O. Manasreh, D. C. Look, K. R. Evans, and C. E. Stutz. Electron-paramagnetic-resonance study of GaAs grown by low-temperature molecular-beam epitaxy. *Phys. Rev. B* **45** (7), 3372–3375 (1992).

[94] M. Stellmacher, R. Bisaro, P. Galtier, J. Nagle, and K. Khirouni. Defects and defect behaviour in GaAs grown at low temperature. *Semicond. Sci. Technol.* **16** (6), 440–446 (2001).

[95] M. R. Melloch, N. Otsuka, J. M. Woodall, A. C. Warren, and J. L. Freeouf. Formation of arsenic precipitates in GaAs buffer layers grown by molecular beam epitaxy at low substrate temperatures. *Appl. Phys. Lett.* **57** (15), 1531–1533 (1990).

[96] A. C. Warren, J. M. Woodall, J. L. Freeouf, D. Grischkowsky, D. T. McInturff, M. R. Melloch, and N. Otsuka. Arsenic precipitates and the semi-insulating properties of GaAs buffer layers grown by low-temperature molecular beam epitaxy. *Appl. Phys. Lett.* **57** (13), 1331–1333 (1990).

[97] Z. Lilental-Weber, A. Claverie, J. Washburn, F. Smith, and R. Calawa. Microstructure of annealed low-temperature-grown GaAs layers. *Appl. Phys. A* **53** (2), 141–146 (1991).

[98] R. M. Feenstra, J. M. Woodall, and G. D. Pettit. Observation of bulk defects by scanning-tunnelling-microscopy and spectroscopy – arsenic antisite defects in GaAs. *Phys. Rev. Lett.* **71** (8), 1176–1179 (1993).

[99] K. Krambrock, M. Linde, J.-M. Spaeth, D. C. Look, D. Bliss, and W. Walukiewicz. Arsenic antisite-related defects in low-temperature MBE grown GaAs. *Semicond. Sci. Technol.* **7** (8), 1037–1041 (1992).

[100] J. Gebauer, R. Krause-Rehberg, S. Eichler, M. Luysberg, H. Sohn, and E. R. Weber. Ga vacancies in low-temperature-grown GaAs identified by slow positrons. *Appl. Phys. Lett.* **71** (5), 638–640 (1997).

[101] J. K. Luo, H. Thomas, D. V. Morgan, and D. Westwood. Transport properties of GaAs layers grown by molecular beam epitaxy at low temperature and the effects of annealing. *J. Appl. Phys.* **79** (7), 3622–3629 (1996).

[102] D. C. Look, D. C. Walters, M. O. Manasreh, J. R. Sizelove, C. E. Stutz, and K. R. Evans. Anomalous Hall-effect in low-temperature molecular-beam-epitaxial GaAs: Hopping in a dense *EL*2-like band. *Phys. Rev. B* **42** (6), 3578–3581 (1990).

[103] M. O. Manasreh, D. C. Look, K. R. Evans, and C. E. Stutz. Infrared absorption of deep defects in molecular-beam-epitaxial GaAs layers grown at 200°C: Observation of an *EL*2-like defect. *Phys. Rev. B* **41** (14), 10 272–10 275 (1990).

[104] P. W. Yu, G. D. Robinson, J. R. Sizelove, and C. E. Stutz. 0.8-eV photoluminescence of GaAs grown by molecular-beam epitaxy at low temperatures. *Phys. Rev. B* **49** (7), 4689–4694 (1994).

[105] R. P. Mirin, J. P. Ibbetson, U. K. Mishra, and A. C. Gossard. Low temperature limits to molecular beam epitaxy of GaAs. *Appl. Phys. Lett.* **65** (18), 2335–2337 (1994).

[106] R. Yano, Y. Hirayama, S. Miyashita, H. Sasabu, N. Uesugi, and S. Uehara. Pump-probe spectroscopy of low-temperature grown GaAs for carrier lifetime estimation: arsenic pressure dependence of carrier lifetime during MBE crystal growth. *Phys. Lett. A* **289** (1–2), 93–98 (2001).

[107] C. H. Lee, A. Antonetti, and G. Mourou. Measurements on the photoconductive lifetime of carriers in GaAs by optoelectronic gating technique. *Opt. Commun.* **21**, 158–161 (1977).

[108] J. Kuhl, E. O. Göbel, T. Pfeiffer, and A. Jonitez. Subpicosecond carrier trapping in high-defect-density amorphous Si and GaAs. *Appl. Phys. A* **34** (2), 105–110 (1984).

[109] M. Lambsdorff, J. Kuhl, J. Rosenzweig, A. Axmann, and J. Schneider. Subpicosecond carrier lifetimes in radiation-damaged GaAs. *Appl. Phys. Lett.* **58** (17), 1881–1883 (1991).

[110] S. Gupta, M. Y. Frankel, J. A. Valdmanis, J. F. Whitaker, G. A. Mourou, F. W. Smith, and A. R. Calawa. Subpicosecond carrier lifetime in GaAs grown by molecular beam epitaxy at low temperatures. *Appl. Phys. Lett.* **59** (25), 3276–3278 (1991).

[111] A. Krotkus, K. Bertulis, L. Dapkus, U. Olin, and S. Marcinkevičius. Ultrafast carrier trapping in Be-doped low-temperature-grown GaAs. *Appl. Phys. Lett.* **75** (21), 3336–3338 (1999).

[112] T. S. Sosnowski, T. B. Norris, H. H. Wang, P. Grenier, J. F. Whitaker, and C. Y. Sung. High-carrier-density electron dynamics in low-temperature-grown GaAs. *Appl. Phys. Lett.* **70** (24), 3245–3247 (1997).

[113] U. Siegner, R. Fluck, G. Zhang, and U. Keller. Ultrafast high-intensity nonlinear absorption dynamics in low-temperature grown gallium arsenide. *Appl. Phys. Lett.* **69** (17), 2566–2568 (1996).

[114] S.-F. Horng, S.-H. Lu, J.-S. Yu, T.-R. Tsai, and C.-C. Chi. Comparison of optical pump-probe characterization of low-temperature-grown GaAs at well-above-bandgap and near-bandedge wavelengths. *Opt. Quantum Electron.* **32** (4–5), 573–584 (2000).

[115] P. A. Loukakos, C. Kalpouzos, I. E. Perakis, Z. Hatzopoulos, M. Logaki, and C. Fotakis. Ultrafast electron trapping times in low-temperature-grown gallium arsenide: The effect of the arsenic precipitate spacing and size. *Appl. Phys. Lett.* **79** (18), 2883–2885 (2001).

[116] P. W. E. Smith, S. D. Benjamin, and H. S. Loka. Tailoring of trap-related carrier dynamics in low-temperature-grown GaAs. *Appl. Phys. Lett.* **71** (9), 1156–1158 (1997).

[117] P. Grenier and J. F. Whitaker. Subband gap carrier dynamics in low-temperature-grown GaAs. *Appl. Phys. Lett.* **70** (15), 1998–2000 (1997).

[118] G. Segschneider, T. Dekorsy, H. Kurz, R. Hey, and K. Ploog. Energy resolved ultrafast relaxation dynamics close to the band edge of low-temperature grown GaAs. *Appl. Phys. Lett.* **71** (19), 2779–2781 (1997).

[119] S. D. Benjamin, H. S. Loka, A. Othonos, and P. W. E. Smith. Ultrafast dynamics of nonlinear absorption in low-temperature-grown GaAs. *Appl. Phys. Lett.* **68** (18), 2544–2546 (1996).

[120] F. Ganikhanov, K. C. Burr, and C. L. Tang. Ultrafast dynamics of holes in GaAs probed by two-color femtosecond spectroscopy. *Appl. Phys. Lett.* **73** (1), 64–66 (1998).

[121] P. Kužel, M. A. Khazan, and J. Kroupa. Spatiotemporal transformations of ultrashort terahertz pulses. *J. Opt. Soc. Am. B* **16** (10), 1795–1800 (1999).

[122] S. Gupta, J. F. Whitaker, and G. A. Mourou. Ultrafast carrier dynamics in III-V semiconductors grown by molecular-beam epitaxy at very low substrate temperatures. *IEEE J. of Quantum Electron.* **28** (10), 2464–2472 (1992).

[123] S. M. Sze. *Semiconductor Devices: Physics and Technology.* John Wiley & Sons, New York (1985).

[124] M. van Exter, C. Fattinger, and D. Grischkowsky. Terahertz time-domain spectroscopy of water-vapor. *Opt. Lett.* **14** (20), 1128–1130 (1989).

[125] G. Gallot and D. Grischkowsky. Electro-optic detection of terahertz radiation. *J. Opt. Soc. Am. B* **16** (8), 1204–1212 (1999).

[126] D. T. F. Marple. Refractive index of ZnSe, ZnTe and CdTe. *J. Appl. Phys.* **35** (3), 539–542 (1964).

[127] M. Stellmacher, J.-P. Schnell, D. Adam, and J. Nagle. Photoconductivity investigation of the electron dynamics in GaAs grown at low temperature. *Appl. Phys. Lett.* **74** (9), 1239–1241 (1999).

[128] M. C. Beard and C. A. Schmuttenmaer. Using the finite-difference time-domain pulse propagation method to simulate time-resolved THz experiments. *J. Chem. Phys.* **114** (7), 2903–2909 (2001).

[129] D. You and P. H. Bucksbaum. Propagation of half-cycle far infrared pulses. *J. Opt. Soc. Am. B* **14** (7), 1651–1655 (1997).